DISSERTATION

Towards bottom-up silicon nanowire-based biosensing:

Innovative concepts for fabricating lab-on-a-chip devices

zur Erlangung des akademischen Grades
Doktoringenieur (Dr. - Ing.)

vorgelegt von

Andreas Gang
geboren am 09. März 1985 in Wolfen

Technische Universität Dresden, Fakultät Maschinenwesen,
Institut für Werkstoffwissenschaft,
Lehrstuhl für Materialwissenschaft und Nanotechnik

Tag der Einreichung: 04.04.2017
Tag der Verteidigung: 09.03.2018

1. Gutachter: Prof. Gianaurelio Cuniberti, TU Dresden
2. Gutachter: Prof. Hans-Peter Wiesmann, TU Dresden

„Grau is alle Theorie – entscheidend is auf'm Blatt!"

Sehr frei nach Alfred "Adi" Preißler (1921 – 2003),
Spieler der deutschen Fußballnationalmannschaft

KURZZUSAMMENFASSUNG

Unter dem Begriff „Lab-on-a-Chip" (LoC) fasst man stark miniaturisierte Systeme zusammen, die die Fähigkeiten eines ganzen Labors auf einen transportablem Mikrochip übertragen. Insbesondere im Bereich der Analyse chemischer und biologischer Proben werden solche Plattformen bevorzugt eingesetzt, da sie direkt am Ort der Probenentnahme schnelle, hoch sensible Messungen ermöglichen.

Im Mittelpunkt dieser Doktorarbeit stehen Sensoren auf Basis von Siliziumnanodrähten (SiNWs). Auf verschiedenen Gebieten werden innovative Konzepte zur einfachen und zuverlässigen Herstellung von LoC Systemen entwickelt.

Zu Beginn wird ein multifunktionaler Mikrofluidik-Aufbau vorgestellt, der ein einfaches reversibles Verschließen von Mikrofluidik-Kanälen auf nahezu allen möglichen Substraten erlaubt. Der Aufbau ermöglicht das schnelle Anfertigen und Testen verschiedener Kanalstrukturen sowie das Betreiben von Fluidik-Experimenten mit hohen Arbeitsdrücken von bis zu 600 kPa. Der zweite Schwerpunkt der Arbeit ist die Entwicklung einer Methode zur Funktionalisierung von Sensor-Oberflächen mittels 3-(Triethoxysilyl) Propyl Bernsteinsäure Anhydrid (TESPSA) für die Immobilisierung spezifischer Rezeptormoleküle. Bei dieser Methode entfällt die Notwendigkeit einer zusätzlichen Passivierung ungenutzter Anbindungsstellen. Des Weiteren erfolgt die Herstellung von Parallelschaltungen von Schottky-Barrieren-Feld-Effekt-Transistoren (SB-FETs) aus „bottom-up" gewachsenen SiNWs durch mechanisches Abreiben der SiNWs vom Wachstumssubstrat auf ein Empfängersubstrat.

Unter Verwendung des eingangs entwickelten Mikrofluidik-Aufbaus wird die prinzipielle Anwendbarkeit der TESPSA-basierten Rezeptor-Immobilisierung nachgewiesen, sowohl anhand von Fluoreszenzmikroskopie-Untersuchungen als auch mit Hilfe der SiNW FETs als Biosensoren. Mittels eines Rezeptor-Analyt-Systems, bestehend aus verschiedenen Antikörpern und einem Peptid des Influenzavirus A, wird gezeigt, dass Antikörper, die über TESPSA an Oberflächen gebunden werden, ihre Spezifizität für ihre Antigene beibehalten.

Der vierte große Forschungsabschnitt dieser Arbeit widmet sich der mikrofluidischen Ausrichtung eindimensionaler Nanomaterialien und deren Ablage an vorgegebenen Fangstellen, wodurch eine zuverlässige Herstellung von FETs aus Einzelnanodrähten erreicht wird. Es wird davon ausgegangen, dass Einzelnanodraht-FETs gegenüber Parallelschaltungen von Nanodraht-FETs verbesserte Sensoreigenschaften aufweisen.

Folglich beinhaltet diese Arbeit viele zukunftsweisende Ansätze für die Herstellung von LoC Systemen. Untersuchungen über eine Bandbreite von Längenskalen, von Mikrometer großen Strukturen bis hinab zur molekularen Ebene, werden präsentiert. Es wird davon ausgegangen, dass die vorgestellten Methoden als eine vielfältige Sammlung von

Werkzeugen nicht nur bei der Herstellung von Biosensoren auf SiNW-Basis Einsatz finden, sondern ganz allgemein den Aufbau verschiedenster LoC Systeme vorantreiben.

ABSTRACT

The term "Lab-on-a-Chip" (LoC) describes highly miniaturized systems in which the functionalities of entire laboratories are scaled down to the size of transportable microchips. Particularly in the field of chemical and bio-analysis, such platforms are desired for a fast and highly sensitive sample analysis at the *point of care*.

This work focuses on silicon nanowire (SiNW) based sensors. Innovative device fabrication concepts are developed from various directions, for a facile and reliable assembly of LoC analysis systems.

Firstly, a multifunctional microfluidic set-up is developed which allows for a facile reversible sealing of channel structures on virtually any kind of substrate while maintaining the possibility of a rapid prototyping of versatile channel designs and the applicability of high working pressures of up to 600 kPa. Secondly, a 3-(triethoxysilyl)propylsuccinic anhydride (TESPSA) based surface modification strategy for the attachment of specific receptor molecules without additional binding site passivation is explored. Thirdly, bottom-up grown SiNWs are utilized for producing parallel arrays of Schottky barrier field-effect transistors (FETs) *via* contact printing.

Using the initially developed microfluidic set-up, the concept of the TESPSA-based receptor immobilization is proved *via* fluorescence microscopy and by applying the SiNW FETs as biosensors. Using a receptor-analyte system based on a set of antibodies and a peptide from human influenza hemagglutinin, it is shown that antibodies immobilized with the developed method maintain the specificity for their antigens.

The fourth major research field in this work is the microfluidics-based alignment of one-dimensional nanostructures and their deposition at predetermined trapping sites for reliably fabricating single NW-based FETs. Such devices are expected to provide superior sensitivity over sensors based on parallel arrays of FETs.

Consequently, within this work, innovative LoC devices fabrication approaches over a broad range of length scales, from micrometer scale down to the molecular level, are investigated. The presented methods are considered a highly versatile and beneficial tool set not only for SiNW-based biosensors, but also for any other LoC application.

CONTENT

ABBREVIATIONS AND SYMBOLS

1D	One-dimensional
2D	Two-dimensional
3D	Three-dimensional
ALD	Atomic layer deposition
APDMES	(3-Aminopropyl)dimethylethoxysilane
APTES	3-aminopropyltriethoxysilane
AuNP	Gold nanoparticle
BioFET	Field effect transistor-based sensor for biological species
BP	Band pass
BPEI	Branched polyethylenimine
BS	Beam splitter
BSA	Bovine serum albumin
ChemFET	Field effect transistor-based sensor for chemicals
CuO NW	Copper (II) oxide nanowire
CVD	Chemical vapor deposition
DI	Deionized
DNA	Deoxyribonucleic acid
EBL	Electron-beam lithography
EDC	N-(3-dimethylaminopropyl)-N′-ethylcarbodiimide
ELISA	Enzyme-linked immonosorbent assay
FAM	6-FAM™ Dye Phosphoramidite
FET	Field effect transistor
FITC	Fluorescein isothiocyanate
GC-MS	Chromatography-mass spectrometry
HA	Human influenza hemagglutinin
HF	Hydrofluoric acid
HFDMCS	(Heptadecafluoro-1,1,2,2-tetrahydrodecyl)dimethylchlorosilane
IgG	Immunoglobulin G
IgGControl$_{red}$	Donkey anti-goat IgG, DyLight 594
IgGReceptor	Donkey anti-rabbit IgG
IgGTarget$_{green}$	Rabbit anti-mouse IgG, DyLight 488
ISFET	Ion sensitive field effect transistor
LoC	Lab on a chip
MeOH	Methanol
MIMIC	Micromoulding in capillaries
MOSFET	Metal-oxide field effect transistor
mPEG	Polyethylen glycol

mTAS	Miniaturized total chemical analysis systems
NBS	Nucleotide binding site
NHS	N-hydroxysuccinimide
NW	Nanowire
PB	Phosphate buffer
PBS	Phosphate buffered saline
PBS-Tween	Phosphate buffered saline with added Tween20
PCR	Polymerase chain reaction
PDMS	Polydimethylsiloxane
PEDOT:PSS	Poly(3,4-ethylenedioxythiophene)poly(styrenesulfonate)
PMMA	Polymethylmethacrylate
PTFE	Polytetrafluoroethylene
RT	Room temperatur
RTP	Rapid thermal processing
SB	Schottky barrier
SEM	Scanning electron microscopy
SiNW	Silicon nanowire
SMU	Source measure unit
SNR	Signal-to-noise ratios
TEMAHf	Ethylmethylaminohafnium
TESPSA	3-(triethoxysilyl)propylsuccinic anhydride
TMA	Trimethyl Aluminium
UVL	UV-lithography
VLS	Vapor-liquid-solid
XPS	X-ray photoelectron spectroscopy

α	pH sensitivity factor (dimensionless)
β	Sensitivity parameter (dimensionless)
β_S	Surface buffer capacity of the oxide (C V^{-1})
ϵ_0	Permittivity of free space (8.854187817 · 10^{-12} C V^{-1} m^{-1})
ϵ_r	Dielectric constant (dimensionless)
κ	Gate-coupling efficiency (dimensionless)
λ_D	Debye screening length (m)
μ	Electron mobility (m^2 V^{-1} s^{-1})
η	Dynamic viscosity (N s m^{-2})
ρ	Density (kg m^{-3})
Φ	Workfunction (eV)
χ^{sol}	Surface dipole potential (V)

Symbol	Definition
Ψ	Surface potential (V)
c	Concentration (mol l^{-1})
C_D	Depletion capacitance (C V^{-1} m^{-2})
C_H	Helmholtz layer capacitance (C V^{-1} m^{-2})
C_{it}	interface-trap capacitance (C V^{-1} m^{-2})
C_{Ox}	Capacitance of gate oxide per unit area (C V^{-1} m^{-2})
C_S	Differential double-layer capacitance (C V^{-1})
E_{ref}	Potential of reference electrode (V)
F	Faraday constant (96485.33289 C mol^{-1})
g	Transconductance (A V^{-1})
I	Ionic strength (mol l^{-1})
I_{max}	Maximum current (A)
I_{min}	Minimum current (A)
I_{off}	*off*-current (A)
I_{on}	*on*-current (A)
I_{SD}	Source-drain current (A)
k	Boltzmann constant (1.38064852 $\cdot$ 10^{-23} J K^{-1})
K_{a1}, K_{a2}	Dissociation constants for protonation and deprotonation of -OH groups, respectively (dimensionless)
L	Length (m)
N	Sample size (dimensionless)
N_A	Avogadro number (6.022140857 $\cdot$ 10^{23} mol^{-1})
N_S	Number of binding sites per surface area (m^{-2})
q	Elementary charge (1.60217662 $\cdot$ 10^{-19} C)
Q_D	Depletion charge in silicon (C m^{-2})
Q_{Ox}	Accumulated charge in the Oxide (C m^{-2})
Q_{SS}	Accumulated charge at the oxide-Si interface (C m^{-2})
R	Universal gas constant (8.3144598 J K^{-1} mol^{-1})
Re	Reynolds number (dimensionless)
S	Subthreshold swing (Volts per decade $\rightarrow$ V dec^{-1})
S_c	Concentration sensitivity (Volts per decade $\rightarrow$ V dec^{-1})
S_{pH}	pH sensitivity (V pH^{-1})
T	Absolute temperature (K)
t	Time (s)
u	flow velocity (m^3 s^{-1})
V	Volume (m^3)
V_{BG}	Back-gate voltage(V)
V_G	Gate voltage (V)
V_{LG}	Liquid gate voltage (V)

V_{SD}	Sorurce-drain voltage (V)
$V_{SD,po}$	Pinch-off voltage (V)
V_t	Threshold voltage (V)
W	Width (m)

INTRODUCTION

The early and personalized detection of diseases, securing food safety and environment monitoring are critical tasks of our society that demand a reliable sensing of biological and chemical species. To a very large extent the analyses in these areas are performed *via* costly, time consuming and laborious methods, such as enzyme-linked immonosorbent assays (ELISA),[1,2] polymerase chain reaction (PCR)[3,4] or gas chromatography-mass spectrometry (GC-MS),[5,6] that have to be performed in accordingly equipped, central laboratories by trained personnel.[7]

In the 1990s the idea to scale down all functionalities of a laboratory to the size of a transportable (micro) chip – to have a *lab on a chip* (LoC) which can be used at the *point of care* – became prominent. Initial works by Terry *et al.*[8] who introduced a highly miniaturized gas chromatograph in 1979 and Manz *et al.*[9] who published a theoretical article about miniaturized total chemical analysis systems (mTAS) in 1990 were the starting points of the LoC development. One key aspect of the LoC approach is to use the technologies developed in microelectronics industry not only for miniaturizing the components of integrated electronic circuits, but also for miniaturizing the sizes of fluidic handling systems. Such fluid channels with dimensions in the micrometer range – so-called *microfluidic* systems – drastically reduce the required sample volumes. Built-in miniaturized valves,[10,11] electrodes,[12] mixers,[13] switches[14] or heaters[15] enable a large degree of automation. The low power consumption of such systems further enhances their cost efficiency.[16,17]

Concerning their cost and time efficiency as well as their integratability, sensor devices implemented in LoC systems are required to detect analytes without a previous chemical labeling. Additional optical components, as in surface plasmon resonance-based devices,[18] should be avoided. Furthermore, high sensitivities and specificities towards the analytes of interest need to be achieved. For meeting these requirements, the introduction of a silicon nanowire (SiNW) field-effect transistor (FET) based biosensor by Lieber *et al.*[19] in 2001 was an important milestone. The idea to use FETs for analyte sensing goes back to the invention of ion sensitive field-effect transistors (ISFETs) by Bergveld in 1970.[20] He showed that the ion or charge density at the interface between a liquid and the gate oxide of a FET influences the FET resistance. By modifying the sensor surface with particular (bio) receptor molecules – such as antibodies,[21–24] DNA[25] or aptamers[26,27] – only specific analytes will adhere to the surface and induce a signal change. Scaling down the semiconducting part to nanometer dimensions by using NWs largely enhances the surface to volume ratio, and, thus, the sensitivity of the devices. SiNW devices are used for detecting pH[19,28,29] and for label-free real-time monitoring of chemicals,[19,30,31] proteins[19,22–24,32,33] and DNA[34] with detection limits down to the fM range. Having nanoscale sensing structures with sizes comparable to the analytes even enables the detection of single species.[35]

The required nanoscale semiconductors can be fabricated "bottom-up" or "top-down". Bottom-up grown SiNWs pose a cost efficient alternative to top-down nanoscale devices which are commonly fabricated *via* time consuming, costly electron-beam lithography (EBL). In a single chemical vapor deposition (CVD) run innumerable SiNWs are grown. Bottom-up fabricated SiNWs possess a low defect density,[36–38] offer competitive electronic properties compared to top-down devices,[39] and are easily transferred on polymer substrates for fabricating flexible sensors.[40] Therefore, bottom-up SiNW-based sensors are of high research interest at the Chair of Materials Science and Nanotechnology of Prof. Cuniberti at the TU Dresden, where this thesis is prepared.

Within this thesis, the focus lies on the development of novel strategies towards fabricating LoC analysis devices based on bottom-up SiNW FETs. Novel approaches at various length scales in LoC fabrication are established, ranging from micrometer over nanometer scale down to the molecular level. The aim is to facilitate the production of highly sensitive and selective LoC analysis devices from various directions. After introducing the fundamentals for this work in **chapter 1**, **chapter 2** describes a novel approach for the rapid prototyping of PDMS-based microfluidics which can easily be assembled reversibly onto virtually any kind of substrate. Additionally, the potential of such microfluidic devices for the patterned deposition of versatilely structured, flexible electronics and uniquely shaped 3D polymer microstructures is demonstrated. In **chapter 3,** a new surface functionalization strategy for immobilizing receptor molecules without additional binding site passivation is described. The fabrication of sensors based on arrays of bottom-up SiNW FETs, their pH and ion sensitivity and their utilization as biosensors is presented in **chapter 4**. Due to evidence that the highest analyte sensitivities are achieved when employing single-NW devices,[32] in **chapter 5** a novel approach for reliably aligning and positioning bottom-up 1D nanostructures at predefined positions *via* microfluidic traps is developed. At the beginning of each chapter describing novel fabrication strategies, the respective investigations are motivated.

1 FUNDAMENTALS

Developing a chip card-sized analysis laboratory is a highly interdisciplinary task. It involves the fabrication of electronic circuits and fluid handling systems at the micrometer scale and the inclusion of a highly sensitive and selective sensor device. Within this thesis, bottom-up SiNW FET-based LoC devices are built.

At the beginning of this chapter, in section 1.1, the fundamentals of UV-lithography are explained, as it is the main (micro-)fabrication tool utilized within this work. Throughout the thesis, various kinds of PDMS-based microfluidic devices are developed, built and used, the fundamentals of which are described in section 1.2. Section 1.3 explains the working principles of FETs and how they can be applied for sensor applications. Means of making FET-based sensors specific towards particular analytes *via* surface functionalization are summarized in section 1.4.

1.1 UV-LITHOGRAPHY

UV-lithography (UVL) is a standard procedure in top-down integrated circuit technology for a patterned etching or deposition of materials.[41] Within this work, UVL is used for different objectives. Patterned photoresist films serve as mold for the fabrication of microfluidic channels (see chapters 2 and 5). Patterns of differently functionalized surfaces are created (see chapter 3). And a localized etching of SiO_2 with subsequent lift-off-based localized metal deposition is performed (see chapters 4 and 5).

The first step in UVL is the deposition of a thin photoresist film on a substrate *via* spin coating (step A in Fig 1.1a). In a subsequent baking step the solvents of the resist are evaporated (step B). Then a photomask is placed on top of the film and the stack is exposed to UV-light (step C). The photomask consists of transparent and nontransparent parts which
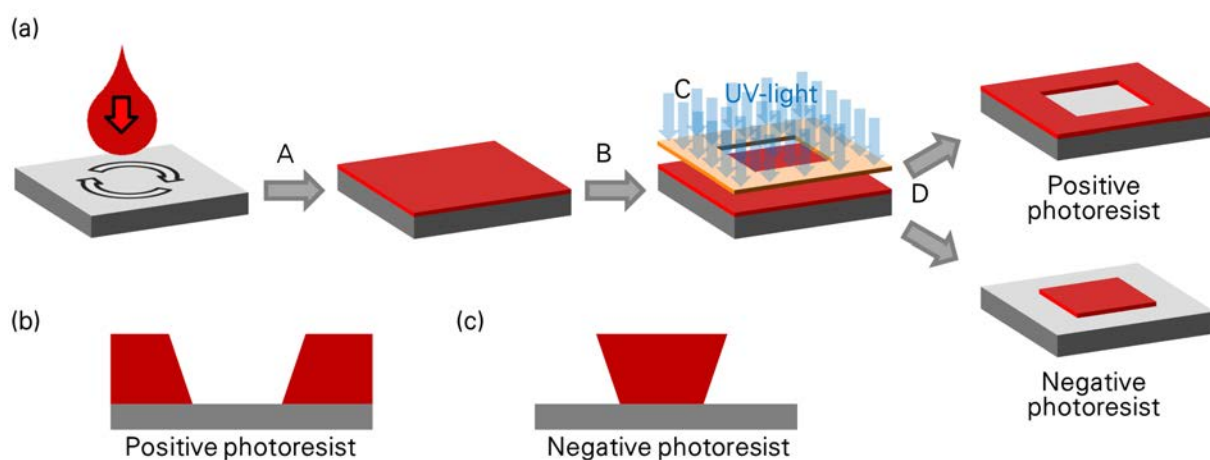

Fig 1.1: (a) Basic steps of UV-lithography microfabrication: A - spin coating, B - prebaking, C - UV-exposure through a photomask, D - development. (b) Typical Sidewall slope of positive photoresist. (c) Typical undercut of negative photoresist.

determine the pattern that the photoresist will form at the end of the procedure. For positive photoresists, the UV-illuminated parts of the film are rendered much more soluble than the non-illuminated parts during immersion in the developer solution (step D).[42] For a negative photoresist it is the opposite. Commonly, negative photoresists require a post exposure bake before their development. There are image reversal photoresists which can be chemically changed from a positive to a negative resist by a post exposure bake and a second UV-illumination of the entire surface before development.

The minimum feature size depends on the wavelength of the UV-light and the chemical composition as well as the film thickness of the photoresist.[41,42] The side walls of the developed patterns can either have a slope as shown in Fig 1.1b, for positive photoresists, or present an undercut as shown in Fig 1.1c, for negative photoresists.[42] A wide undercut is intended for patterned metal depositions, because it prevents the side walls from being coated with a metal film so that the subsequent lift-off is facilitated. However, for soft lithography procedures, the undercut must be minimized for not rupturing the master structure when the cast polymer is peeled-off (see sections 1.2 and 2.2.1). Slope and undercut mainly depend on the exposure dose during UV-illumination of the photoresist.[42] The dose has to be optimized accordingly.

1.2 PDMS–BASED MICROFLUIDIC DEVICES

In the field of *microfluidics*, fluid flows are controlled and manipulated in channel systems with dimensions in the micrometer range.[16,17] As opposed to macroscopic systems, fluid volumes down to the femtoliter range can be manipulated accurately which provides the advantage that only reduced amounts of precious samples and chemicals are required.[16] Due to the reduced channel sizes, the influences of surface forces such as capillary effects become dominant over volume forces of the fluids, *e. g.* gravity.[17] Inertia is less important than viscosity.[16]

The ratio of inertial forces and viscous forces is expressed by the dimensionless Reynolds number

$$\text{Re} = \frac{\rho u L}{\eta} \tag{1.1}$$

where ρ is the density, u the velocity and η the dynamic viscosity of the fluid, and L the characteristic length of the channel. In wide channels, at high $Re > 2500$, the flow regime is considered turbulent. In microfluidic devices with low $Re < 1$, there is a strictly laminar flow, free of turbulences,[16,17] which substantially enhances the control of concentrations of molecules in space and time.[16]

Benefiting from the developments in the production of integrated electrical circuits, there are various fabrication and design possibilities for microfluidic devices. The large scale

integration of fluid handling systems provides at least up to 50-fold sample economy compared to conventional preparation systems like 96-well plates.[43] High throughput microfluidics enable processing up to 10^6 samples in parallel.[44,45] Demonstrated applications of microfluidic devices include cell growth studies,[46] manipulation and study of single cells [47] and single molecules,[48] droplet formation [49,50] and droplet-based synthesis of (smart) microcapsules (see also section 1.2.1),[51–53] fabrication of fibers [54] and spray dried nanoparticles,[55] trapping of particles [56] and cells (see also section 1.2.2),[57] high-throughput screening in drug development,[58,59] and bioanalysis [9,60,61] among others. All these examples imply that tasks which are usually performed in macroscopic set-ups in a laboratory can be condensed and miniaturized to micro-scaled *lab on a chip* (LoC) applications. Compared to macroscopic set-ups the accuracy of sample handling is increased and temperature control and homogeneity over the fluid volume is enhanced. Regarding the analyses of biological or chemical species the miniaturization to "miniaturized total chemical analysis systems" (mTAS) [9] enables the utilization of the test devices at the *point of care*, with reduced costs per test and shorter time-to-result.[45]

Driving the fluid through the channel system is achieved by pressure gradients, capillary effects, electric fields, magnetic fields, centrifugal forces or surface acoustic waves.[17,45] For further manipulating the flow, miniaturized pumps [62] and valves [10,11] are implemented into the systems. Special mixer set-ups are utilized to disturb the laminar flow regime and accelerate the normally only diffusion-driven mixing of fluids.[13,63,64]

The first microfluidic devices were made from silicon or glass using microelectronics (etching) processes. However, rapid prototyping of channel structures, which is particularly important in academia, requires faster and cheaper production methods. Whitesides *et al.*[65] introduced in 1997 the replication of (channel) structures *via* soft lithography. A mold with the negative of the intended channel structure is prepared, *e. g. via* UVL (see Fig 1.2a and section 1.1). Then a prepolymer is cast on top and cured (Fig 1.2b) before it is peeled off and inlet holes are punched (Fig 1.2c). Afterwards tubing is attached and the channel is sealed with a flat substrate (Fig 1.2d) to obtain a microfluidic device. The mold can be replicated multiple times which makes the approach very cost-efficient.
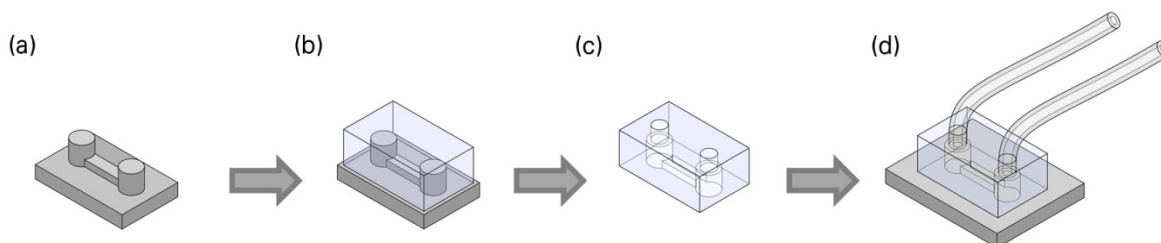

Fig 1.2: Basic steps of microfluidic device fabrication via soft lithography. (a) Preparation of mold (*e. g. via* UVL). (b) Casting and curing polymer on mold. (c) Peeling off polymer stamp and punching inlet holes. (d) Attaching tubing and sealing channels with flat substrate.

One of the most often used polymers for the rapid prototyping of microfluidic devices is polydimethylsiloxan (PDMS), due to its advantageous properties. PDMS is a soft, optically transparent elastomer with low toxicity and with permeability to gases, such as CO_2 and O_2, making it particularly attractive for biological applications.[16,66] The elasticity of the material enables a simple soft lithographic fabrication of pneumatically actuated pumps,[10] valves [10,11] and mixers.[67] Commercially available preparation kits (*e. g.* Sylgard 184, Dow Corning, USA) which contain the required oligomer-base and a cross-linking agent are utilized for a fast, cost-efficient stamp fabrication.

The mixing ratio of base and curing agent allows adjusting the polymer flexibility. With the standard mixing ratio of 10:1 ($w_{base}/w_{curing\ agent}$), stable fluid channels with dimensions in the nanometer range [68] and with width to height ratios of 10:1 can be fabricated.[69] The more curing agent is applied, the more crosslinking between the prepolymer building blocks occurs. Thus, the less flexible the cured PDMS will become,[70] and higher aspect ratios can be realized without risking a collapse of the fluid channels.

At room temperature the cross-linking time is at least one day. Increasing the curing temperature decreases the required curing time, however, induces internal stresses and, thus, deformation of the PDMS stamp.[71] Deformations of PDMS stamps are also induced by many organic solvents which dissolve and swell the polymer.[72]

Commonly, to seal the microfluidic channels, PDMS is bonded *irreversibly* (covalently) on silicon wafer substrates after an oxygen plasma treatment.[66] A weaker, however, *reversible* sealing is achieved without plasma treatment, based on the self-adhesion of PDMS to other surfaces.[66,73] The reversible sealing can be supported by mechanical clamps,[74–76] permanent magnets,[70] glass-PDMS-glass sandwich arrangements,[77] or by aspiration *via* vacuum in additional channel structures within the stamp.[78] A novel strategy for fabricating multifunctional reversibly sealable microfluidic devices is described in chapter 2.

Within this work investigations in the field of droplet microfluidics (see chapter 2) and in the field of microfluidic trapping of one-dimensional (1D) nanostructures are performed (see chapter 5). The following two sections introduce the backgrounds of the respective fields of research.

1.2.1 Droplet microfluidics

The formation of droplets of one fluid inside another immiscible fluid *via* microfluidic devices dates back to the early 2 000s when Thorsen *et al.*[49] and Anna *et al.*[50] used soft lithography-based T-junction or flow focusing microstructures (see Fig. 1.3), respectively, to emulsify water droplets in a continuous oil stream. Since then, droplet microfluidics has been used in a plethora of applications ranging from investigations on reaction kinetics [79] and protein crystallization [80,81] to smart material synthesis,[51–53] single cell analysis,[82,83] polymerase chain

reaction (PCR),[84,85] and high throughput-screening technologies,[86] among others. There are several review articles on droplet microfluidics.[51,87]

Compared to continuous flow microfluidics, in droplet microfluidics the fluid stream is compartmentalized *via* an additional immiscible fluid resulting in a segmented flow regime. Up to several ten thousands of uniformly shaped droplets are generated within seconds.[88] Each of them can be controlled and manipulated independently allowing the parallel processing of up to 10^6 nano and femtoliter-sized mini reactors in which samples are mixed, treated and analyzed individually.[45,89,90]

Fig. 1.3 schematically depicts the fabrication of droplets using a T-junction

(a) T-junction configuration

(b) Flow focusing configuration

Fig. 1.3: Schematic drawing of droplet formation configurations. A discontinuous, discrete phase, *e. g.* water, is introduced into a continuous phase, *e. g.* oil, *via* (a) T-junction or (b) flow focusing arrangements.

flow configuration. A continuous fluid phase, *e. g.* oil, flows along the main channel of the structure. An immiscible fluid, *e. g.* water – the subsequent discontinuous, discrete phase – enters the main channel *via* an orthogonal channel. At the junction of main and inlet channel, the immiscible fluids form an interface.[91] As the portion of the discrete phase in the main channel grows, a droplet begins to form.[91] The droplet is distorted and pushed *via* shear forces by the continuous phase downstream along the main channel.[91] When the upstream interphase of the droplet reaches the downstream edge of the inlet channel, the neck of the discrete phase thins so that the droplet breaks off and is carried downstream within the continuous phase.[91] In the flow focusing configuration, depicted in Fig. 1.3b, the discrete phase enters from the central channel while the continuous phase is introduced from the two side channels. Due to shear forces imposed by the stream of the continuous phase, the stream of the discrete phase is focused in the narrow orifice. In a highly periodic break-up of the discrete phase dispersions with droplets of narrow size distribution are formed.[50]

The size of the formed droplets is determined by (i) the size of the orifice of the T-junction or flow-focusing nozzle, (ii) the viscosity of the immiscible phases, (iii) the use of surfactants, and (iv) the hydrophilicity or hydrophobicity of the channel surface.[87]

Within this thesis a T-junction configuration with a UV-curable adhesive as continuous and water as discrete phase, is used to fabricate uniquely shaped 3D polymer structures (see chapter 2).
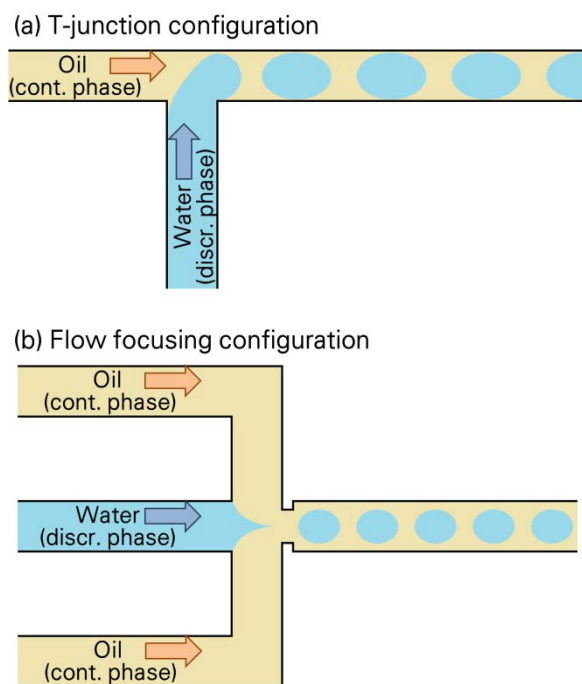
1.2.2 Microfluidic trapping

Microfluidic trapping is achieved by implementing obstacles in the fluid stream that allow the carrier phase to pass while capturing the objects of interest. One design of such obstacles is depicted in Fig 1.4a.[57] Partially opened U-shaped pockets with the upper part of the U facing against the fluid flow are used for trapping single cells. Once a pocket is filled with a cell, the fluid mainly streams around the trapping site so that any further cells pass on to the next trapping sites.

Another trapping layout is shown in Fig 1.4b.[56] The structure is designed in such way that the fluid flow resistance through the trapping site and its narrow side channel is lower than along the broad main channel. Thus, particles are aspirated into the side pockets. After trapping the particle, the flow resistance along the respective channel side arm is drastically increased redirecting the main flow along the main channel. One after the other, every trapping site is filled with one particle. There are similar trapping layouts for capturing cells.[92]

The above-described trapping layouts are designed for capturing ellipsoidal micrometer-sized particles and cells. For the trapping of 1D nanostructures investigated within this thesis, other device designs are required (see chapter 5).
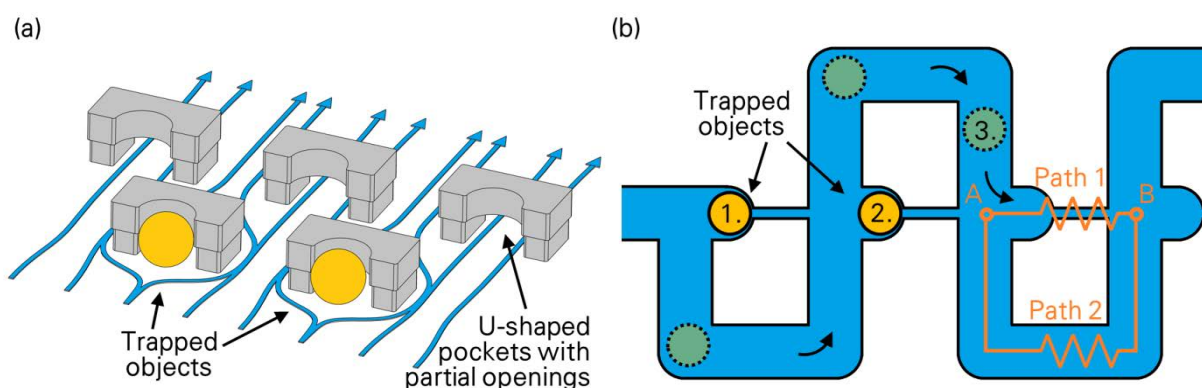
Fig 1.4: Schematic drawings of microfluidic trapping sites for micrometer-sized cells or particles. (a) U-shaped pockets with partial openings (gray) capture the respective objects (orange). Subsequently, the streamlines (blue) of the fluid mainly pass around the blocked trapping sites.[57] (b) Trapping *via* aspiration. Flow resistance between point A and point B along path 1 is lower than along path 2. One trapping site after the other is filled and its opening to the narrow side channel, *i. e.* path 1, blocked.[56]

1.3 FIELD-EFFECT TRANSISTORS

The first physical realization of a transistor is a Noble Prize-winning invention from 1947.[93] Transistors (short for *transfer-resistor*) are semiconductor devices which are used for amplifying and switching electronic signals. In microelectronic industry they are the key components in all integrated circuits. Worldwide about 2.5×10^{20} transistors were produced in 2014 – about 25 times the number of stars in the Milky Way.[94] It is assumed that one conventional transistor costs about as much as one character in a printed newspaper.[95]

Within this work, silicon nanowire (SiNW) based Schottky-barrier field-effect transistors (SB FETs) are built and utilized as bio-sensors. Using transistors for sensor applications is part of a new development commonly called "More than Moore" where micro- and nanoelectronic technologies are merged with non-digital functions.[95] The advantages of SiNW-based sensors will be highlighted in section 4.1. In the following sections, for ease of understanding, first, the fundamental working principle of FETs is introduced using the example of "dry" metal-oxide semiconductor field-effect transistors (MOSFETs, section 1.3.1). Then, the working principle of their "wet" counterparts, the ion sensitive ISFETs, is explained (section 1.3.2). In section 1.3.3 the fundamentals of SB FETs are described and similarities and differences to MOSFETs are discussed. In the last part, section 1.3.4, the influences of charge traps in a FET on the device characteristics are outlined. For a more detailed description on the principles of FET devices the reader is referred to standard literature such as references [96–99].

1.3.1 MOSFET

In Fig. 1.5, a schematic of a typical silicon-based *n*-channel MOSFET is depicted. Two heavily *n*-doped regions, *source* and *drain*, are integrated in a *p*-type substrate. On top of the device, in-between the source and drain contacts, there is an insulating oxide layer covered by a *gate* metal contact. One additional contact is connected to the bulk. Applying different gate voltages, V_G, puts the FET in different operation modes (Fig. 1.5a-c). In the cut-off mode (Fig. 1.5a), *i. e.* when V_G stays below the threshold voltage, V_t (further discussed below), the *n*-doped regions are electrically insulated by a potential barriers at the *p-n*-junctions which inhibit charge carrier movement. Source drain currents, I_{SD}, only flow *via* thermal activation of charge carriers. At V_G above V_t, an inversion layer of mobile electrons is formed towards the oxide interface (Fig. 1.5b). A conducting channel between source and drain develops, so that the FET behaves like an Ohmic resistor, with a linear dependence between drain current, I_{SD}, and source drain voltage, V_{SD}. When V_{SD} is raised above the pinch-off voltage (Fig. 1.5c), $V_{SD,po} = V_G - V_t$, the gate-to-channel voltage at the end of the channel falls below V_t so that the inversion layer disappears. The channel is pinched-off and I_{SD} saturates.

The different operation modes of MOSFETs are visible in their output characteristics (Fig. 1.5d) and their transfer characteristics (Fig. 1.5e). In the Ohmic mode, the output current rises linearly with V_{SD} (Fig. 1.5d). At high V_{SD} the current saturates due to the pinch-off of the channel. The transfer characteristics of a FET are depicted as a linear plot and as a semi-logarithmic plot (Fig. 1.5e). In the subthreshold or cut-off regime, respectively, the current is temperature dependent and rises exponentially with V_G.

$$I_{SD} \sim \exp\left[\kappa \, \frac{qV_G}{kT}\right] \qquad\qquad (1.2)$$

where *q* is the elementary charge and *kT* is the thermal energy of the charge carrier with *k*

as Boltzmann constant and T as absolute temperature. The factor, κ, describes the effectiveness of gate coupling, which is discussed in more detail in section 1.3.4. The inverse slope of the semi-logarithmically plotted transfer curve, the subthreshold swing S, is an important characteristic describing how efficient a FET can be switched.
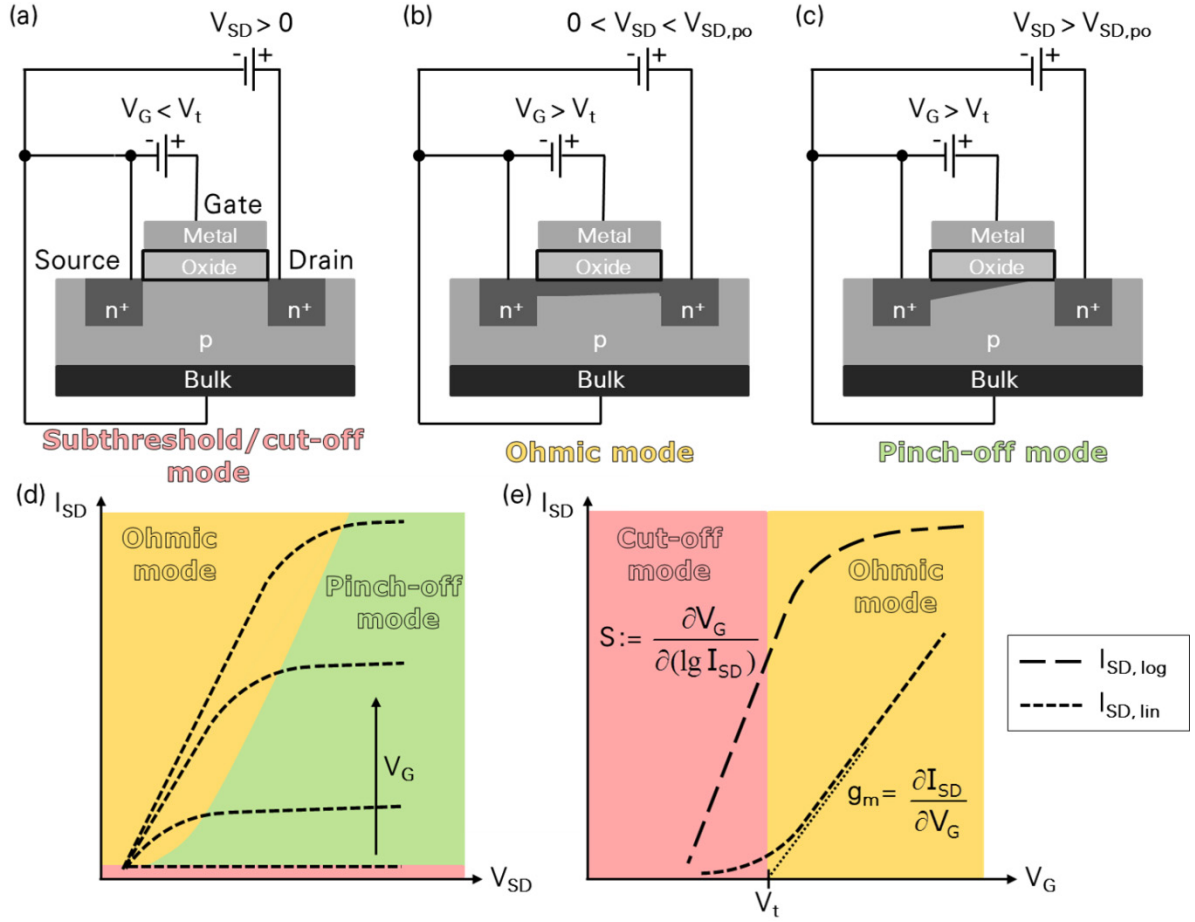
Fig. 1.5: (a) Schematic of a typical *n*-channel MOSFET. Two heavily *n*-doped semiconductor regions, *source* and *drain*, are integrated in a *p*-type semiconducting substrate. On top of the device, there is an insulating oxide layer covered by a metal *gate*. Depending on gate the voltage, V_G, applied between source and gate, the device specific threshold voltage, V_t, and the source drain voltage, V_{SD}, different source drain currents, I_{SD}, and different modes of operation are adjusted. In the cut-off or subthreshold mode, $V_G < V_t$, the *n*-doped regions are isolated from each other by potential barriers at the *p-n*-junctions towards the *p*-region. I_{SD} only flows *via* thermal activation of charge carriers. (b) At $V_G > V_t$, an inversion layer of mobile electrons is formed adjacent the oxide. An electron conducting channel between source and drain develops. The FET behaves like an Ohmic resistor (Ohmic mode). (c) At V_{SD} above the pinch-off voltage, $V_{SD,po} = V_G - V_t$, the conducting channel is pinched-off (pinch-off mode) and saturation takes place. (d) Output chracteristics (I_{SD} vs. V_{SD}) of MOSFET for different V_G. Different modes of operation indicated by different background colors. (e) Transfer characteristics (I_{SD} vs. V_G) of MOSFET plotted in linear and logarithmic scale. In the Ohmic mode I_{SD} depends linearly on V_G. The slope of the curve is called transconductance, g_m. The intersect voltage of the linearly fitted transfer curve with $I_{SD} = 0$ is commonly defined as V_t. In the cut-off or subthreshold mode I_{SD} depends exponentially on V_G. The inverse slope of the semi-logarithmic plot is called subthreshold swing S.

$$S := \frac{\partial V_G}{\partial (\lg I_{SD})} = \frac{1}{\kappa} \frac{kT}{q} \ln(10) = \frac{1}{\kappa} \, 59 \text{ mV/dec} \, \frac{T[K]}{300} \qquad (1.3)$$

At room temperature, in case of a maximum gate coupling ($\kappa \rightarrow 1$), the minimum swing is approx. 59 mV/dec.

Another important characteristic determining the quality of an FET is the ratio between the I_{SD} in the *on-* and in the off-state of the device. A high on/off ratio (I_{on}/I_{off}) commonly arises from low leakage currents in the off-state and a high current gain in the *on*-state.

In the Ohmic mode, the ideal expression for the source drain current, I_{SD}, is:

$$I_{SD} = C_{Ox} \, \mu \, \frac{W}{L} \left[V_G - V_t - \tfrac{1}{2} V_{SD} \right] V_{SD} \qquad (1.4)$$

C_{Ox}, the capacitance of the gate oxide per unit area, μ, the electron mobility in the channel and W and L, the width and length of the channel, respectively, are considered as fixed values in a fabricated FET device. For MOSFETs also the threshold voltage is a constant

$$V_t = \Phi_M - \Phi_{Si} - \frac{Q_{Ox} + Q_{SS} + Q_D}{C_{Ox}} + 2 \, \Phi_f \qquad (1.5)$$

composed of the workfunction of the gate metal, Φ_M, the workfunction of silicon, Φ_{Si}, the accumulated charge in the oxide, Q_{Ox}, the accumulated charge at the oxide-Si interface, Q_{SS}, the depletion charge in silicon, Q_D, the gate oxide capacitance per unit area, C_{Ox}, and the onset of inversion, expressed in the last term of equation (1.5), $2 \, \Phi_f$, which depends on the doping level of the channel.

1.3.2 ISFET (ChemFET, BioFET)

In Fig. 1.6 a schematic of an ISFET is shown. As opposed to MOSFETs, in ISFETs the gate oxide is not covered by a metal, but by a liquid contacted to a reference electrode instead.[20,98] In this *liquid gate* set-up, by means of the reference electrode, the FET is gated similarly to a MOSFET. The threshold voltage of the FET, however, is not a purely device related constant, as it would be the case for MOSFETs. For ISFETs, equation (1.4) changes to

Fig. 1.6: Schematic drawing of ISFET set-up. As opposed to a MOSFET the gate oxide is not covered by a metal gate electrode, but by a liquid solution instead, with reference electrode inside. This liquid gate arrangement allows steering the FET.

$$V_t = E_{ref} - \Psi + \chi^{sol} - \Phi_{Si} - \frac{Q_{Ox} + Q_{SS} + Q_D}{C_{Ox}} + 2 \, \Phi_f \qquad (1.6)$$

Here, the (stable) potential of the reference electrode, E_{ref}, substitutes the workfunction of the metal, and the term $\Psi + \chi^{sol}$ describes the potential at the interface between liquid and
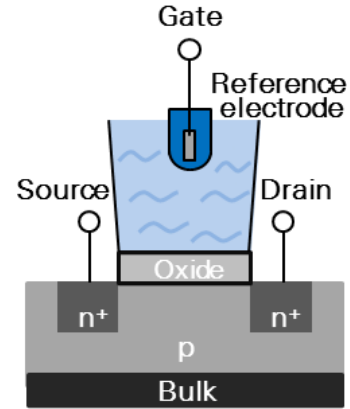
gate oxide. The surface dipole potential, χ^{sol}, has a constant value. The surface potential, Ψ, however, depends on the pH of the liquid, as well as the concentration and the type of other ions dissolved in it.

According to the site-binding model,[100,101] the hydroxyl groups at the surface of the gate oxide can be protonated or deprotonated and, thus, be positively or negatively charged, respectively. At the interface the charge of the liquid solution is opposite to the charge on the oxide surface. An electrochemical double layer is formed. Based on the Gouy-Chapman-Stern model [29,102–104] the dependence of the resulting surface potential on the pH of the solution is described by

$$\Delta\Psi = -2.3\, \alpha\, \frac{RT}{F} \Delta pH_{solution} \qquad \| \qquad \alpha = \frac{1}{(2.3\, kT/q^2)(C_S/\beta_S) + 1} \qquad (1.7)$$

where R is the universal gas constant, F is the Faraday constant, C_S is the differential double-layer capacitance and β_S is the surface buffer capacitance of the oxide, *i. e.* the ability of the surface to take up or deliver protons. Only for sensitivity factors, α, close to 1 a Nernstian pH-sensitivity of 59.5 mV/pH (at 300 K) is achieved. Different kinds of gate oxides provide different sensitivities. Near Nernstian sensitivity is reported for devices covered with Al_2O_3,[29] HfO_2 [105] and Ta_2O_5,[98] respectively. For SiO_2 covered ISFETs sub-Nernstian pH-sensitivities between 35 and 45 mV/pH are reported.[29,106,107]

Commonly, the sensitivity of the ISFET for other ions is also explained with the site-binding model.[98] Latest findings by Tarasov *et al.*[108] indicate that there is a direct interaction between hydroxyl surface groups and adsorbed anions. In a surface complexation reaction anions from the solution replace previously adsorbed protons, which induces a change of the surface potential.

In general, independent of the charge of a chemical or biological species, there is a change of the surface potential upon its adsorption to the ISFET surface. Also the blocking of binding sites with uncharged molecules influences the sensor signal distinctly.[109] Therefore, ISFETs are ideal signal transducers for the detection of all sorts of analytes. To ensure that there is only a specific interaction with one particular analyte, the oxide surface is chemically modified, which is explained in more detail in section 1.4. Depending on the target analyte there are also other abbreviations for FET-based sensors, such as ChemFET or BioFET, for the particular detection of chemical or biological species, respectively.

The change of the surface potential results in a shift of the transfer characteristics, which can be monitored, *e. g. via* continuous gate sweeping, as demonstrated by Zörgiebel *et al.*[28] Within this work, if not otherwise stated, the change of the surface potential is monitored by measuring ΔI_{SD} of the FETs at constant V_G and constant V_{SD}. Subsequently, the measured data are used to calculate ΔV_t, which is explained in detail in section 4.3.3.1.

1.3.3 SB FET

Within this work SiNW-based SB FETs are fabricated in cooperation with the NaMLab gGmbH, Dresden. A schematic of the devices is given in Fig. 1.7a (detailed description of the fabrication process in section 4.2). Intrinsic SiNWs connect Ni source and drain electrodes. Emerging from the Ni electrodes atomically sharp, metallic $NiSi_2$ leads are formed towards the Si part of the NW. The $NiSi_2$-Si Schottky barriers at the contacts determine the FET characteristics. The NW is surrounded by an oxide shell and is placed on top of the oxide layer of a Si wafer. In this silicon on insulator arrangement the SB FET is steered *via* a common back-gate, *i. e.* the substrate.

Fig. 1.7b shows typical transfer curves of a SB FET produced within this thesis as semi-
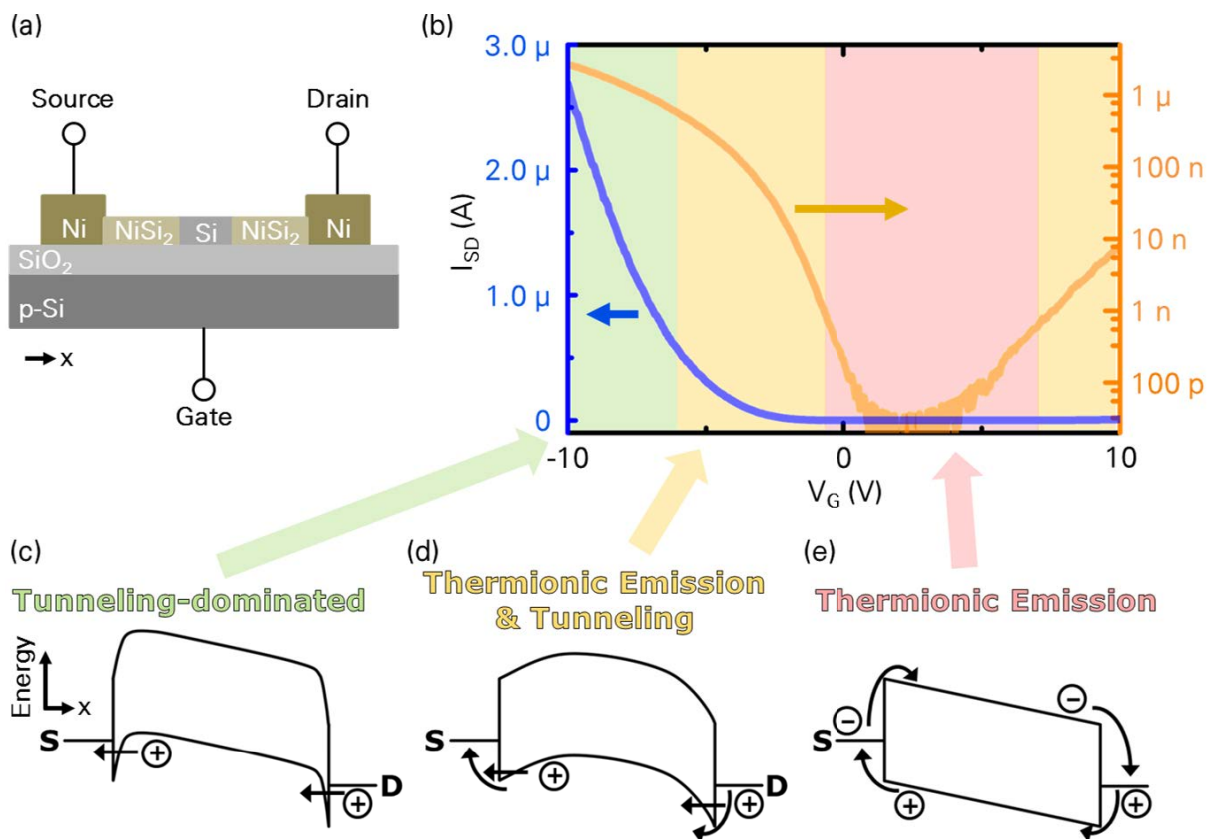
Fig. 1.7: (a) Simplified schematic of a SiNW SB FET as produced within this thesis. Two Ni *source* and *drain* electrodes are connected *via* SiNW. Atomically sharp $NiSi_2$ leads are formed at both ends of the Si part. A common back-gate steers the device. The $NiSi_2$-Si Schottky barriers at the contacts determine the FET characteristics. (b) Transfer characteristics of one device fabricated within this thesis, recorded at $V_{SD} = 1$ V, plotted in linear (blue) and semi-logarithmic (orange) scale (V_G sweep from -10 V to +10 V shown). The device shows ambipolar behavior. (c) Schematic drawing of the band structure of the SB FET at high negative gate voltages, V_G. The SBs are thinned out strongly so that holes mainly tunnel through the SBs at drain (D) and source (S). (d) At intermediate negative V_G the SBs are not thinned out as strongly, so that both tunneling and thermionic emission of holes occur to similar extent. (e) Without external electric field only thermionic emission – of holes and electrons – takes place. In (a), (c), (d) and (e) *x* represents the coordinate for space.

logarithmic and linear plot. It is visible that SB FETs behave similar to MOSFETs. However, the gating is based on different mechanisms. MOSFETs, are single crystalline devices with differently doped sections. When raising V_G, the external electric field lowers (at $V_G < V_t$) or removes ($V_G > V_t$) the potential barriers at the *p-n* junctions so that electrons move unhindered through the lattice from source to drain. In SB FETs, the SB height at the metal-semiconductor interface is fixed for a specific device. The SB height is influenced by utilized materials, interface properties and internal strains,[110] among others. For NiSi₂-Si interfaces the SB height is approx. 0.66 eV for electrons and 0.46 eV for holes.[111] An external electric field cannot remove the barriers, it just bends the energy bands of the silicon part. Fig. 1.7e shows the band diagram of the SB FET in case there is no external electric field. The charge carriers overcome the SBs by thermionic emission.[110] In case of a strong external electric field, the SBs are strongly thinned out (see Fig. 1.7c) so that charge carriers with low thermal energy can tunnel through the barriers and current flow increases. Thus, at large negative V_G, the tunneling of holes is the dominating mechanism for injecting charge carriers into the Si. At intermediate negative V_G, tunneling and thermionic emission occur to similar extend (see Fig. 1.7d).

For the NiSi₂-Si SB FETs built within this thesis, at positive V_G electrons can tunnel as well, which explains the ambipolar behavior of the device and the current increase at $V_G \geq 5$ V. By means of two separate top gate electrodes on top of both SBs of the FET, precise control over hole and electron transport is possible. This is exploited for building reconfigurable logic switches at the NaMLab gGmbH.[110,112]

Within this work, the SB FET devices are passivated with an oxide layer, and then implemented in a microfluidic set-up for ISFET/sensing applications, which is described in detail in section 4.2. The SB FETs react in a very similar way to surface potential changes as described for MOSFET/ISFET platforms before (see section 1.3.2).

1.3.4 Gate coupling and charge trapping

In equation (1.2) and (1.3), the factor κ is introduced for describing the effectiveness of gate coupling of FET devices, *i. e.* how effective an applied V_G steers the FET resistivity. The factor is determined by the gate oxide capacitance, C_{Ox}, and by the depletion capacitance, C_D, based on the following simplified equation.

$$\kappa = \frac{C_{Ox}}{C_D + C_{Ox}} \tag{1.8}$$

For a maximum gate coupling ($\kappa \to 1$) the oxide capacitance must be much larger than the depletion capacitance, hence, low channel doping and thin oxide thickness are desired.

In addition to that, defects at the oxide-Si interface and within the oxide-bulk are of great importance. Stretched bonds, dangling bonds and other faults, *e. g.* due to lattice

mismatches, enable the trapping of charges during device operation.[113] Depending on the applied V_G, charges can go from the Si-channel into trapping sites, or the other way around, *via* tunneling or thermal activation.[114,115] Also a charge exchange between trapping sites is possible. There are charge traps with low stability or short lifetimes (1 - 10 μs), respectively, commonly at the direct oxide-Si interface,[116,117] and charge traps with longer lifetimes (~ 1 s), commonly in the oxide bulk.[116]

Equations (1.5) and (1.6) show that charges inside the oxide and at the oxide-Si interface influence V_t. Depending on trap lifetimes and V_G sweeping speed, charge trapping leads to hystereses in the transfer characteristics of the devices. The additional charges also reduce the gate coupling as they screen the applied electric field. This effect is considered by introducing an interface-trap capacitance, C_{it}, and rewriting equation (1.8) as [99]

$$\kappa = \frac{C_{Ox}}{C_D + C_{Ox} + C_{it}} \qquad (1.9)$$

Incorporation of water molecules in the gate oxide during device fabrication is also considered as a possible origin of for charge traps with long lifetimes.[118,119]

The occurrence of defects in the gate oxide can be prevented by an appropriate passivation, such as a thermal growth of high quality oxides.[99,120] Furthermore, a subsequent annealing treatment in forming gas for saturating Si dangling bonds with hydrogen atoms should be included.[99,120]

1.4 SENSOR SPECIFICITY

As described in section 1.3.2 the surface potential of FETs and, hence, the device resistivity is influenced by all sorts of chemical and biological species which adhere to their oxide surfaces. Consequently, FETs are suitable transducers for a broad range of (bio)sensor applications. However, to obtain a sensor which is specific for one particular analyte, the surface has to be modified and/or functionalized.

Biosensors are defined as devices "that use specific biochemical reactions mediated by isolated enzymes, immunosystems, tissues, organelles or whole cells to detect chemical compounds usually by electrical, thermal or optical signals".[121] In this section, the fundamentals of surface modification are discussed. The described approaches are focused on FET-based sensors in which the specificity is achieved by immobilizing receptor molecules on the transducer surface. The reader is referred to standard literature such as references [122–124] and review articles such as references [125,126] for further functionalization strategies on a wider field of sensor types.

1.4.1 Receptor molecules

A (bio)receptor is a molecule that interacts specifically with an analyte *via* the key-lock-principle – a non-covalent interaction based on a complex interplay of hydrogen bonds, salt bridges, hydrophobic interactions, van der Waals forces, electrostatic interactions and structural fitting.[124] The aim of a sensor surface functionalization is to exploit these specific interactions. Receptors are attached to the sensor surface so that only one particular analyte is attracted to go and stay there – always based on the equilibrium [127]

Fig. 1.8: Schematic drawing of an IgG antibody. The Y shaped protein consists of one Fc domain (**f**ragment that **c**rystallizes) and two Fab domain (**f**ragments for **a**ntigen **b**inding).

analyte + receptor ⇌ analyte-receptor complex
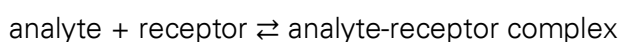
Then, ideally, any sensor signal exclusively depends on the presence or absence of the specific target molecule. The background noise due to unspecific adsorption of other species is minimized.

Commonly applied bio-receptors are antibodies[128] or fragments of antibodies,[21] other proteins,[129] enzymes,[130] single stranded DNA [25] and aptamers.[26] Within this work, single-stranded DNA and antibodies are used as model systems for investigating new receptor binding strategies, as both types of bio-molecules are well suited for model receptor-analyte investigations, they are readily available and they can be purchased with or without fluorescence label.

Single stranded DNA interacts specifically with complementary DNA strands. Upon hybridization, along the chains at all sites, the base pairs adenine-thymine or cytosine-guanine are formed. The DNA strands utilized within this work are chemically synthesized by Eurofins MWG GmbH, Germany, who provide many options for modifying the ends of the strands with different functionalities.

Antibodies are naturally occurring proteins that play an important role in the immune response of animals against pathogens.[128] They are extracted from the serum of animals into which previously the desired antigen (*i. e.* analyte) was injected. Fig. 1.8 shows a schematic of an IgG antibody. Such antibodies are Y-shaped. One Fc domain (fragment that crystallizes) forms the base and two Fab domains (antigen binding fragments) form the arms of the Y. Each antibody can bind up to two target molecules, commonly with high specificity and high affinity. However, antibodies are sensitive to changes of external conditions, such as temperature, ion concentration or pH.[127] Also labeling them with fluorescent dyes can alter their tertiary folding structure and reduce their specificity. Within this work, as a model
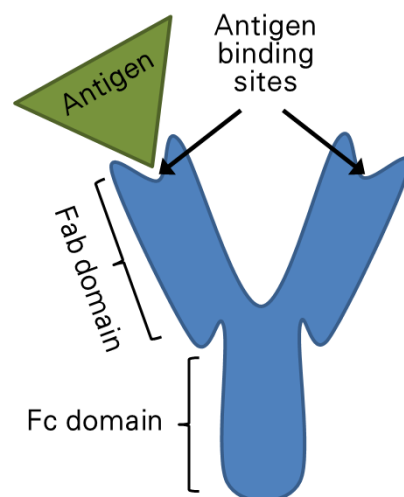
receptor system, secondary antibodies, *i. e.* with specificity towards Fc domains of other animals' antibodies, with and without fluorescent label, are used (see chapter 3).

1.4.2 Receptor immobilization

When immobilizing receptor molecules on a transducer surface, the specificity of the receptor must not be impeded. If, for example, the receptor molecules are not properly oriented in such way that the analyte binding sites face away from the surface, there will be no specific interaction. Furthermore, a reduced specificity may occur due to steric hindrance, either of the analyte attachment or of the proper folding of the receptor. Reasons for that can be a too close vicinity to the surface or a too high receptor molecule density.

For FET-based sensing, it is important to find a strategy which brings the analyte sufficiently close to the device surface so that the analyte's influence on the surface potential is not screened by other ions in the surrounding buffer solution. The maximum possible distance is described by the Debye screening length

$$\lambda_D = \sqrt{\frac{\epsilon_0 \, \epsilon_r \, k \, T}{2 \, N_A \, q^2 \, I}} \approx \frac{0.32}{\sqrt{I}} \qquad (1.10)$$

with ϵ_0 as permittivity of free space, ϵ_r as dielectric constant, N_A as Avogadro number and I as ionic strength of the solution. Equation (1.10) illustrates that the maximum possible distance for an analyte recognition event depends on the ion concentration of the buffer solution. In a 10 mM phosphate buffer (PB) solution λ_D is approx. 1.5 nm, in a 0.1 mM PB solution λ_D is approx. 14.5 nm.[131] Hence, a low ion concentration is beneficial for a high sensitivity. However, the receptor specificity is influenced by the ionic strength of the solution as well.[127,132]

The strategies for immobilizing receptor molecules can be divided into three main subgroups – physical (non-covalent) adsorption,[133] covalent binding or bioaffinity immobilization[133].[126]

1.4.2.1 Physical immobilization

Proteins, such as antibodies, adhere to surfaces by means of electrostatic, polar and hydrophobic interactions.[126,134] When using this "stickiness" for immobilizing receptors, commonly heterogeneous layers of randomly oriented molecules are formed (see Fig. 1.9a). The attachment can be enhanced by chemically modifying the surface making it more hydrophobic.[126] However, there is always an uncertainty that receptor molecules could be washed away during sample analysis which would lead to false signals.[126] Therefore, the physical adsorption is not considered as receptor immobilization strategy within this thesis.

1.4.2.2 Bioaffinity immobilization

Receptors are also immobilized on "cushions" of proteins or DNA strands by making use of biochemical affinity reactions.[126] Avidin and streptavidin for example provide four binding sites with strong affinity for biotin. Fig. 1.9c schematically depicts a binding strategy where biotinylated linker molecules (colored orange) are utilized to fix streptavidin (green) on a surface and other biotinylated functional molecules (red) bind antibodies (blue) on top of them.[135]

Protein G and protein A are surface proteins of streptococcal bacteria and *Staphylococcus aureus* which possess two and five binding sites, respectively, with high affinity towards the Fc domains of antibodies. Thus, both proteins bind antibodies the wrong way round to the bacteria surface and protect the bacteria from the immune response of mammals by disrupting opsonization and phagocytosis.[136,137] Bringing these proteins on a sensor surface enables a well oriented immobilization of antibodies afterwards, with the Fc domains as anchoring points and the antigen binding sites facing towards the analyte solution.[138,139] In other strategies, His-tag affine proteins are used as anchors for His-tagged receptor molecules.[140] Additionally, single stranded DNA on the surface can be employed for subsequent affinity binding of receptor molecules that are labeled with the complementary DNA strand.[141]

However, the bioaffinity immobilization is not considered applicable for FET-based biosensors, due to the short maximum distance within which the analyte can be detected.
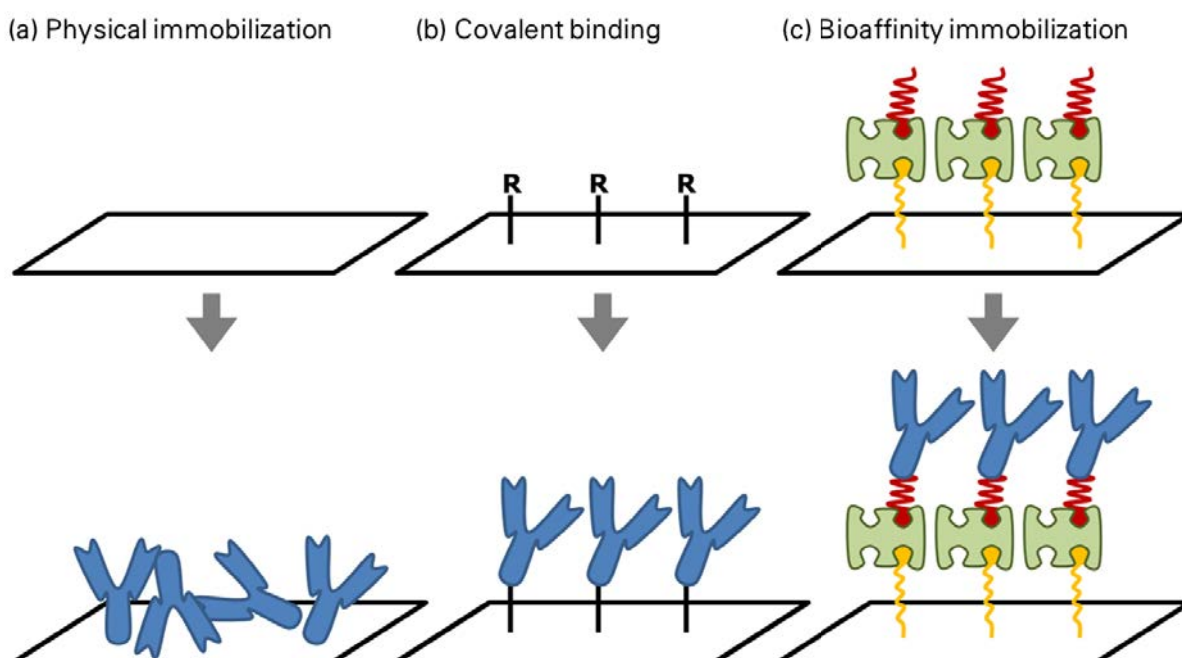
Fig. 1.9: Schematic illustration of three different kinds of receptor immobilization strategies. In the top row the prepared initial surfaces are depicted, in the bottom row, the according surfaces after antibody immobilization *via* (a) physical immobilization, (b) covalent binding, (c) bioaffinity immobilization.(Adapted from Rusmini *et al.* [126])

Protein A for example has a diameter of about 7 nm.[142] The height of an antibody is about 10 nm.[143] It is not suitable to use stacks of these molecules for sensing an antigen or analyte binding event on top of them.

1.4.2.3 Covalent binding

Binding receptors covalently to a surface *via* linker molecules (see Fig. 1.9b) solves two problems of the physical and the bioaffinity immobilization. The receptors cannot be washed off during sample analysis. And the distance between sensor surface and analyte binding site is minimized which increases the device sensitivity. FET surfaces commonly consist of oxides such as SiO_2, HfO_2 or Al_2O_3, on which in most cases silane chemistry-based linker strategies are applied.

Surface functionalization *via* silane chemistry

Silane molecules for surface functionalization purposes commonly consist of a central silicon atom at which up to three hydrolysable groups, such as methoxy or ethoxy groups or Cl-atoms, are attached (see Fig. 1.10a).[144,145] The fourth valence electron of the Si atom bonds with a linker alkyl chain at the end of which an organofunctional group is attached.[144,145]
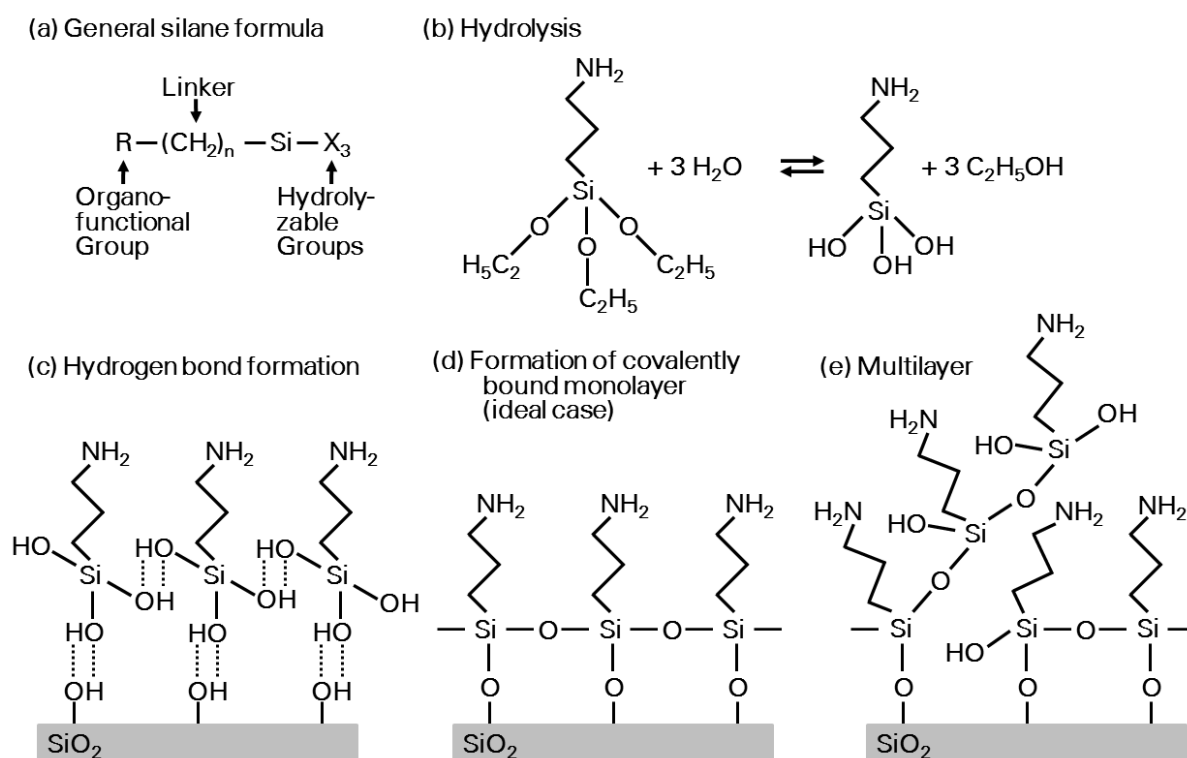
Fig. 1.10: Schematic of covalent binding of silanes to oxide surfaces. (a) General formula of silane linker molecules. (b - d) Consecutive reaction steps when binding APTES to SiO_2 surface, including (b) hydrolysis, (c) hydrogen bond formation between -OH groups among the silane molecules and between -OH groups of the molecules and the oxide surface, (d) condensation and formation of covalently bound (amino-terminated) silane monolayer, which would be the ideal case. (e) A more realistic illustration where a faulty APTES multilayer is formed.

19

Such coupling agents are commercially available with a broad range of combinations of linkers and functionalities which enables a fine tuning of surface properties like wettability and chemical reactivity.[145,146]

The molecules are stored under inert atmosphere, like Ar, due to their high reactivity. In combination with water, a hydrolysis reaction occurs where ultimately the hydrolysable groups are replaced by -OH groups. Fig. 1.10b exemplarily depicts the hydrolysis of (3-aminopropyl)triethoxysilane (APTES), a common surface modifier when combining anorganic surfaces with biomolecules. For APTES during hydrolysis, upon -OH group formation, ethanol forms as byproduct.

Subsequently, the -OH groups attached to the silanes form hydrogen bonds towards the -OH groups of other silane molecules or the -OH groups of the surface (see Fig. 1.10c). Afterwards, in condensation reactions covalent bonds among the silanes and towards the surface are formed.[147] Ideally, a monolayer is assembled – a self-assembled monolayer (see Fig. 1.10d).[148]

In case the initial silane has three hydrolysable groups, as for APTES, since the silanes also crosslink among each other, it is more likely that a partial formation of polymerized silane chains occurs. Consequently, faulty multilayers are assembled (see Fig. 1.10e). Such faulty assemblies destabilize the entire silane functionalization layer.[149] Therefore, within this work whenever possible, silanes with only one hydrolysable group – and two non-hydrolyzable methyl groups attached to the Si atom – are applied. In that case, as soon as a covalent bond between two silane molecules is formed, there is no more possibility for the dimer to covalently attach to the surface. A multilayer formation is prevented.

Receptor attachment *via* silane linker

There are silanes with different functionalities available. The different functionalities are used for various receptor binding strategies. Fig. 1.11 depicts an APTES-based immobilization of amino-terminated (protein/receptor) molecules.[27,150] When APTES is covalently linked to the surface (see Fig. 1.10 and Fig. 1.11a), an amino-terminated layer is formed. Adding succinic anhydride (Fig. 1.11b) leads to a ring opening reaction in which an amide bond and a carboxy-termination are created.[151] In the following steps, *N*-(3-dimethylaminopropyl)-*N'*-ethylcarbodiimide (EDC) and *N*-hydroxysuccinimide (NHS) are used (Fig. 1.11c) to activate the surface and to covalently bind (protein/receptor) molecules that possess an amino group for forming a stable amide bond (Fig. 1.11d,e). However, the succinimidyl esters that are formed temporarily can be hydrolysed under the bioconjugation conditions, affecting seriously the reproducibility of the process.[152]

Other strategies rely on the application of homofunctional cross linkers such as glutaraldehyde [153] or disuccinimidyl suberate [154] for covalently connecting amino-terminated

surfaces and molecules providing an amino-group, so that there is one reaction step less required during the immobilizaition procedure, compared to the procedure in Fig. 1.11.

The amounts of immobilization steps are further reduced when the surface is initially functionalized with silanes that provide other organofunctional groups such as aldehydes using 3-(trimethoxysilyl)propyl aldehyde,[24,155] isocyanates using 3-(triethoxysilyl)propyl isocyanate,[152] or epoxides using (3-glycidoxypropyltrimethoxy-silane [156,157] which enable a direct covalent binding of amino-terminated molecules.

These strategies [24,27,152–156] have in common that unused binding sites have to be passivated after receptor immobilization which is usually accomplished using ethanolamine as blocking agent. The passivation step is crucial for preventing any covalent binding of undesired molecules to the surface.

In total, the receptor attachment *via* silane linkers comprises at least three steps: (i) the linker deposition, (ii) the binding of receptor molecules and (iii) the passivation of excess binding sites. In chapter 3 of this thesis, a receptor binding approach is developed which allows the covalent binding of amino-terminated molecules on oxide surfaces without the subsequent binding site passivation step.
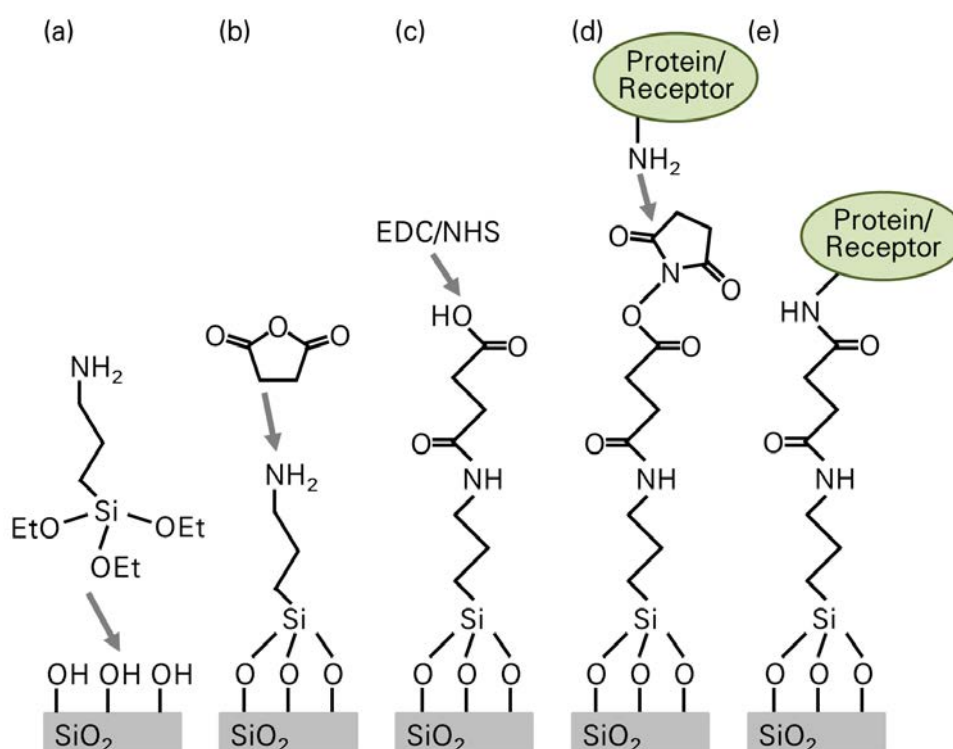
Fig. 1.11: Schematic of exemplary APTES and crosslinker-based protein immobilization strategy comprising the following steps. (a) APTES immobilization, (b) addition of succinic anhydride to the amino-terminated surface which results in a ring opening-process creating an amide bond and forming a terminal carboxylate, (c) EDC/NHS activation of carboxy group, (d & e) coupling of amino-terminated (protein/receptor) molecule to the surface.

Commonly, proteins and antibodies readily provide the required amino groups. However, there are often multiple amino acids at multiple positions within one molecule. Therefore, the above-described strategies [24,27,152–156] will immobilize such receptors in random orientations. An oriented immobilization is achieved by using linker chemistries that bind to a chemical functionality at a specific position within the chosen receptor molecule. Antibodies possess for example an area rich in aromatic amino acids – a nucleotide binding site (NBS). The NBS is near the antigen binding sites of the antibodies and has an affinity for indole-3-butyric acid.[158] On an indole-3-butyric acid-terminated surface, when exposed to 254 nm light, a covalent link to NBS is formed.[158] While one of the antigen binding sites of each photo-attached antibody faces towards the surface and is blocked for antigen interactions, the other antigen binding site is well oriented towards the analyte solution.[158] There are several binding strategies for an oriented covalent immobilization of antibodies. Trilling *et al.* [158] discuss them in their minireview.

The oriented immobilization of antibodies improves their affinity towards analytes by up to two orders of magnitude.[158] However, targeting amino groups is a sufficient and common immobilization strategy which is also applicable to other types of receptor molecules. In case of single stranded DNA or aptamers, it is for example possible to purchase them with amino labels at desired positions. Accordingly, their orientation can be engineered during the receptor synthesis.

1.5 CONCLUSION

In this chapter, the fundamentals of the main fabrication methods and the working principles of the LoC devices built within this thesis are described. Sections 1.2 and 1.4 anticipate motivations for novel strategies in fabricating PDMS-based microfluidics and silane-based receptor immobilization, respectively, which are explained in detail in chapter 2 and chapter 3. The fundamentals on the utilization of transistors for sensor applications from section 1.3 are applied in chapter 4 and 5 of this thesis.

2 MULTIFUNCTIONAL REVERSIBLY SEALABLE MICROFLUIDIC SET-UP

Building LoC devices is not possible without microfluidic set-ups. In this chapter, a novel method for fabricating multifunctional reversibly sealable microfluidic devices is described. Furthermore, possible applications of such devices beyond their usage in analysis assemblies are investigated, such as the direct printing of flexible electronic interconnects onto flexible substrates and the deposition of uniquely shaped polymer structures *via* droplet microfluidics using a UV-curable adhesive and water as continuous and dispersed phases, respectively. Parts of this chapter are published elsewhere.[159]

2.1 MOTIVATION

Microfluidics are indispensable for an efficient utilization of chemical and biological components in a broad spectrum of applications in fluid and sample manipulation [44–48,56–59] and material synthesis [51,52,54,55]. In section 1.2, PDMS is introduced as the common material of choice for the rapid prototyping of microfluidic structures, due to its advantageous properties. One distinct feature of PDMS is the possibility to bond it covalently and *irreversibly* onto substrates by means of an oxygen plasma treatment of the respective surfaces.[66] This enables a rapid and simple leak-proof utilization of the cast channel structures.[46,56–58] However, a plasma treatment is not feasible, if the surface, on which the microfluidic structure is placed, was chemically functionalized before. The plasma would destroy all organic components making any functionalization efforts useless.[160,161] To investigate and apply the surface functionalization strategy presented in chapter 3, a reliable sealing strategy without need for a plasma treatment is required.

Due to its high surface energy, PDMS also adheres *reversibly* to many kinds of substrates without the application of an oxygen plasma.[66,73] Besides the utilization on previously functionalized surfaces, this reversible sealing is advantageous for several applications such as the chemical patterning of surfaces,[162] a locally confined deposition of cells,[163] or the production of polymer-based microstructures *via* micromoulding in capillaries (MIMIC).[164] However, the self-adhesion cannot be used for working pressures above 35 kPa.[73] To increase the applicable fluid pressures, while maintaining the reversibility of the PDMS attachment to the substrate, different techniques were developed. Le Berre *et al.*[78] include in their PDMS designs, next to the fluidic circuits, channel networks that allow the application of an externally created vacuum to enhance the adhesion of the stamps to the substrates by aspiration. The maximum working pressure achieved in this configuration is 100 kPa. However, the space requirements of the aspiration structures may be a drawback for a number of microfluidic applications. Rafat *et al.*[70] use permanent magnets to increase

the maximum working pressures up to 145 kPa. A restriction of their approach is its suitability for simple microfluidic layouts with large channels only. Pressing PDMS on the substrate surface using special mechanical clamps allows maximum working pressures of up to 220 kPa as demonstrated by Yang and Maeda[76] and Saarela *et al.*.[74] Chen *et al.* achieve with a glass-PDMS-glass sandwich configuration maximum working pressures of up to 400 kPa.[77] However, in the latter cases [74,77] the diversity of the channel designs is strongly restricted by the layout of the clamps or the glasses fixing the PDMS devices. Changing in- or outlet positions, or the tubing amounts, respectively, would require a change of the clamp or the glass designs.

Usage of all advantageous aspects of PDMS-based microfluidics in reversibly sealable set-ups requires a technique that combines high fluid working pressures with the possibility of a rapid prototyping of channel designs. In this chapter, a novel two-step PDMS casting method is presented which provides a large freedom in channel structure design, allows working pressures of up to 600 kPa and keeps the channel sealing reversible, at the same time.

As a possible application of the microfluidics prepared with the developed method, the printing of flexible electronic interconnects is demonstrated. Flexible and stretchable sensor devices that do not break upon deformation enable a real time detection of physiological data on top of or underneath the skin, or near moving body parts of a patient. There are flexible electronics in which tactile,[165] temperature,[166,167] DNA [40] and glucose [168] sensors are implemented. In combination with flexible and stretchable batteries [169] and antennae,[169,170] such devices may enable an on-line monitoring of medically relevant indicators. In this way, the idea of measuring at the *point of care* is pushed to its limits. During the last years, great attention was given to the deposition of organic conductive materials on bendable supports using different kinds of printing techniques for generating flexible electronic devices.[171] Within this work, as a cost efficient approach for printing flexible interconnects, microstructures based on the conductive polymer poly (3,4-ethylenedioxythiophene) poly (styrenesulfonate) (PEDOT:PSS) are produced.

Furthermore, the developed microfluidic set-up is used for the deposition of polymer structures with unique shape. The procedure is based on droplet microfluidics (see section 1.2.1) which in other cases is utilized for the production of various kinds of spheroid-shaped objects consisting of multiple components and possessing diverse properties.[51–53] Within this work a UV-curable adhesive is used as continuous and water as dispersed phase. In this way microcavities are formed which may find application in cell culturing in the future.

2.2 MATERIALS AND METHODS

2.2.1 Fabrication of reversibly sealable PDMS-based microfluidics

Fig. 2.1 depicts the fabrication process of the reversibly sealable microfluidic devices. The successive steps are shown as schematic drawings on the left hand side (Fig. 2.1a-f), and as photographs on the right hand side (Fig. 2.1h-n). The schematic drawings show the production of a simple channel structure with only one in- and one outlet to prevent an overcrowding of the images. The photographs provide insight in the complexity that can be achieved with the proposed method, as the rapid prototyping of a four-channel structure with in total eight in- and outlet-tubes is demonstrated.

As starting point, a mold or master structure, respectively, is prepared (Fig. 2.1a,h). Within this work two types of SU-8 negative photoresist (MicroChem Corp., USA), SU-8 2010 and SU-8 2050, are used to produce structures of 10 and 50 μm height, respectively. The respective protocols are given in the appendix.

On top of the mold, PDMS is cast (Fig. 2.1b). For that purpose PDMS base and curing agent (Sylgard 184 Silicone Elastomer Kit, Dow Corning, USA) are mixed in varying ratios between 6:1 and 10:1 (w/w), degassed and poured over the mold. The cast is cured for 5 h at 45°C and peeled off (Fig. 2.1i). Then, holes are punched into the in- and outlet areas of the PDMS (Fig. 2.1c,k) and PTFE tubing is attached (Fig. 2.1d). Up to this point the procedure does not differ from the standard fabrication of PDMS-based microfluidics introduced in section 1.2.

In the following steps, the freshly prepared stamp, including the attached tubing, is enclosed in a second layer of PDMS. The self-adhesion of the PDMS stamp is used to seal the channel structure with a glass slide. Then a casting frame with at least $n + 1$ holes in one side is placed around the PDMS stamp, where n is the number of attached tubes. The tubing is guided through the holes in the frame on top of which a second glass slide is placed (Fig. 2.1e). After fixing the glass slides with clamps to the frame, uncured PDMS is cast into the assembly by means of a syringe using the remaining hole in the casting frame, through which no tubing is guided (Fig. 2.1l). The second layer of PDMS is again cured for 5 h at 45°C. A cuboid shaped PDMS stamp with the tubing guided to one side is formed (Fig. 2.1m).

Within this work, 45°C curing temperature are applied to minimize the curing time of the PDMS while preventing deformations in the fluid channel layout due to internal stresses induced by the heating and cooling cycle.[71] Particularly, the curing of the second layer of PDMS around the initial one can induce distortions, if too high curing temperatures are used.

(a)

Mold preparation

(b)

Cast and cure PDMS

(c)

Preparation of holes for ...

(d)

... tubing attachment

(e)

Enclose channel system in 2nd PDMS layer using casting frame with holes at 1 side

(f)

Mount substrate and adjusted channel system in (microscopy) holder

(g)

| Air |
| Aqueous FITC solution |
| Isopropanol-based solution of black marker pen |
| Aq. solution of Dylight594 labeled antibodies |

100 µm

Fluorescence microscopy image combining the information obtained by using the bright field mode, one fluorescence mode detecting red fluorescence and one fluorescence mode detecting green fluorescence → 4 different fluids in 4 separate channel systems

Device fabrication route

(h)

1 cm

Master structure based on SU-8 2050 photoresist, on Si-wafer piece

(i)

PDMS stamp after 1st curing step

(k)

PDMS stamp after punching holes into every in-/outlet section

(l)

| Glass slides in the back & the front of the frame | Aluminum frame with 9 side-holes | 8 tubes pushed into initial PDMS stamp & guided through holes in the frame |

Syringe for injecting PDMS into the frame

Initial PDMS stamp with inserted tubigs

Frontline of the freshly cast PDMS (will be filled entirely at the end)

Clamps fixing glass slides to the frame

Second casting step for creating cuboid shaped PDMS stamp with enclosed tubing

(m)

Final cuboid shaped PDMS stamp with 4 micro-channels and 8 enveloped tubes

(n)

PDMS block   In- / oulet tubes

PMMA lid of sample holder

Fixation screws   Microscope objective

Aluminum base of sample holder

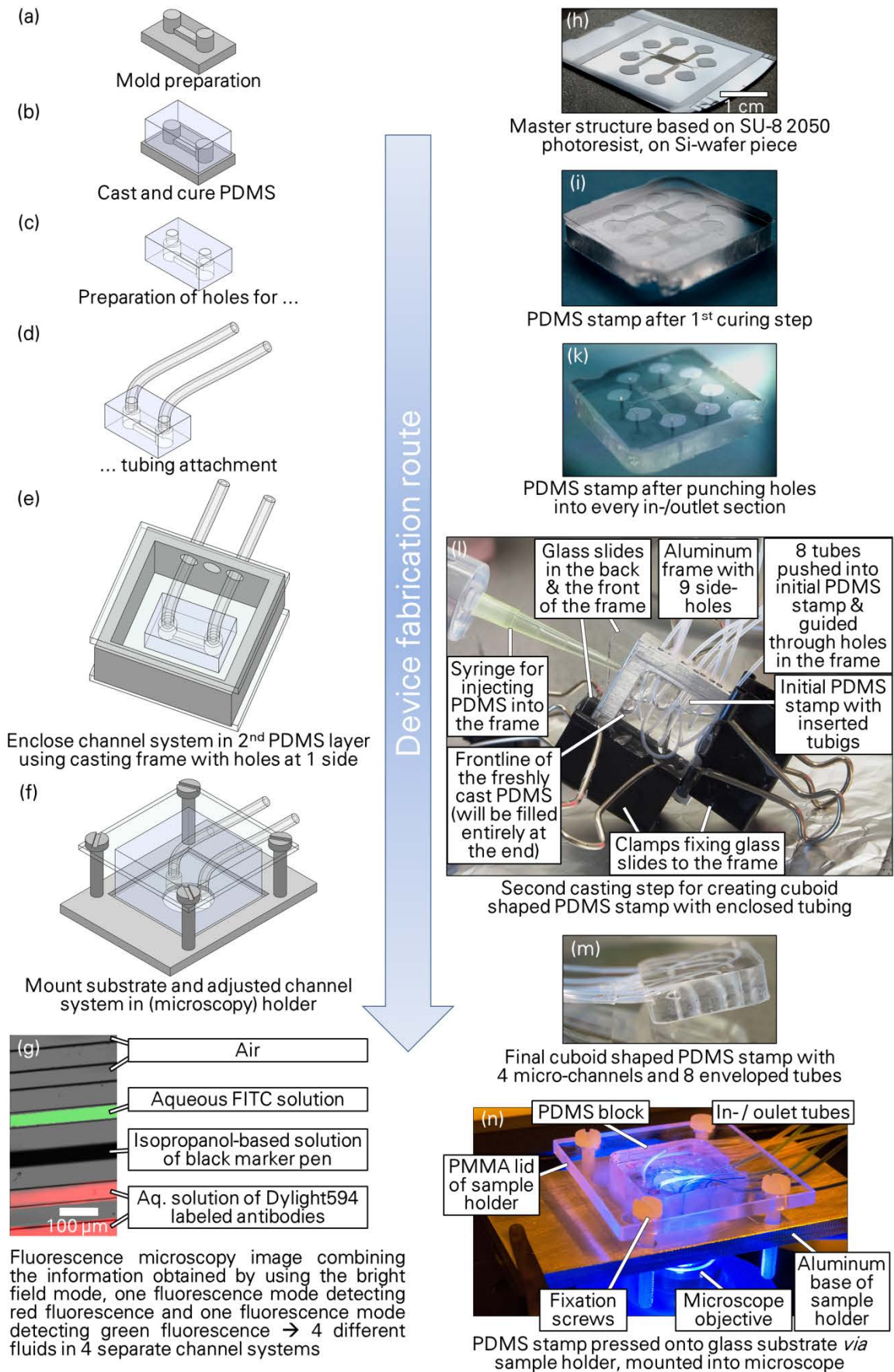PDMS stamp pressed onto glass substrate *via* sample holder, mounted into microscope

Fig. 2.1: Fabrication of reversibly sealable PDMS device – photographs on the left hand side and according schematic drawings on the right hand side. Including one fluorescence microscopy image obtained while utilizing the four-channel PDMS stamp produced during the photo series.

The final PDMS stamp can be placed on top of virtually any kind of substrate. Due to the cuboid shape of the stamp a simple sample holder is sufficient to press the PDMS onto the substrate which increases the possible fluid working pressures effectively. Within this work the sample holder consists of an aluminum base and a polymethylmethacrylate (PMMA) lid which can clamp the PDMS and the substrates *via* four screws (Fig. 2.1f,n). Since the tubing is guided to the side, there is no need for any tubing-related holes in the PMMA lid which is advantageous over other reversible sealing techniques with regard to a rapid prototyping of different channel designs.[74,77] Furthermore, having large parts of the tubing (≥ 15 mm) embedded in the PDMS stamp provides a tubing strain relief enabling a high robustness of the devices.

2.2.2 Leakage test

To compare the reliability of microfluidic devices fabricated *via* the presented method, a leakage test is performed. Partially adopting the scheme of Chen *et al.*,[77] a PDMS device with only one attached tube (see Fig. 2.2) is fabricated. Compressed air is pushed pressure controlled (manometer, WIKA Alexander Wiegand SE & Co. KG, Germany) into the
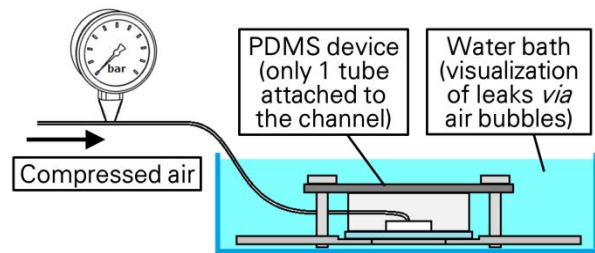

Fig. 2.2: Schematic drawing of leakage test arrangement. Compressed air is pushed pressure controlled into a PDMS device with only one attached tube. Having the whole set-up inside a water bath allows checking for air bubbles indicating a leak.

channel while keeping the entire setup inside a water bath. The pressure is gradually increased to investigate the maximum applicable working pressure before air bubbles occur indicating a leak.

2.2.3 Printing flexible electronic interconnects

For generating flexible electronic devices, an aqueous PEDOT:PSS solution (Sigma-Aldrich, MO, USA) is pushed into a two-channel-structure possessing the channel layout, depicted in Fig. 2.4a. The lines between the inlet and outlet areas in position 1 and 2, and position 3 and 4, respectively, are of 40 μm width and 10 μm height. A printer foil supported by an object carrier glass carrier is utilized as substrate. After fixing the PDMS on the substrate and filling the channels with PEDOT:PSS solution, the excess water is removed in two steps. At first a local heating, constricted to the aluminum base of the sample holder and, thus, the PDMS channels, on a hot plate at 80°C for 48 h is applied. Subsequently, the entire assembly, including the tubing, is heated inside a furnace to 80°C for 24 h. Afterwards, the PDMS setup is disassembled to obtain the bare printer foil with the PEDOT:PSS on top.

Samples are investigated *via* optical microscopy (Axiolab, Carl Zeiss Microscopy GmbH, Germany). Conductivity measurements to test the electrical properties of the PEDOT:PSS

interconnects are performed using a source measure unit (SMU, Source Meter 2604B, Keithley, USA) in combination with a DPP105-V-AI-S micropositioner (Cascade Microtech, Inc., USA) probe station.

2.2.4 Deposition of polymer-based microcavities

Fig. 2.5a illustrates how inversed porous polymer structures are created and immobilized on a polystyrene substrate by using a T-junction droplet microfluidic channel design (see section 1.2.1). It is a two-step procedure. At the beginning, at $t = t_1$, droplets are formed. An adhesive that polymerizes under UV-irradiation (proformic 40166, VIKO UG, Germany) is utilized as continuous phase. Water is the discrete phase. Both phases are pushed into the channel system with a flow rate of $u = 0.003$ µl/min. After having generated a sufficient amount of droplets, such that the entire channel system is filled, the flow is stopped. $u = 0$ µl/min at $t > t_1$. The droplets are immobilized by applying UV-light from a UV-LED supplied with the adhesive for at least 7 s. The illumination is restricted to a desired area of the microfluidic chip. Illuminating the entire set-up would be disadvantageous, because the consequent polymerization in the in- and outlet tubes would prevent a reutilization of the PDMS stamp. Subsequently, the setup is disassembled and the polystyrene substrate is rinsed with water and dried under N_2 gas flow. The PDMS stamp is cleaned with acetone and isopropanol and blown dry. The polymer structure remaining on the polystyrene substrate is investigated *via* optical microscopy (Axiolab, Carl Zeiss Microscopy GmbH, Germany) and scanning electron microscopy (SEM, Philips XL 30 ESEM-FEG environmental scanning electron microscope, FEI, USA).

2.3 RESULTS AND DISCUSSION

2.3.1 Channel deformation during device assembly

When assembling the microfluidic devices by pressing the PDMS stamps onto the respective substrates, at high clamping pressures a deformation of the channels is observed (see Fig. 2.3). Particularly wide hollow structures with width to height ratios above 10:1 are prone to collapsing as also reported by Xia and Whitesides for covalently bonded PDMS devices.[69] Therefore, if possible, in all microfluidic channels with high aspect ratios additional support posts are included to stabilize the structures, hence, to increase the applicable clamping pressures. The imprints of such posts are depicted in Fig. 2.4c.

In Fig. 2.3 it is also visible that at high clamping pressures the PDMS features in contact with the substrate are squeezed to form broader contact areas. Such deformations can affect microfluidic channels and their flow profiles in undesirable ways. During assembly, it is important to check optically for such deformations and to adjust the clamping pressure accordingly. By changing the mixing ratio of PDMS base and curing agent and, thus, the stiffness of the PDMS stamp, deformations can be reduced (see section 1.2).
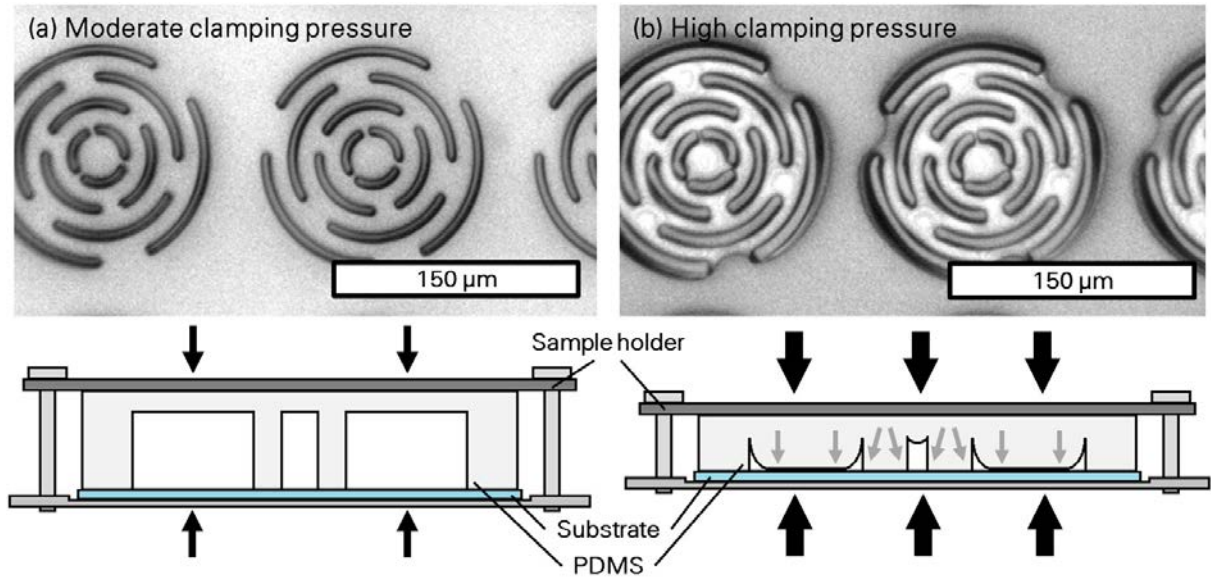
Fig. 2.3: Deformation and collapse of PDMS structures upon increased clamping pressure. Optical microscopy images of a PDMS device assembly with an array of circularly arranged PDMS walls at (a) moderate clamping pressure, (b) high clamping pressure. At high pressure, the PDMS walls are squeezed to form broader contact areas with the substrate. In the wide areas between the circular wall arrangements the PDMS structure collapses. Within the narrow gaps between the walls of each circular arrangement the collapse is prevented. The drawings underneath the microscopy images schematically illustrate the PDMS behavior. Black arrows symbolize the pressure strength. Gray arrows indicate PDMS deformations.

Konda *et al.* [75] make use of clamping pressure-based channel deformations by implementing channel walls of different heights in their structures. By increasing or decreasing the clamping pressure, additional channel walls are pushed into the flow structure or taken out, respectively.

2.3.2 Maximum fluid working pressure

Within this work the pressure of compressed air is raised up to 600 kPa without observing any air bubble formation in the water bath of the built-up depicted in Fig. 2.2. Hence, at this pressure no leakage occurs, not between the PDMS device and the glass substrate, and also not along the PTFE tube attached to the channel. This pressure resistance is considered as the highest one ever demonstrated for PDMS based reversibly sealable microfluidic devices,[70,74,77,78] and it exceeds the resilience of plasma bonded PDMS-on-glass devices.[172] The cuboid shape of the PDMS stamp, as a result of guiding the tubing sideways, enables a uniform pressure distribution over the entire chip when fixing it in the sample holder on the substrate. Consequently, a high device pressure resistance is achieved. Raising the applied fluid pressure to values above 600 kPa causes a leak in the outlying tubing assembly.

Comparing the achieved pressure resistance particularly to the results in the work of Saarela *et al.* [74] in which also mechanical clamps are used, the resistance increase can be attributed

to the improved tubing integration. In the work of Saarela *et al.* [74] the tubing is only pushed into the PDMS, maximum 6 mm deep. Consequently, leakage mainly occurs at the PDMS-tubing interface. Embedding the tubing in the PDMS casing circumvents such issues.

In one of the latest publications on reversibly sealable microfluidics, published after the paper that was brought out within this thesis,[159] Konda *et al.* [75] fabricate their devices *via* 3D printing-based molds. 3D printing allows positioning the in- and outlet holes at the sides of the PDMS stamps, as well. Therefore, their approach also enables the use of a simple clamping arrangement, and it provides a similar degree of freedom concerning the rapid change of channel designs. However, a maximum working pressure is not determined in their publication.

2.3.3 Printing flexible electronic interconnects

The results of the printing experiments using PEDOT:PSS are summarized in Fig. 2.4. Fig. 2.4a illustrates the layout of the structure, with positions 1-4 as in- or outlet tube attachment areas. The optical microscopy image in Fig. 2.4b shows the substrate printer foil in an untreated state. Several dark spots are visible which might be due to material inhomogeneities or surface contaminations. The optical microscopy images of an inlet region in Fig. 2.4c and of a curved line section in Fig. 2.4d illustrate that the developed printing method allows a well defined deposition of PEDOT:PSS with homogenous line widths and material densities. The conductive properties of the printed structures are examined while bending the substrate foil as depicted in the photograph in Fig. 2.4e. Measurements between position 1 and 2, and position 3 and
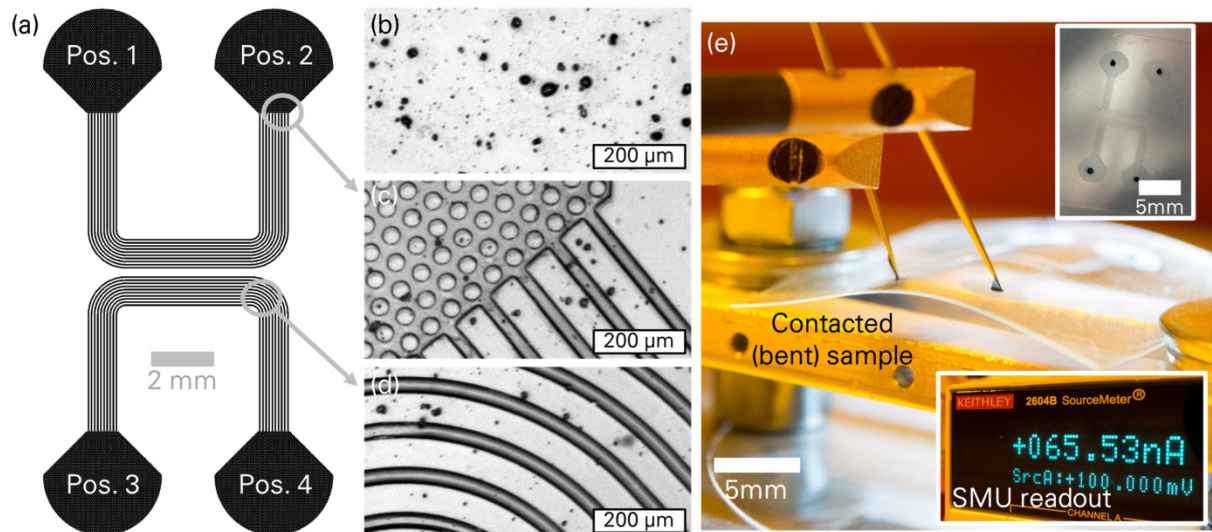
Fig. 2.4: Deposition of PEBDOT:PSS-based flexible electronics. (a) Layout of the channel design. (b) Optical microscopy images of the printer foil which was utilized as substrate before any polymer deposition, (c) of the in- / outlet area and (d) one curved line section after PEDOT:PSS printing. (e) Photograph of the conductivity measurement arrangement and in the insets the simultaneously displayed data on the SMU readout and a photograph of the entire circuit, respectively.

4 (see Fig. 2.4a), respectively, showed resistivities in the low MΩ range, as can be derived from the lower right inset in Fig. 2.4e depicting the display of the SMU during the experiment. Taking into account the device geometry a conductivity of approx. 0.01 S·cm^{-1} is estimated for the PEDOT:PSS. As works of other groups show, this value could be further enhanced.[173,174] Measuring the resistance between position 1 and 3 leads to infinite values. These results demonstrate that printing PEDOT:PSS based flexible electronic devices is possible using the presented approach. The 40 µm feature size achieved within this work is similar to the accuracies obtained with other conductive polymer printing techniques.[171] Since the PDMS channel design can be changed very quickly with the presented fabrication method, a rapid prototyping of flexible electronic circuits with versatile layouts is possible.

2.3.4 Deposition of polymer-based microcavities

Fig. 2.5 summarizes the procedure and the outcome of the droplet formation and polymer structure immobilization experiments. As depicted in Fig. 2.5b, water droplets are formed inside a continuous phase of UV-curable adhesive. Due to the high viscosity of the adhesive of 3,000 cP, droplets of water are even formed when the adhesive is introduced *via* the orthogonal channel. After stopping the fluid flow (see Fig. 2.5c), polymerizing the adhesive and removing the PDMS channel the polymer structure is still in shape and fixed to the polystyrene substrate (see Fig. 2.5d). Imaging the structure from the side provides more
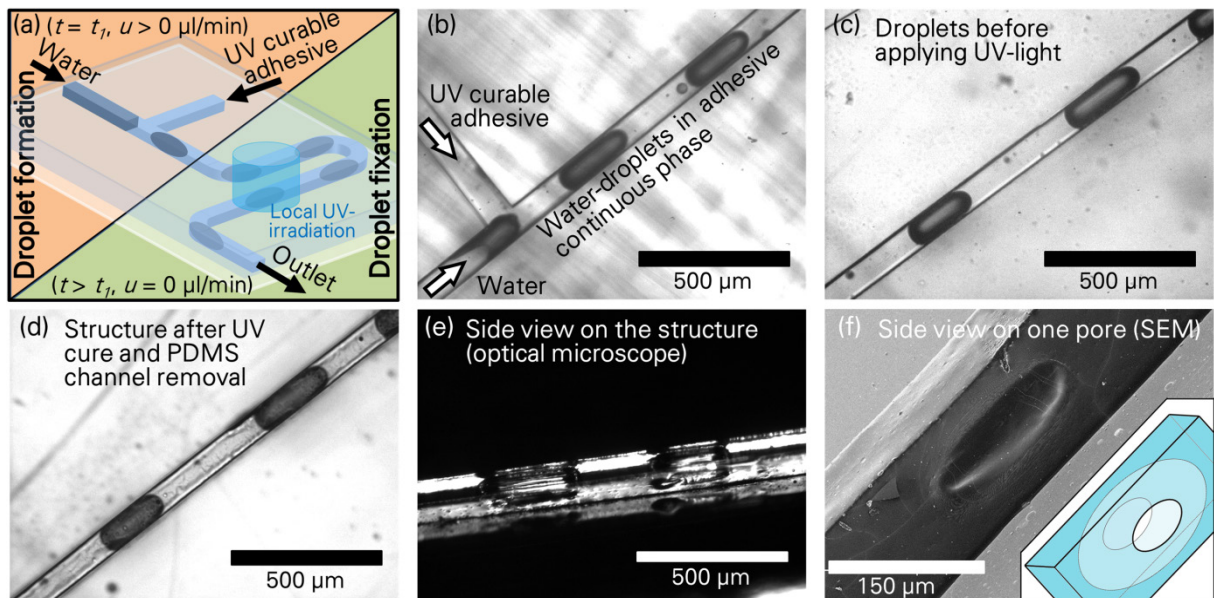
Fig. 2.5: Illustration of the droplet formation and polymer structure immobilization procedure on a polystyrene substrate using a T-junction PDMS channel layout. (a) Schematic drawing of the two-step procedure. Top view optical microscopy images of (b) the droplet formation process, (c) the droplets before curing the utilized UV-curable adhesive, (d) after polymerization of the adhesive and removal of the PDMS channel. (e) Side view optical microscopy image of the formed polymer structure. (f) SEM picture of a side view on one pore inside the polymer structure and schematic drawing of a pore in the polymer material (inset in (f), orientation of the pore similar to the one in the SEM image).

information on the shape of the pores left by the water in its previous polymer "cage" (see Fig. 2.5e). The information of Fig. 2.5 e in combination with the insights gained *via* SEM (see Fig. 2.5f) lead to the conclusion that the pores possess different kinds of walls: in the direction towards the substrate there is a thin polymer layer on the polystyrene surface; on top of the pore there is a thin closed polymer layer, as well; in two lateral directions – along the previous channel pattern – there are thick polymer walls between the separate pores. In the other two lateral directions, there are thin polymer walls with oval openings that previously allowed the water to leave the polymer structure (see also inset in Fig. 2.5f).

Such cavities may be very helpful for cell growth experiments. The openings at the side walls would allow the cells to enter the pores making a large surface area accessible. There are various photopolymerizable hydrogels which can be used for tissue engineering purposes and which could replace the UV-adhesive utilized within this work.[175] As mentioned in section 1.2.1, the size of the droplets and, thus, the microcavities can be tuned by altering device geometries, viscosities and flow velocities of the immiscible fluids, use of surfactants, and hydrophilicity or hydrophobicity of the channel surface.[87] In this way large amounts of differently sized pores can be produced in very short time and facilitate for example experiments on pore size dependent cell fate decisions.[176]

2.4 CONCLUSION

In this chapter, a seminal technique for the production of reversibly sealable microfluidic devices withstanding fluid working pressures up to 600 kPa is presented. Guiding the in- and outlet tubes connected to the fluid channels sideways enables a rapid prototyping of microfluidic devices with a high versatility of channel designs while no changes in the layout of the utilized mounting assembly are required. Potential applications for such devices are demonstrated by depositing flexible electronic interconnects and patterned polymer microstructures on different substrates. Also a patterned etching of Al_2O_3 using H_3PO_4 during the fabrication of ISFETs (see chapter 4) *via* the presented microfluidic set-up is possible (results not shown). In general, the demonstrated technique can be used for a low-effort patterned interaction of various chemicals with a broad range of substrates opening up new possibilities for many research fields.

A 3D printing-based microfluidic set-up published a few months later by Konda *et al.*[75] shows similar advantages. However, a maximum fluid working pressure is not investigated. The fluid working pressures achieved within this thesis make the presented approach attractive for investigating spray-drying techniques.[55]

Adapting the soft lithography procedure to other curable polymers, such as perfluoropolyethers,[177] polyurethanes or polyimides,[69] instead of PDMS, will further broaden the range of possible applications. Thus, the demonstrated technique will strongly enhance LoC device fabrication.

Within this thesis, one highly important feature of the presented technique is the reliable sealing of microfluidic channels without any plasma treatment, hence, without destroying organic components on the substrate surface. In chapter 3, a novel surface functionalization method is investigated. The microfluidics for the respective experiments are based on the device fabrication method developed within this chapter.

3 SILANE-BASED SURFACE MODIFICATION

As pointed out in section 1.4, the specific interaction of a sensor with its environment is crucial for its application. In this chapter a novel surface modification method for an effortless immobilization of (bio)-receptor molecules on oxide surfaces is presented. The strategy is based on the silane 3-(triethoxysilyl)propylsuccinic anhydride (TESPSA). For verifying the success of the new receptor binding approach, a patterned deposition of TESPSA in combination with fluorescence microscopy experiments using fluorescence-labeled antibodies is performed. Within the chapter, the patterning of silanes is investigated. Further applications of patterned silane-functionalized surfaces, such as a patterned deposition of gold nanoparticles (AuNPs) and localized surface wettabilities, are demonstrated. Parts of this chapter are published elsewhere.[178]

3.1 MOTIVATION

One common approach to make ChemFET or BioFET devices specific for particular analytes is the covalent attachment of receptor molecules on their surfaces. The fundamentals of a silane-based attachment of functional groups to oxide surfaces and their subsequent utilization for anchoring receptors are described in more detail in section 1.4.2. Functionalization approaches based on APTES require up to five reactions steps before finishing the immobilization of amino-terminated receptors.[27,150] To reduce the efforts during receptor immobilization other functionalization approaches were developed. Only three reaction steps are needed when using 3-(trimethoxysilyl)propyl aldehyde,[24,155] 3-(triethoxysilyl)propyl isocyanate,[152] or 3-glycidoxypropyltrimethoxysilane[156,157] as initial linkers. The three basic steps are (i) covalent attachment of the silane-linker with its organofunctional groups, (ii) covalent binding of receptor molecules *via* the organofunctional groups at the surface (iii) passivation of excess binding sites. The last step is crucial for preventing any unspecific, potentially covalent interactions between analytes and the surface.

Within this chapter, a novel strategy is proposed, with which no additional binding site passivation is required. This further reduces the amount of necessary reaction steps and, thus, the efforts during receptor immobilization. The new approach is based on the silane linker TESPSA (see Fig. 3.2) which brings a succinic anhydride functionality to the surface. Similar anhydrides are known to readily react with amines in a ring opening reaction forming an amide bond.[179,180] With this reaction, antibodies or other amino-terminated receptor molecules can be covalently bound in a single preparation step (see Fig. 3.2b). Additionally, when exposed to water, the anhydride group gets hydrolysed and two carboxy groups are generated (see Fig. 3.2c) inhibiting a subsequent covalent binding in the presence of

amines.[179] Consequently, using TESPSA to attach receptor molecules to oxide surfaces makes an additional binding site passivation dispensable.

In the first part of this chapter (sections 3.2.1 and 3.3.1), different activation procedures for a proper silanization of glass substrates are assessed. The effects of different silanes and varying silanization times on the surface wettability are monitored.

In the second part (sections 3.2.2, 3.2.3 and 3.3.2), TESPSA is deposited in stripe patterns on glass substrates and immersed with antibody molecules. Using secondary antibodies with and without fluorescence label as a model system, fluorescence microscopy is used to collect information about (i) the attachment of the antibodies to the surface, (ii) their specificity against their target molecules, and (iii) the ability of the surface functionalization approach to prevent unspecific binding.

In-between the TESPSA stripes, a protein repellent surface coverage is required to obtain a reference fluorescence signal. Polyethylen glycol (mPEG) layers are known to prevent protein adsorption.[181] Thus, for investigating the receptor binding, a protocol is developed, which enables depositing patterns of TESPSA within mPEG-sliane-functionalized areas.

Patterns of different silanes can introduce alternating surface wettabilities which can be applied for a passive regulation of fluid streams.[182,183] In the third part of this chapter (sections 3.2.4 and 3.3.3), the formation of hydrophilic patterns within hydrophobic surface areas is investigated – with the hydrophobic areas being based on the deposition of the fluorinated silane (Heptadecafluoro-1,1,2,2-tetrahydrodecyl) dimethylchlorosilane (HFDMCS) and the hydrophilic parts being based on an air plasma treatment or a deposition of TESPSA.

As will be further explained in chapter 4 of this thesis, one important step for the bottom-up growth of SiNWs is the deposition of seed AuNPs on a growth substrate. A patterned deposition of AuNPs enables the fabrication of arrays of vertical FETs with very high transistor densities [184,185] and arrays of 2D photonic crystals.[184] In sections 3.2.4 and 3.3.3 a silane-based patterned deposition of AuNPs is described.

3.2 MATERIALS AND METHODS

The chemicals utilized for the surface functionalization procedures within this chapter are listed in Tab. 3.1. The devices for sample characterization are listed in Tab. 3.2. For initial wettability and fluorescence microscopy investigations microscopy-grade glass slides are used as substrates (Paul Marienfeld GmbH, Germany). For investigations on silane-based patterns of hydrophilic and hydrophobic surface areas and for the deposition of AuNPs silicon wafers (single side polished, native SiO_2, Siegert Wafer, Germany) are used. Prior to silanization, the substrates are consecutively cleaned in acetone, isopropanol and deionized (DI) water, dried under a stream of N_2 and activated (see section 3.2.1).

Tab. 3.1: List of the chemicals applied within this chapter – full names, abbreviations, supplier and storage conditions

Chemical name	Abbreviation	Supplier	Storage
3-(Triethoxysilyl)propylsuccinic anhydride	TESPSA	abcr GmbH, Germany	RT, under Ar atmosphere
(3-Aminopropyl)dimethylethoxysilane	APDMES	abcr GmbH, Germany	RT, under Ar atmosphere
(Heptadecafluoro-1,1,2,2-tetrahydrodecyl)dimethylchlorosilane	HFDMCS	abcr GmbH, Germany	RT, under Ar atmosphere
mPEG-silane, MW 350 Da		Nanocs Inc., USA	RT, under Ar atmosphere
(3-Aminopropyl)triethoxysilane	APTES	Sigma Aldrich, USA	RT, under Ar atmosphere
AZ 6632 positive photoresist		MicroChemicals GmbH, Germany	RT, dark condition
Amino-terminated oligonucleotides, FAM fluorescence-labeled, $\lambda_{emission}$ = 518 nm		Eurofins MWG Operon, Germany	-20°C, dark condition
Donkey anti-rabbit IgG	$IgG_{Receptor}$	Fisher Scientific GmbH, Germany	4°C, dark condition
Rabbit anti-mouse IgG, DyLight 488 fluorescence-labeled, $\lambda_{emission}$ = 518 nm	IgG_{Target_green}	Fisher Scientific GmbH, Germany	4°C, dark condition
Donkey anti-goat IgG, DyLight 594 fluorescence-labeled, $\lambda_{emission}$ = 617 nm	$IgG_{Control\_red}$	Fisher Scientific GmbH, Germany	4°C, dark condition
Aqueous 20 nm AuNP suspension, stabilized *via* branched polyethylenimine		nanoComposix Europe, Czech Rep.	4°C, dark condition

Tab. 3.2: List of devices utilized for sample characterization

Device	Supplier
Contact Angle System OCA30	DataPhysics Instruments GmbH, Germany
Axiovert 200M, transmitted light and fluorescence microscope → filter set 10 (green fluorescence, excitation band pass (BP) filter 450 - 490 nm, beam splitter (BS) 510 nm, emission BP filter 515 - 565 nm) → filter set 15 (red fluorescence, excitation BP filter 540 - 552 nm, BS 580 nm, emission low pass filter > 590 nm)	Carl Zeiss Microscopy GmbH, Germany
Axiolab, reflected-light microscope	Carl Zeiss Microscopy GmbH, Germany
Philips XL 30 ESEM-FEG environmental scanning electron microscope	FEI, USA

3.2.1 Surface wettability dependent on surface activation and silane functionality

Before silanization, the substrates are activated to generate a maximum amount of -OH groups on the surface for a dense silane deposition. Three activation approaches are applied. Glass slides are immersed (i) for 1 h in 1M NaOH, (ii) for 30 min in 1:1 (vol./vol.) MeOH:HCl,[186] or they are (iii) treated with an air plasma (Plasma Prep II, SPI supplies, USA).

As a measure for the quality of the silanization process, the static contact angles of water drops on the silanized surfaces are determined. At least 5 drops are measured for each silanization experiment ($V = 1.6$ µl). In initial experiments, APDMES is applied. APDMES is a derivative of the commonly used APTES, with only one hydrolysable ethoxy group instead of three, which prevents the formation of multilayers.

Two ways of applying the silane are tested. (i) Immersion of the substrate in a solution of 1 .. 2 vol.% APDMES in ethanol, so that the APDMES molecules diffuse within the ethanol and react with the substrate surface. (ii) Positioning the substrate and an open container of APDMES inside a closed petri dish, so that the APDMES evaporates and reacts with the substrate surface from the vapor phase. Different functionalization times are examined.

The silanization from the vapor phase is of particular importance for the patterned deposition of the silanes described in section 3.2.2. APDMES possesses a sufficiently low boiling point (78°C)[187] to evaporate at room temperature (RT). The boiling point of TESPSA (152°C)[188] is much higher. Therefore, the silane is placed inside an open container next to the substrate in a desiccator. The silane is evaporated by applying a vacuum of approx. 5 kPa and by providing additional heat input *via* an externally positioned infrared lamp (see Fig. 3.1e). Different silanization times are tested. For HFDMCS, which has the highest boiling point (189°C)[189] among the applied silanes, the same evaporation and silanization built-up is used.

There are no data available about the boiling point of the mPEG-silane. Therefore, the mPEG-silane, which is a triethoxysilane,[190] is applied as 2 vol.% silane solution in ethanol. Different silanization times are tested.

After silanization, all substrates are rinsed twice in isopropanol and dried under a stream of N₂.

3.2.2 Patterned surface functionalization

The patterned surface functionalization is based on a protocol by Shah *et al.*.[191] Fig. 3.1 schematically depicts the patterning strategy developed within this thesis. At first the entire substrate is covered with a silane of one organofunctionality (functionality (<u>A</u>), see Fig. 3.1b). By means of UVL using the positive resist AZ6632 the functionalization pattern is defined
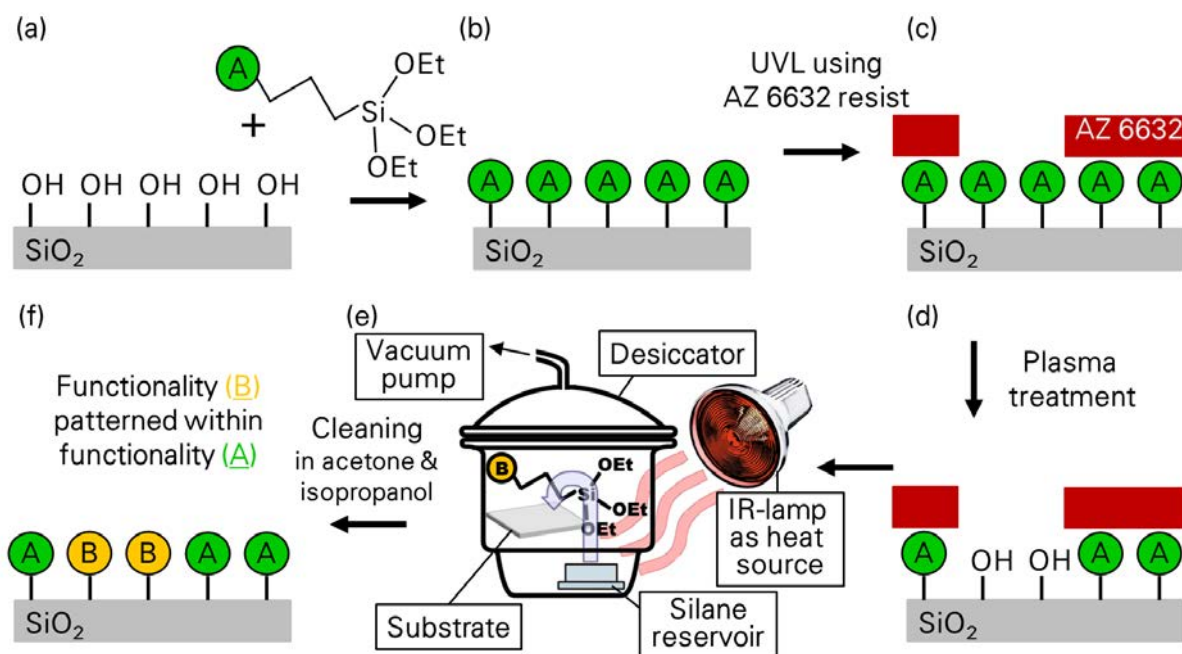
Fig. 3.1: Schematic illustration of silane-based patterned surface functionalization, starting with (a) a plasma activated substrate surface. (b) Immobilization of functionality (A) on the surface. (c) Preparation of the pattern *via* UVL. (d) Removal of functionality (A) and plasma activation of the surface in the areas not covered with photoresist. (e) Evaporation of silane with functionality (B) for reaction with activated surface areas inside a desiccator, supported by applying a vacuum and heating the silane reservoir *via* external heat source. (f) Resulting patterned surface with functionality (B) within areas of functionality (A).

(see see Fig. 3.1c). The recipe for applying the AZ6632 is provided in the appendix. In a 15 min air plasma step the previously deposited silanes are removed from the surface and the surface is activated again in the areas which are not covered with photoresist (see Fig. 3.1d). Subsequently, a second silane with another functionality (functionality (B), see Fig. 3.1e,f) is deposited. This reaction must be induced from the vapor phase. Applying the second silane in a solution of an organic solvent would dissolve the photoresist, so that the resist components could impede the silanization process.

At the end, the substrate is consecutively cleaned in acetone and isopropanol, and dried under a stream of N_2. For investigating the immobilization of receptor molecules, the first deposited silane is the mPEG-silane and the second one is TESPSA.

For investigating patterns of hydrophilic within hydrophobic surface areas and for investigating the patterned immobilization of AuNPs, the first deposited silane is HFDMCS. The second silane is TESPSA, or no second silane is deposited after the plasma treatment.

3.2.3 TESPSA-based receptor immobilization

Fig. 3.2 summarizes the behavior of TESPSA in the presence of amino-terminated molecules and in aqueous environments. After immobilization on the surface (see Fig. 3.2a), the

succinic anhydride functionality can immobilize amino-terminated receptor molecules in a ring opening reaction under formation of an amide bond (see Fig. 3.2b). Or the anhydride can be hydrolyzed so that two carboxyl groups are formed (see Fig. 3.2c). Thus, prior to the immobilization of the desired amine molecules, the samples are cured and annealed in a furnace at 120°C for at least 1.5 h to remove any water from the surface and to dehydrate all succinic anhydride functionalities.[179,192]

In an initial test, to investigate the effect of water on the amine immobilization behavior, one half of a fully TESPSA-functionalized and annealed glass slide is dipped into a water bath for 1.5 h. Subsequently, the sample is immersed entirely in a 10 mM PBS solution (pH 7.4) containing 0.1 mM FAM labeled amino-terminated oligonucleotides for 30 min. After that, the glass slide is rinsed with DI water and dried under a stream of N_2. A typical fluorescence microscopy image is shown in Fig. 3.2d. There is a sharp edge along the centerline of the glass slide at which the fluorescence intensity strongly increases. This edge is a result of the hydrolysis of the succinic anhydride functionalities on the right-hand side and the annealed functionalities on the left-hand side prior to the oligonucleotide immobilization. On the left-hand side, the binding affinity towards the amino-terminated oligonucleotides is much higher, resulting in the visible fluorescence contrast. This
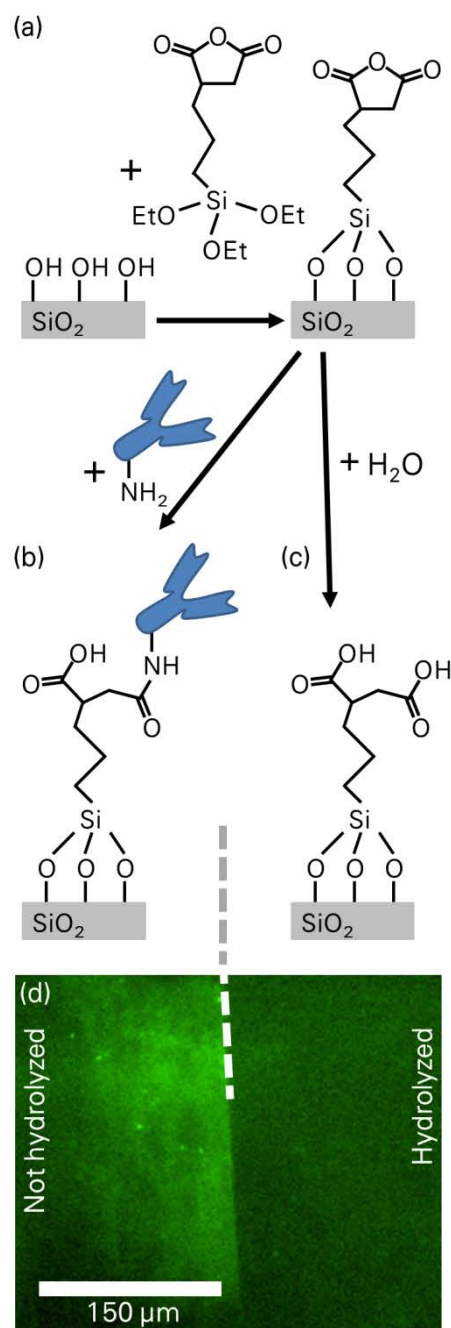

Fig. 3.2: TESPSA-based surface modification. Schematic drawings of (a) the covalent binding of TESPSA to an SiO_2 surface, (b) the covalent attachment of amines *via* a succinic anhydride functionality ring opening reaction leading to an amide bond formation, (c) the hydrolysis of the succinic anhydride functionalities resulting in the generation of two carboxyl groups. (d) Fluorescence microscopy image showing a glass slide of which one half was dipped into water prior to the immobilization of fluorescence labelled oligonucleotides. The visible fluorescence intensity edge goes along the middle line of the glass slide.

test demonstrates the importance of the annealing step.

For investigating the immobilization of antibodies and their specificity on a TESPSA-functionalized surface, the experimental set-up depicted in Fig. 3.3 is used. On the glass substrate, stripes of TESPSA are deposited next to stripes of the mPEG-silane (see Fig. 3.3a and section 3.2.2). Using the built-up described in chapter 2, a PDMS-based microfluidic structure is fixed on top of the prepared glass slide. The structure consists of four channels arranged in a cross like manner (see Fig. 3.3b) to run and microscopically observe four independent experiments simultaneously.

The composition of the receptor-analyte system applied for testing the receptor immobilization strategy is schematically shown in Fig. 3.3c. As model system three secondary antibodies with and without fluorescence label are used.

(i) A donkey anti-rabbit IgG as receptor molecule without fluorescence label (IgG$_{Receptor}$),

(ii) a rabbit anti-mouse IgG with green fluorescence label (IgG$_{Target\_green}$),

(iii) a donkey anti-goat IgG with red fluorescence label (IgG$_{Control\_red}$).

Fig. 3.3: Sample preparation for fluorescence microscopy-based investigations on receptor specificity. Schematic drawings of (a) the surface pattern consisting of stripes formed from TESPSA next to stripes derived from the deposition of mPEG-silanes, (b) the experimental layout of the PDMS-based microfluidic channels to run four experiments in parallel on one substrate, (c) the receptor-analyte combination – a receptor without fluorescence label is immobilized on the surface and specifically attracts the green fluorescently-labelled analyte, but not the red analyte.

IgG$_{Receptor}$ specifically interacts with the green analyte IgG$_{Target\_green}$ and repels the red analyte IgG$_{Control\_red}$. IgG$_{Target\_green}$ and IgG$_{Control\_red}$ also repel each other.

During the experiment, the microfluidic channels are consecutively filled with different antibody solutions, each with a concentration of 0.01 mg/ml IgG in 10 mM PBS buffer, pH 7.4. The solutions are allowed to incubate for 30 min, followed by a rinsing step using
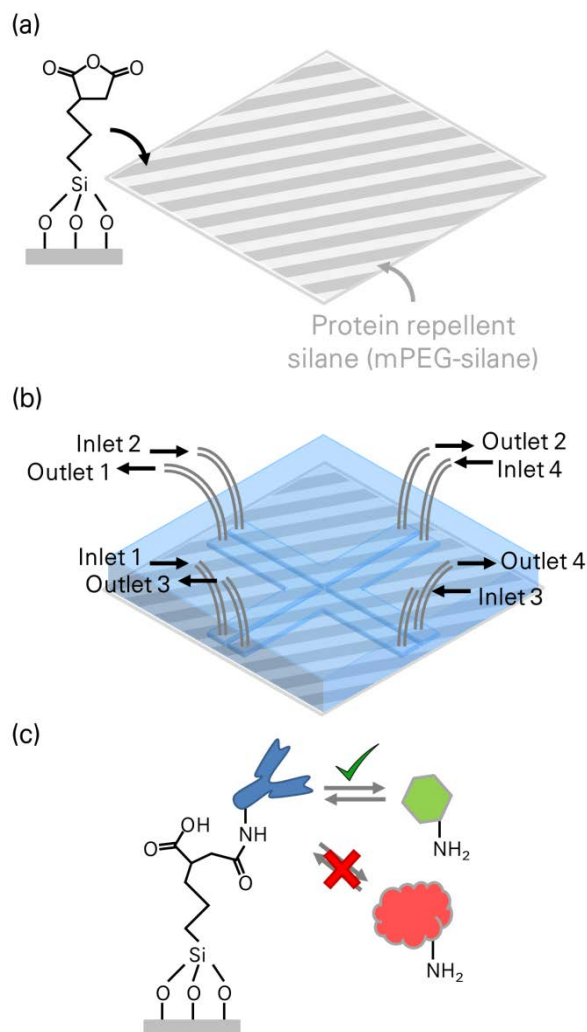
10 mM PBS-Tween (pH 7.4, 0.05% Tween20), before applying the next antibody solution. The sequences of antibody solutions in the different channels are as follows:

Channel 1: (1st) $IgG_{Receptor}$, (2nd) IgG_{Target_green}, (3rd) $IgG_{Control\_red}$

Channel 2: (1st) $IgG_{Receptor}$, (2nd) $IgG_{Control\_red}$, (3rd) IgG_{Target_green}

Channel 3: (1st) IgG_{Target_green}, (2nd) $IgG_{Control\_red}$

Channel 4: (1st) $IgG_{Control\_red}$, (2nd) IgG_{Target_green}

After each rinsing step the channels are investigated *via* fluorescence microscopy.

3.2.4 Patterned surfaces with hydrophilic and hydrophobic areas

Further applications of silane patterns are investigated by creating hydrophilic areas (equivalent to functionality B in Fig. 3.1) next to hydrophobic HFDMCS-based surface areas (equivalent to functionality A in Fig. 3.1). The hydrophilic areas are functionalized with TESPSA, or no silane is deposited after the plasma treatment.

Fig. 3.4 depicts the two applied patterning layouts. There is one pattern which divides the substrates in one hydrophobic and one hydrophilic half (see Fig. 3.4a) so that sufficiently large areas for contact angle measurements are provided. And there is one pattern for creating hydrophilic rings within a hydrophobic surface (Fig. 3.4b).

The wettabilities of the surfaces are tested *via* contact angle measurements. And the condensation behavior of water on the substrate surface is monitored. The condensation is induced by cooling down the substrate on a layer of ice in standard room conditions.

The immobilization of AuNPs is tested on substrates with the ring pattern. Aqueous suspensions of 20 nm AuNPs are pipetted on top of the substrate and blown off *via* a stream of N_2 after 30 min incubation time. Subsequently, the substrates are sonicated in acetone, isopropanol and DI water and dried under a stream of N_2. Before deposition the AuNP suspension is diluted 1:100 in di-water. The AuNP distribution is examined *via* SEM.
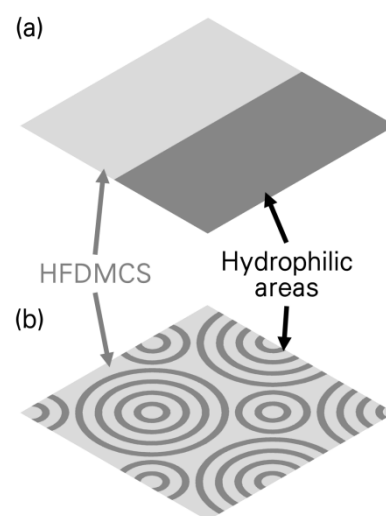

Fig. 3.4: Two surface patterning layouts are used for (a) dividing the substrate into one HFDMCS-based, hydrophobic and one hydrophilic half, and (b) for creating hydrophilic rings within a hydrophobic surface.

3.3 RESULTS AND DISCUSSION

3.3.1 Surface wettability dependent on surface activation and silane functionality

Fig. 3.5 summarizes the results of contact angle measurements on differently silanized surfaces. In Fig. 3.5a, different activation procedures and different APDMES silane deposition approaches are compared. In an initial experiment, based on common APTES protocols, silanization times of up to 60 min of an ethanol solution with 2 vol.% APDMES after a 5 min plasma activation are tested (green diamonds). A freshly activated substrate is highly hydrophilic with contact angles below 10°. After 30 min functionalization time the contact angles saturate at ~ 65°. Decreasing the plasma activation time to 15 s and the
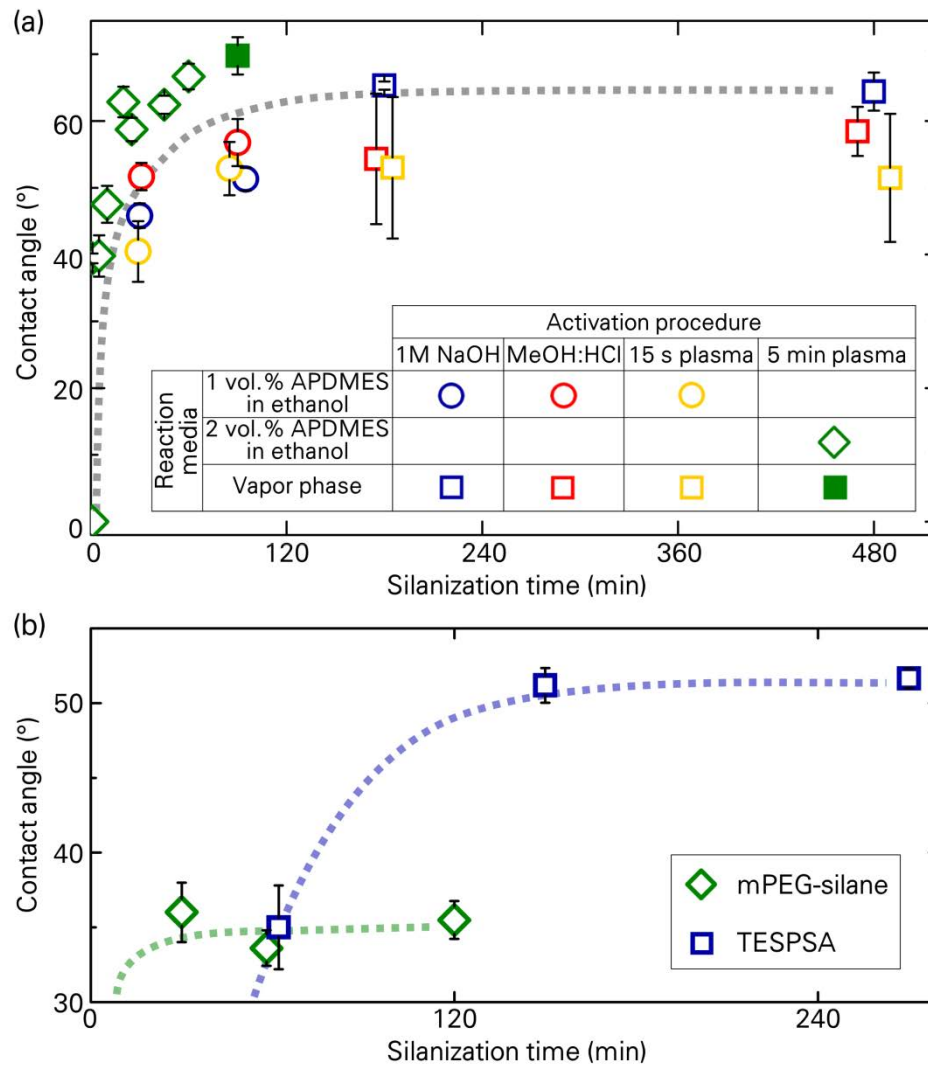

Fig. 3.5: Contact angle measurements on (a) APDMES-functionalized surfaces in dependence of activation procedure, silanization strategy and silanization time, (b) TESPSA and mPEG-silane-functionalized surfaces in dependence of functionalization time after 5 min plasma activation. TESPSA is deposited from vapor phase, mPEG-silane in ethanol solution. Dotted lines are guides to the eye.

silane concentration in ethanol to 1 vol.% reduces the maximum contact angle to ~ 53° after 90 min functionalization time (yellow circles). When activating the surface *via* 1M NaOH or 1:1 (vol./vol.) MeOH:HCl applying 1 vol.% APDMES in ethanol for the functionalization results in similar contact angles (blue and red circles). In case of an activation *via* 15 s plasma treatment or 1:1 (vol./vol.) MeOH:HCl, the silane deposition from the vapor phase does not result in contact angle values above 60°, also not after very long functionalization times of more than 4 h (yellow and red squares). The activation *via* 1M NaOH in combination with the vapor deposition leads to contact angles of ~ 65° (blue square), similar to the result of the 2 vol.% silane solution in ethanol after 5 min plasma activation. In the literature, for APDMES contact angles of ~ 50° are reported.[193] For APTES, there are values between 58° and 63°.[27,144,194] These data show that an activation *via* 1M NaOH or a long plasma treatment result in a proper silanization of the surface. The activation *via* 1:1 (vol./vol.) MeOH:HCl is not as efficient, which is also described elsewhere.[186] 15 s plasma activation are too short. With regard to the large standard deviations of the respective samples, it can be assumed that the activation is not complete and inhomogeneous. In view of the intended patterning of the surface, the dry plasma-based activation process is preferred for the subsequent experiments. Also the deposition from the vapor phase is of huge importance for the patterning strategy. The optimized protocol includes 5 min plasma activation and the deposition from the vapor phase for 90 min, resulting in contact angles of ~ 69° (filled green square).

For forming TESPSA stripes next to stripes of mPEG-silane, at least one of the two silanes must be deposited from the vapor phase for using the strategy presented in section 3.2.2. In Fig. 3.5b, the contact angles after an ethanol-based deposition of mPEG-silane and a vapor phase deposition of TESPSA are summarized. It is visible that the mPEG-silananized surface does not change its contact angle between 30 min and 120 min functionalization time. The contact angle is ~ 35°. A similar value is reported in the literature.[194] In the following, mPEG-silanization procedures 45 min functionalization time are applied to minimize the formation of multilayers of the triethoxysilane.

The contact angle of TESPSA saturates after 2.5 h at values of ~ 52°. This value is approx. twice as high as reported by Lee *et al.*.[195] however, in their publication also for APTES, compared to other references,[27,144,194] a significantly lower contact angle of ~ 43° is determined. In the following experiments, a TESPSA functionalization time of at least 3 h is applied.

The application of HFDMCS is particularly delicate. The chlorosilane is higly reactive, so that the storage conditions are very important. The utilization of HFDMCS being stored under N$_2$ atmosphere results in contact angles below 90°, despite a proper plasma activation and long functionalization times. Aliquoting HFDMCS under Ar atmosphere and storing the aliquots in an Ar atmosphere leads in subsequent experiments to contact angles of ~ 100° after 5 min

plasma activation and 60 min functionalization time. For a similar silane with three instead of one hydrolysable chlorine atom, contact angles of ~ 110° are reported in the literature.[194]

3.3.2 TESPSA-based receptor immobilization

Fig. 3.6 summarizes the outcomes of the three stages of the fluorescence microscopy-based antibody immobilization experiment. The microscopy images combine the information of the green and the red fluorescence filter sets. The four separate microfluidic channels are indicated by gray dotted lines. Green and red fluorescence intensities are measured along the white dashed lines across the images and plotted as gray values in the graphs below.

As schematically depicted next to the microscopy image in Fig. 3.6a, in channel 1 and 2 at first the $IgG_{Receptor}$ is immobilized by guiding it through the channels over the annealed TESPSA areas. In channel 3 and 4, IgG_{Target_green} and $IgG_{Control\_red}$ are immobilized, respectively. Green and red fluorescence signals are solely detected in the lower two channels. This is also visible in the gray value plots. Two intense green fluorescence peaks are detected in channel 3. The lower green peak in channel 3 is attributed to a decreased fluorescence intensity close to the channel wall. In channel 4, one intense red fluorescence peak is detected, and two peaks with lower intensities at positions very close to the channel walls. The peaks at positions close to the channel walls are always indicated with ▼. They also appear in the subsequent two stages, however, with changing intensities, because the lines, along which the gray values are measured, are not exactly identical in the different cases. The fluorescence intensities in channel 3 and 4 are used as references for the subsequent investigations of the receptor-analyte interactions in the second and the third stage.

From the microscopy image in Fig. 3.6a, it is already visible that the highest fluorescence signals are observed in all cases along identical stripes. Different patterns, at other parts of the channel confirm that the dark stripes are the areas that were covered with photoresist during the second plasma treatment (see Fig. 3.7). Since the dark stripes show similar gray values as the areas next to the microfluidic channels, they are assumed to efficiently repel antibodies or proteins, respectively, and, thus, to be still possessing the mPEG-functionality, despite the previous photoresist coverage.

In the second stage, in Fig. 3.6b, the addition of IgG_{Target_green} in channel 1 results in a strong green fluorescence indicating a specific interaction between $IgG_{Receptor}$ and IgG_{Target_green}. Weak red fluorescence signals are detected in channel 2 and channel 3, at positions where previously other antibodies were immobilized (indicated with *). This signal is attributed to minor unspecific interactions between $IgG_{Control\_red}$ and immobilized $IgG_{Receptor}$ in channel 2 as well as IgG_{Target_green} in channel 3. No similar effect could be observed in channel 4 for the green fluorescence signal. Thus, the $IgG_{Control\_red}$ is assumed to have a tendency to interact unspecifically with any antibody covered surface. In channel 4, the IgG_{Target_green}, however, proves that unspecific interactions are not due to unsaturated binding sites of the TESPSA
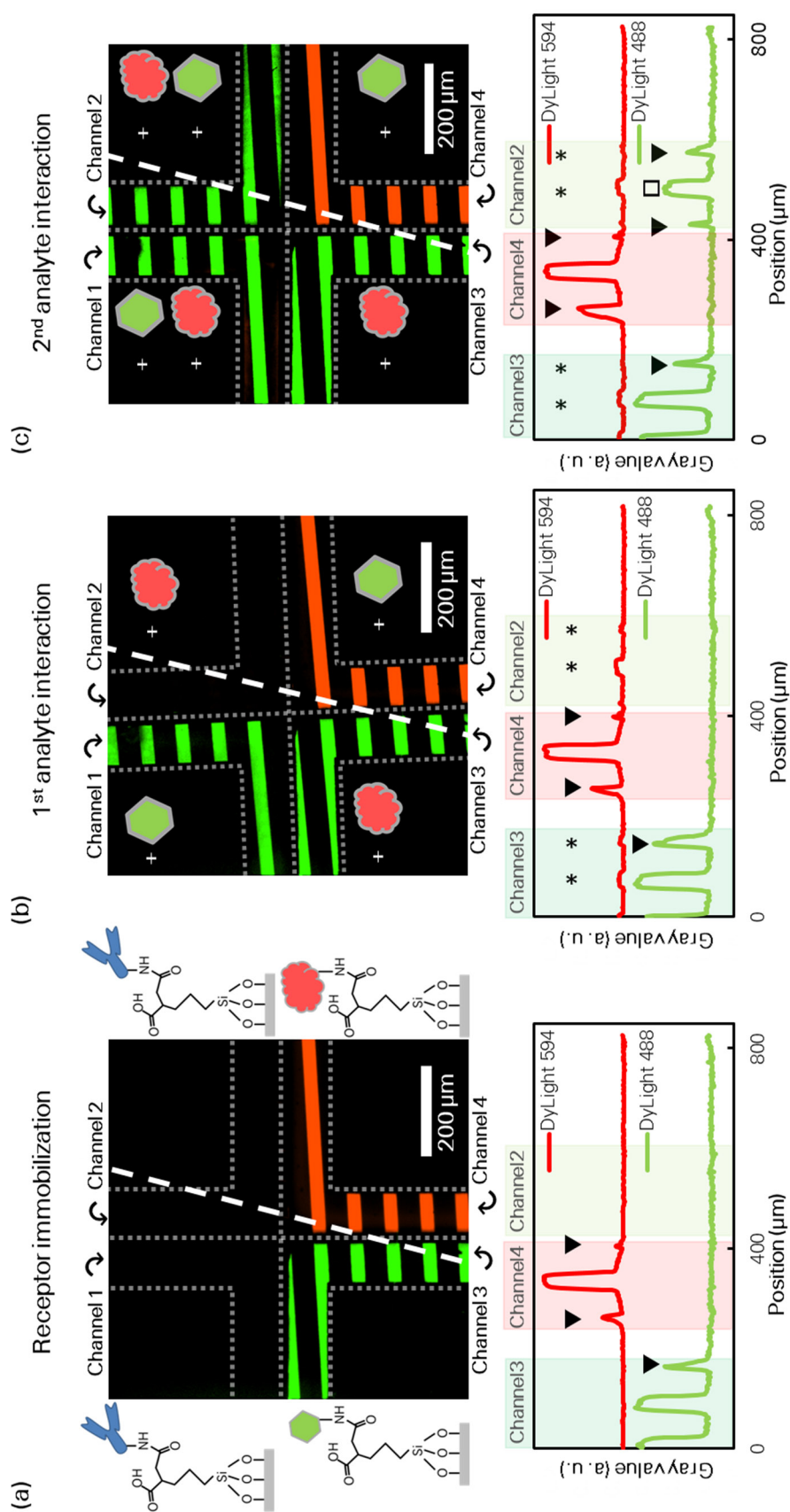
Fig. 3.6: Fluorescence microscopy investigations of receptor and analyte binding. Merged images of green and red fluorescence filter set-ups. In four microfluidic channels (indicated by gray dotted lines) receptor and analyte molecules were incubated with the surface in different orders as schematically depicted next to the channels. Below the microscopy images, the gray values for the green and the red fluorescence filter set-ups along the respective white dashed lines are plotted. Further explanations are given in the main text.

layer. A surface blocking, for example with bovine serum albumin,[27,196] might prevent undesired non-specific interactions entirely.

In the third stage, a high green fluorescence signal is detected in channel 2 (indicated with □). This signal is attributed to a specific interaction between the immobilized IgG$_{Receptor}$ and the IgG$_{Target\_green}$. The fluorescence intensity in channel 2 is not as high as in the reference channel 3. This result implies that during the initial binding of IgG to the TESPSA surface more molecules attach than during the specific receptor-analyte interaction. One reason might be that not all IgG$_{Receptor}$ are properly oriented. Or the equilibrium of the receptor-analyte interaction adapts to the space requirements of the IgG$_{Target\_green}$, while the covalent bond between IgG$_{Target\_green}$ and TESPSA cannot be reversed, independent of the density of molecules already attached.

Fig. 3.7: Diagonal lines implemented in the stripe pattern allow explicitly determining in which stripes TESPSA is deposited. The dark stripes were covered with photoresist during the second plasma treatment and the TESPSA deposition. The dark spots that overlap with the fluorescent lines are due to support posts of the PDMS channels preventing the channel collapse, as described in section 2.3.2.

In conclusion, the results demonstrate the successful TESPSA-based covalent binding of receptor molecules. Even multiple subsequent cleaning steps do not reduce the fluorescent signal. The bound receptors maintain their specificity. And an additional blocking of excess binding sites is not required. Thus, the receptor immobilization strategy presented in this chapter will strongly facilitate the development of sensors with high specificity towards selected analyte species.

3.3.3 Patterned surfaces with hydrophilic and hydrophobic areas

Two exemplary results of the patterning of the wettability of surfaces are depicted in Fig. 3.8. In initial tests, the contact angles of the surfaces after applying the patterning strategy are tested. As shown in Fig. 3.8a, the patterning allows creating hydrophilic ares directly next to hydrophobic ones. However, with ~ 13° the plasma treated surface in Fig. 3.8a has a considerably higher contact angle than the freshly plasma cleaned surface in section 3.3.1. This is due to the cleaning of the surface after the plasma treatment for removing the photoresist. During the cleaning procedure, the highly reactive, plasma treated surface interacts with organic components and impurities in the solvent bath so that the contact angle increases. The areas functionalized with TESPSA and HFDMCS show similar contact angles as determined in section 3.3.1 demonstrating that these surfaces are not affected by the patterning procedure.
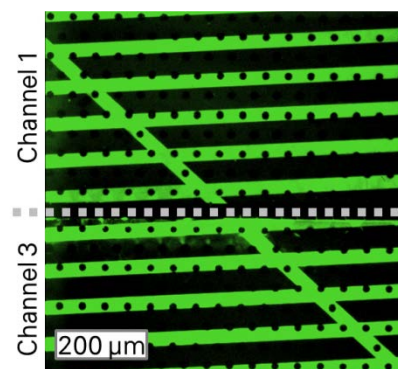
On the surface depicted in Fig. 3.8b, hydrophilic TESPSA-based rings are deposited in-between hydrophobic HFDMCS-functionalized areas. The visible droplet pattern results from the condensation of water on that surface. The condensation mainly occurs on the TESPSA areas under formation of relatively large drops. The amount of drops and the drop size on the HFDMCS areas is significantly smaller. A similar preferential condensation of water on the hydrophilic areas is observed for plasma treated rings within a HFDMCS surface. These results show that the applied patterning approach can also be used for creating surfaces that enable a passive control over the behavior of liquids.[182,183]

Fig. 3.8: Patterned wettability. (a) Contact angle measurement on a surface of which one half is functionalized with HFDMCS and one half is plasma cleaned. (b) Water condensation on rings of TESPSA-functionalized, hydrophilic areas within hydrophobic HFDMCS-functionalized parts.

The results of the deposition of AuNPs on such patterned surfaces are depicted in Fig. 3.9. In Fig. 3.9a, the boundary between a TESPSA-functionalized surface part and a HFDMCS-functionalized surface part is shown. It is visible that the AuNP density on the TESPSA part is much higher than on the HFDMCS part. A similar result is observed when using plasma treated surfaces instead of TESPSA-functionalized ones (see Fig. 3.9b). On both, TESPSA-functionalized and plasma treated surfaces $\sim$ 30 AuNPs/μm² are deposited. The AuNP density can be tuned by changing the dilution of the initial AuNP suspension prior to deposition. As can be seen from the insets in Fig. 3.9a,b the AuNPs are homogeneously

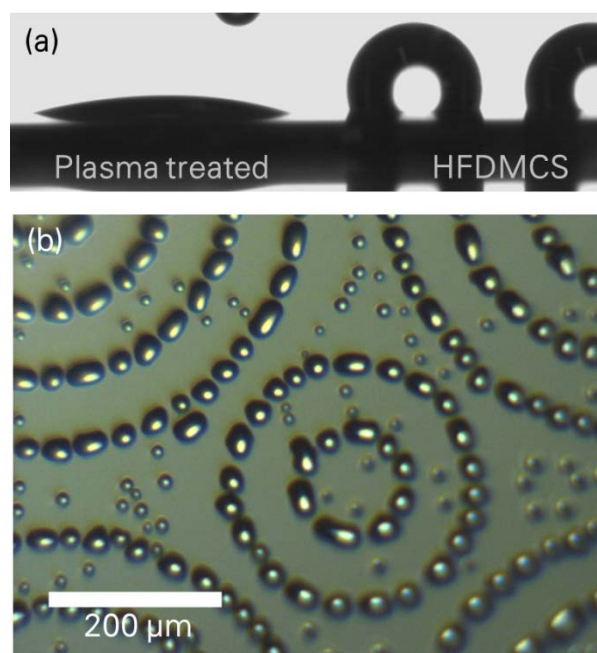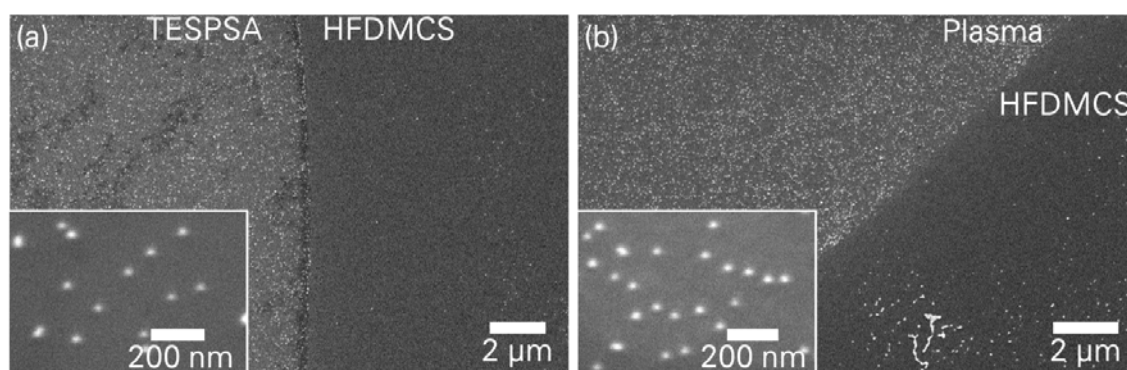Fig. 3.9: Patterned AuNP deposition *via* patterned surface silanization. (a) TESPSA- und HFDMCS-functionalized surface. (b) Plasma treated and HFDMCS-functionalized surface. Insets show TESPSA and plasma treated parts, respectively, at higher magnification.

spread. Unexpectedly, the surface charges introduced by the plasma treatment [197] appear to attract the BPEI stabilized and, thus, amino-terminated AuNPs to a similar extend as the TESPSA, even though on plasma treated surfaces no covalent bond can be formed. It must be noted that the high AuNP density is measured after cleaning the substrates using sonication. Such thorough cleaning conditions are required for preventing a contamination of the equipment utilized for the bottom-up growth of SiNWs described in section 4.2.1. In earlier works, a removal of AuNPs from the surface after cleaning was observed.[120]

In some cases, large agglomerations of AuNPs occur on the HFDMCS parts of the substrates, as can be seen in Fig. 3.9b. They might result from the formation of drops while blowing the AuNP suspension off the surface. Due to the hydrophobicity, possible remainings of the aqueous suspension will rapidly form tiny drops carrying many AuNPs to a small area and leave them on the surface owing to a fast evaporation. In subsequent AuNP deposition procedures, the AuNP suspension is rinsed off the surface under flowing water before continuing as described above (see section 3.2.4).

Apart from the few AuNP inhomogeneities in the HFDMCS parts, the silane- or plasma-based patterned deposition of AuNPs is possible with the developed strategy. This may become an alternative initial step in the bottom-up fabrication of arrays of vertical FETs with very high transistor densities [184,185] or arrays of 2D photonic crystals [184] described in the literature. Due to cross-contamination issues between the lithography devices required for the patterning and the SiNW growth chamber (see section 4.2.1), a patterned growth of SiNWs is not performed within this thesis.

3.4 CONCLUSION

In this chapter, the patterned functionalization of surfaces using different silanes is demonstrated. A novel receptor immobilization strategy is proposed and it is shown to enable a specific receptor-analyte interaction while making an additional passivation of excess binding sites dispensable. In the future, this strategy will strongly facilitate the functionalization of sensor devices.

Furthermore, the surface patterning is demonstrated to enable a passive control over the behavior of liquids and a localized deposition of AuNPs.

4 MULTIPLE SILICON NANOWIRE-BASED SENSING

This chapter describes the bottom-up growth of SiNWs using the vapor-liquid-solid (VLS) method,[198] and their assembly into parallel arrays of SB FETs.[199] The devices are passivated and implemented into microfluidic set-ups as described in chapter 2 of this thesis. In this ISFET configuration, pH- and ion-sensitivities are determined, and changes of the device behavior after a HFDMCS-based surface functionalization are investigated. Furthermore, the practicability of the TESPSA-based receptor immobilization strategy presented in chapter 3 for BioFET applications is tested.

4.1 MOTIVATION

As described in section 1.3, FETs are well suited for the detection of analytes. When using SiNWs as sensitive elements, as introduced by the work group around C. M. Lieber in 2001, due to their diameters in the range of the analyte dimensions and their huge surface to volume ratio, very low detection limits, in theory even the detection of single molecules, can be achieved.[19] The applicability of SiNW-based sensors is demonstrated in various publications on the detection of pH [19,28,29] chemicals,[19,30,31] proteins [19,22–24,32,33] and DNA [34] with detection limits down to the fM range. Also the real-time and label-free detection of single viruses has been shown,[35] as well as the detection of gases.[200,201]

In the experiments described within this chapter, the successful fabrication of parallel arrays of SB FET-based sensors at the Chair of Materials Science and Nanotechnology of Prof. Cuniberti at the TU Dresden, in cooperation with the NaMLab gGmbH, Dresden, is continued.[199,202] The fabrication is based on bottom-up grown SiNWs of which innumerable amounts can be produced in a single chemical vapor deposition (CVD) process. Compared to a laborious electron-beam lithography-based top-down production of SiNW FETs, the bottom-up approach is considered more cost-efficient, and devices with low defect densities,[36–38] much lower NW diameter [38,203] and competitive device performance [39] can be obtained through simpler methods. Bottom-up grown SiNWs are also advantageous for assembling polymer substrate-based flexible sensors.[40]

The basic layout of the devices fabricated within this thesis is introduced in Fig. 1.7a in section 1.3.3. As-grown intrinsic SiNWs are deposited on Si wafer substrates and covered with Ni electrodes. In a silicidation step, Ni diffuses into the Si core of the NWs forming the Ni silicide $NiSi_2$ and an up to atomically sharp $Si-NiSi_2$ semiconductor-metal interface. Introducing such Schottky contacts is relatively simple compared to the application of dopants in conventional MOSFET devices and enables high on/off current ratios.[199]
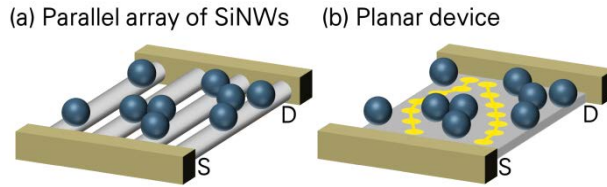
(a) Parallel array of SiNWs (b) Planar device

Fig. 4.1: Schematic drawing of randomly distributed analytes (blue spheres) on top of (a) a parallel array of SiNWs and (b) a planar semiconductor between source (S) and drain (D) electrodes. The inhomogeneous modification of the surface potential by the analytes provides percolation paths of unmodified resistivity in case (b). Percolation paths are depicted as yellow dotted lines. In (a), no percolation paths exist making the SiNW-based device more sensitive.

The NWs are deposited and aligned *via* a simple contact printing method.[204,205] By means of interdigitated Ni electrodes, hundreds of SiNWs per FET are contacted yielding low device-to-device variability for emerging research devices and high source drain currents, I_{SD}, in the µA range at low source drain voltages, V_{SD}, of 1 V or below. This enables a robust device operation.

In sensor applications, at low analyte concentrations, the parallel arrays are expected to be more sensitive than planar field-effect devices of similar sensor area. If the sensor surface is inhomogeneously covered with analytes, the inhomogeneous modification of the surface potential provides percolation paths of unmodified resistivity in the case of planar devices (see Fig. 4.1b). Due to the one dimensional current flow through SiNWs, there are no possibilities for such percolation paths once a NW is covered with analytes. Thus, at a similar coverage with analytes, the current is modulated more efficiently in parallel arrays of SiNWs (see Fig. 4.1a).

Also advantageous for sensor applications is the utilization of intrinsic SiNWs. Because of the low charge carrier density, the Debye screening length within the NWs spans the entire NW diameter.[206] This yields a large gating efficiency in case of surface potential changes and, thus, a high sensitivity of the devices. Additionally, applying intrinsic SiNWs makes the elaborate accurate control of the NW doping levels dispensable.[32]

For employing the devices in liquid environments, they must be protected against electrochemical degradation. Therefore, dielectric passivation layers made of Al_2O_3 or HfO_2 are deposited on top of the structures, including the source and drain electrodes, before assembling them in similar microfluidic set-ups as described in chapter 2 and using them in pH, ion and protein sensing applications.

As introduced in section 1.4 and section 3.1, the functionalization of the surface of a FET-based sensor is indispensable for a specific interaction with desired analytes. One milestone in the functionalization of sensor devices is the fabrication of true reference sensors,[109,207,208] which are insensitive to changes of pH or ion concentrations. Devices that react only to alterations of the electrostatic potential, *i. e.* the liquid gate voltage, but not to chemical changes would allow building a differential ISFET-reference FET set-up for minimizing the influences of drift or temperature.[106] Within this chapter the possibility of fabricating such true reference sensors *via* surface functionalization using the silane HFDMCS (see chapter 3) is tested.[207,208]

Furthermore, ion-sensitive FETs in a sensor set-up must interact specifically with only one target analyte while being unaffected by other molecules. In this regard, the TESPSA-based receptor immobilization strategy presented in chapter 3 is investigated in combination with the assembled bottom-up SiNW SB FET sensors.

In the first part of this chapter (section 4.2), the fabrication of sensors based on parallel arrays of bottom-up SiNW SB FETs with Al_2O_3 and HfO_2 dielectric surface layers is described. Subsequently, in section 4.3, the electrical characteristics of the fabricated devices are determined *via* back-gate measurements and under liquid gate conditions, and the pH and ion sensitivities of two kinds of dielectric surfaces – Al_2O_3 and HfO_2 – are examined. Furthermore, the applicabilities of the two dielectric surface types for fabricating a true reference sensor are investigated, and the TESPSA-based immobilization of receptor molecules and the resulting sensor specificities for particular analytes are tested.

4.2 DEVICE FABRICATION

In this section, the important steps towards the fabrication of parallel arrays of SiNW SB FETs are described. Along the description of the utilized recipes, fundamental information on the applied processes are provided and characteristic intermediate fabrication results are shown.

4.2.1 Bottom-up growth of SiNWs

SiNWs are catalytically grown with the help of AuNP seed particles in a vapor-liquid-solid (VLS) process, originally proposed by Wagner and Ellis in 1964.[198] AuNPs are deposited on a Si wafer surface according to the procedure described in section 3.2.4, however, without any previous patterning of the surface. Initially, as schematically depicted in Fig. 4.2, the growth behavior on two kinds of substrates is compared. BPEI-stabilized AuNPs are deposited on freshly air plasma treated or on TESPSA-functionalized wafers. Subsequently, the substrates are treated with a remote O_2 plasma (250W, 50 Pa, 20 sccm O_2, 30 min, ATV SRO-706 Reflow Oven, ATV Technologies, Germany) to remove all organics from the surface [191] before starting the growth procedure in a customized Precision 5000 CVD system (Applied Materials, USA).

SiNWs are grown at 450°C in an atmosphere with equal flow of H_2 and SiH_4 at a pressure of 6.67 kPa (100 sccm total flow). H_2 is used as carrier gas, SiH_4 as precursor for the formation of Si. As can be seen from the Au-Si phase diagram [209] in Fig. 4.3, pure AuNPs are solid at the given temperature. According to the VLS model,[120,198,209] SiH_4 adsorbs on the surface of the AuNPs and decomposes catalytically into Si and H_2. Si diffuses into the metal (stage (i) in Fig. 4.3). Due to the Si uptake, a liquid Au-Si alloy is formed, and with increasing Si content the AuNPs become liquid Au-Si droplets (stage (ii) in Fig. 4.3). The SiH_4 precursor continues adsorbing and catalytically cracking at the Au-Si droplet surface so that the Si concentration
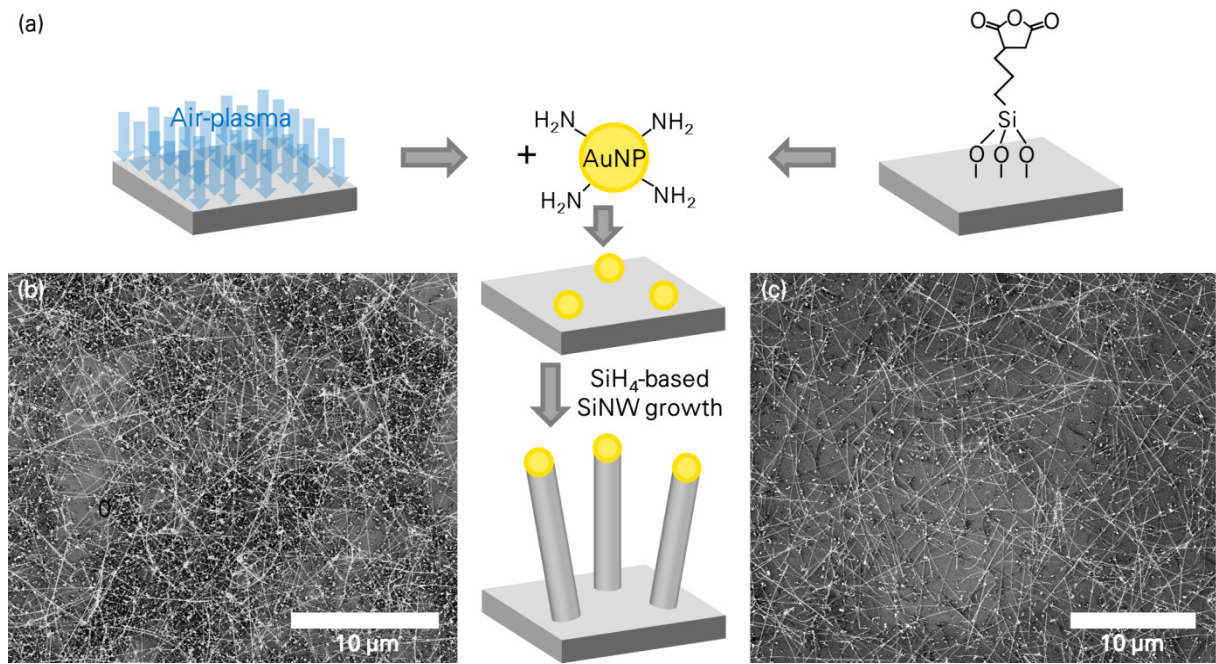
(a)

Fig. 4.2: SiNW growth. (a) Schematic drawing of the procedure, starting with seed AuNP deposition on air plasma cleaned or TESPSA functionalized surfaces. The seed NP are used for a catalytic growth of SiNW in a SiH_4-enriched CVD atmosphere. SEM images (courtesy of I. Ibrahim) show the grown SiNWs on (b) an initially plasma treated SiO_2-coated wafer, (c) an initially TESPSA functionalized wafer.

further increases until the right hand side liquidus line in Fig. 4.3 is reached. Beyond that, a Si oversaturation occurs and excess Si precipitates at the interface between Au-Si droplets and growth substrate. According to the phase diagram, the precipitate is pure Si, since there is no Au-Si solid solution. After a first monolayer of Si with approximately the diameter of the Au-Si droplet is deposited, the next monolayer is formed on top. With each deposited layer, the Au-Si droplet is pushed further away from the substrate and a SiNW is formed (stage (iii) in Fig. 4.3).

Based on this mechanism, the diameters of the SiNWs are close to the initial diameters of the AuNPs.[184,202,210] Within this thesis, AuNPs with nominal diameters of 20 ± 3 nm (nanoComposix Europe, Czech Republic) are applied. The NWs are found to be of similar width. In earlier studies, the grown SiNWs are demonstrated to be single crystalline with low defect densities.[36–38]

It is important that during the growth the precipitates and, thus, the formed SiNWs are made of pure Si. Incorporations of Au into the NWs would affect the characteristics of subsequently assembled FETs by creating deep charge traps [211,212] or by creating mid gap states that promote charge carrier recombination.[209,213]

The SEM images in Fig. 4.2 show that the growth of SiNWs is not influenced by the initial AuNP deposition procedure. Both the air plasma- and the TESPSA-based approach yield similar growth results. Due to its simplicity, for subsequent NW growth, the air plasma-

based deposition of AuNP seed particles is applied. In previous works, the AuNPs are deposited from citrate stabilized AuNP solutions,[120,202] with promotion of the AuNP adhesion *via* a thin polymer film.[202] In most cases, such citrates contain Na$^+$ ions [214] which must be avoided in Si semiconductor processing to prevent a degradation of the electrical properties of the devices.[215] Therefore, the sodium-free AuNP deposition developed within this thesis is considered an important advancement in the fabrication of high quality bottom-up SiNW FETs.

The NW growth conditions are chosen in such way that the catalytic decomposition of SiH$_4$ at the AuNP surface is predominant over a thermal decomposition at other locations of the substrate or the CVD chamber.[216] However, the flakes below the grown SiNWs in Fig. 4.2b,c are assumed to be amorphous Si,[202] which indicates that the applied recipe can be further optimized,

Fig. 4.3: Successive Intermediate stages of catalytic VLS bottom-up growth of SiNWs projected onto Au-Si phase diagram [208] to illustrate the compositional and phase evolution during the growth process. At temperatures above 363°C, at stage (i) SiH$_4$ precursor gas, depicted as red circles, decomposes catalytically at the AuNP surface into Si and H$_2$. The yellow circle depicts an AuNP. Si diffuses into the AuNP and Si and Au form a liquid alloy. After taking up sufficient amounts of Si to pass the first liquidus line, at stage (ii) an entirely liquid Au-Si droplet is formed. The increasing reddening of the droplet represents the increasing Si concentration. The droplet further absorbs Si *via* SiH$_4$ decomposition at its surface. After passing the second liquidus line, a Si oversaturation occurs and pure Si precipitates at the droplet-wafer interface. All subsequent precipitations are stacked onto the previous ones so that a NW is grown at stage (iii).

e. g. by testing reduced growth temperatures. The growth time has to be adjusted to the desired NW length. After 30 min, there are up to 30 µm long NWs which is sufficient to bridge the 10 µm distance between the Ni electrodes in the intended device design (see Fig. 4.6). The detailed parameters of the recipe are given in the appendix.

Due to initial repair issues with the NW growth furnace, within this work SiNWs grown by S. Pregl are used for the further device fabrication described in the following sections. The according NWs are grown from citrate stabilized 20 nm AuNPs (Plano GmbH, Germany) deposited on a poly(diallyldimethylammonium chloride) coated wafer. Prior to the growth organic components are removed in an O$_2$ plasma, combined with an O$_2$ anneal (1 kPa, 200 sccm O$_2$, 250 W remote plasma, 400°C, 15 min & 12.5 kPa, 200 sccm, 400°C, 15 min, ATV SRO-706 Reflow Oven, ATV Technologies, Germany). The growth is performed in a CVD hot-wall reactor (450°C, H$_2$:SiH$_4$, 10:1, vol./vol., 6.5 kPa, ATV PEO-601, ATV Technologies, Germany).[202]
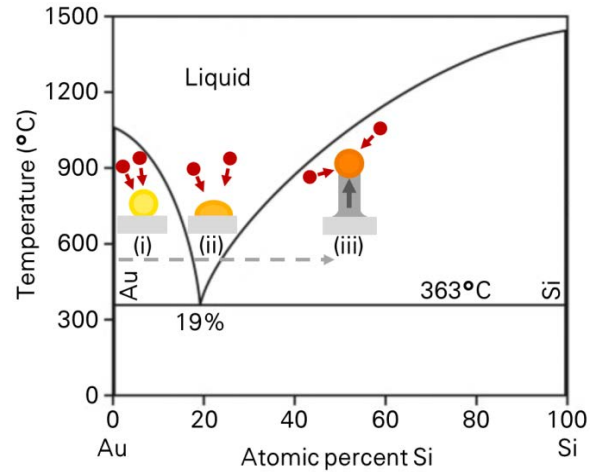
4.2.2 Aligned deposition and oxidation of SiNWs

After their growth, the SiNWs are transferred from the growth substrate (see Fig. 4.4a) to a receiver substrate on which all further device fabrication steps are performed. The transfer method is named "contact printing".[204,205] It starts by cleaving a small piece of approx. 12 x 12 mm² off the growth substrate and by attaching a 10 x 10 x 10 mm³ steel cube on its backside using double sided scotch tape. The receiver substrate is fixed on a table *via* a "Gel Box" (Gel-Pak, USA) as adhesive underground which also allows for a fast release later on. Then the growth substrate is put on top of the receiver substrate. Under the weight of the iron cube, the SiNWs are pressed against the receiver substrate surface. Using tweezers, the growth substrate is pushed manually a few millimeters in one direction up to an undefinable point, where the friction increases significantly, and slightly beyond. During that motion, SiNWs are ripped of the growth substrate and deposited on the receiver substrate with an alignment parallel to the pushing direction (see Fig. 4.4b,c). It is assumed that the SiNWs adhere to the receiver substrate *via* hydrogen bonds between the -OH groups on the wire surfaces and on the substrate surface or *via* covalent Si-O-Si bonds similar to ones presented in Fig. 1.10c,d in section 1.4.2.3.[217]

To prevent the formation of scratches on the receiver substrate, it is important to thoroughly blow off any dust or dirt particles from the growth substrates *via* N_2 gun prior to the printing. Also the receiver substrate is cleaned in advance, by successively sonicating it in acetone and isopropanol and blowing it dry under a stream of N_2. Any scratch that is formed during the contact printing could breach the surface oxide of the receiver substrate and cause leakage currents through the bulk Si yielding defective devices. To minimize the probability for cracking the oxide, wafers with particularly thick 1.5 µm thermal oxide (single side polished, degenerately *p*-doped, Siegert Wafer, Germany) are used as receiver substrates.

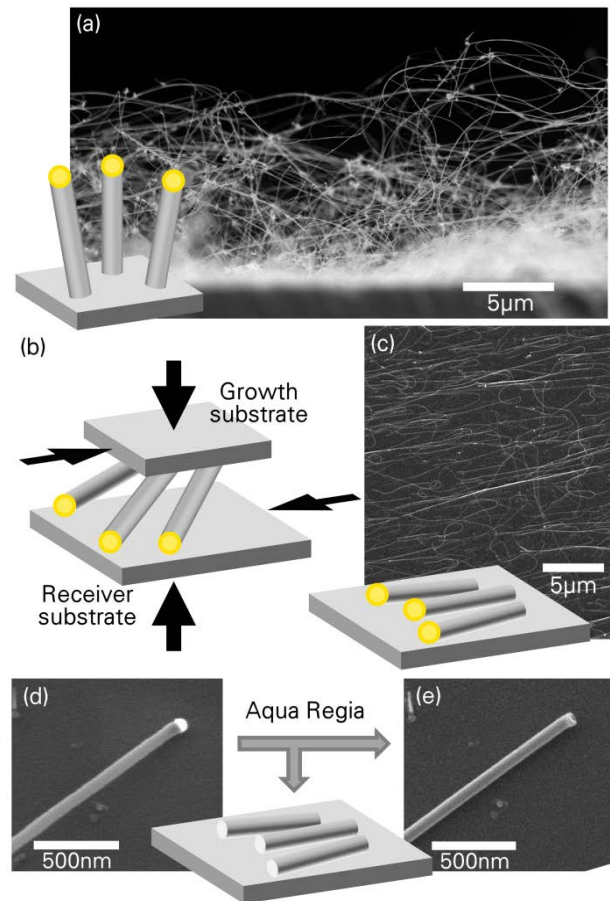
Fig. 4.4: Device preparation stages before contacting SiNWs depicted *via* SEM images and adjacent schematic drawings. (a) Sideview on as-grown SiNWs. (b) Schematic pressure and substrate movement directions during contact printing transfer of SiNWs from growth to receiver substrate. (c) As-printed SiNWs. (d & e) One SiNW before and after removal of catalyst NPs at the NW tip *via* aqua regia.

Having the SiNWs deposited on the chip, before applying any high temperature device fabrication steps the catalytic particles at the tips of the NWs (see Fig. 4.4d) must be removed. As mentioned in section 4.2.1, Au has a negative impact on the device properties and at temperatures above 363°C a liquid alloy would form and destroy the NWs. Additionally, a contamination of the utilized furnaces with Au must be prevented. Therefore, the chips are put into aqua regia (HNO$_3$:HCl, 1:3, vol./vol.) for 4 h and then thoroughly rinsed with water. The comparison of the same SiNW before and after the aqua regia treatment in Fig. 4.4d,e shows that the procedure effectively dissolves the Au.

In the next step, a thermal oxide shell is formed around the SiNWs to replace the native SiO$_2$ and, thus, to reduce surface charge densities [218] and improve on/off current ratios and device hysteres.[120,219,220] *Via* a rapid thermal processing furnace (RTP, AST Electronic GmbH, Germany) the chips are oxidized at 875°C in a 100 kPa O$_2$ atmosphere (flow rate 100 slm) for 6 min yielding an approx. 6 nm thick oxide shell. In a subsequent forming gas anneal (H$_2$:N$_2$, 1:20, vol./vol., 100 slm) at 450°C at 100 kPa for 10 min, remaining dangling bonds at the interface between the Si core and the oxide shell are saturated.[99,120,221,222]

4.2.3 Contacting the SiNWs

For contacting the printed SiNWs, interdigitated Ni electrodes are deposited on top of them (see Fig. 4.5a,b,d,e) using UVL in combination with a lift-off step. At first, the electrode patterns are defined using AZ5214e image reversal photoresist as negative resist, so that
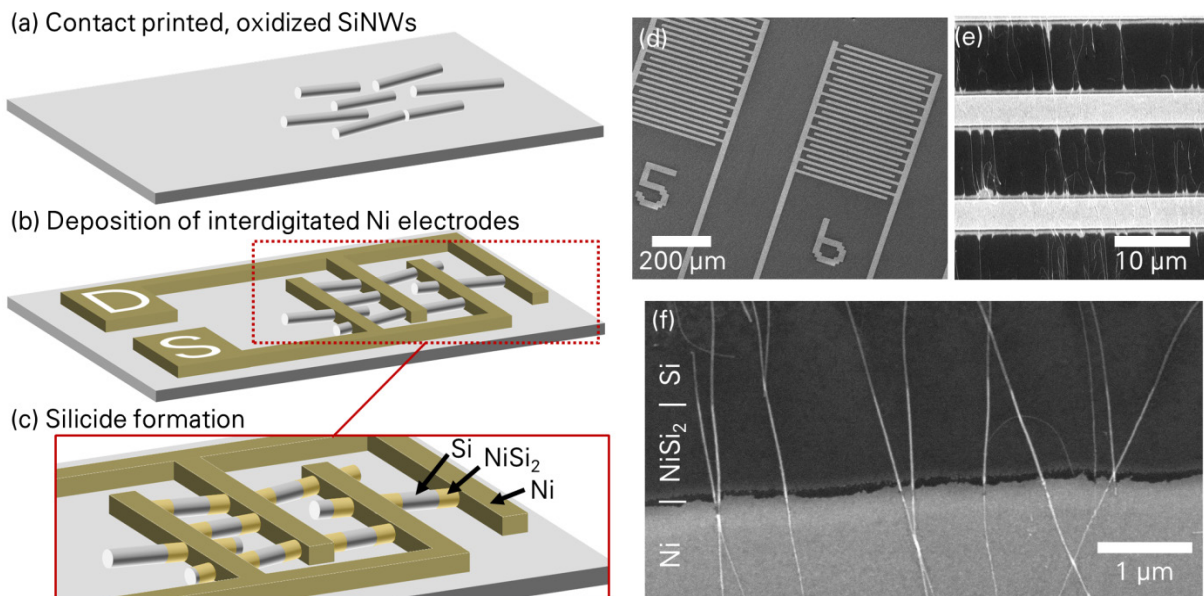
Fig. 4.5: Contacting of the SiNWs. (a) Schematic drawing of contact printed, oxidized SiNWs which are (b) covered with interdigitated source (S) and drain (D) Ni electrodes after UVL, HF-dip, Ni deposition and lift-off. (c) Enlarged view on red labeled section in (b) after the Ni silicide formation depicted by a color change at the NW tips. (d & e) SEM image of SiNWs contacted with interdigitated Ni electrodes. (f) SEM image of SiNWs covered with Ni electrode. Bright parts of the SiNWs consist of NiSi$_2$.

after the development the resist structures show an undercut which facilitates the lift-off later on (see Fig 1.1c in section 1.1). A detailed recipe for applying the photoresist is provided in the appendix. Compared to common AZ5214e protocols, in this work only about half of the spin coating spinning speed (2000 rpm) is used during the chip fabrication to obtain thick resist layers (~ 1.9 µm). This is important for the next step, to withstand the immersion of the sample in a 1% aqueous hydrofluoric acid (HF) solution.

HF is used to locally remove the oxide shell from the SiNWs before the Ni deposition to ensure a direct contact between the Si core and the metal. Since HF also penetrates the resist, a high resist thickness is applied to elongate the possible HF etching times. SiNWs with 6 nm thick SiO_2 shells are etched for 80 s.

Subsequently, the chips are rinsed with water and dried under a stream of N_2, and transferred into the sputtering machine (High Resolution Ion Beam Coater, Gatan, Inc., USA). In total, beetwen the etching in HF and the transfer of the sample into the vacuum of the sputtering device, maximum 4-5 min may pass, in order to prevent a re-oxidation of the freshly etched Si parts. Such a fast transfer is supported by the load lock system of the sputtering machine utilized in this thesis, which brings the sample into its permanently evacuated main chamber within 2 min.

During the sputtering process, the sample is slowly rotated to achieve a homogeneous Ni deposition. Due to a close distance between sample and sputter target, the incident material beam is not focused, so that occasionally Ni is deposited at areas beneath the undercut of the photoresist yielding undefined Ni thicknesses in these parts. One further disadvantage of the undercut is the etching of the oxide shell of the SiNWs at positions where no Ni is deposited. In these areas, later on, a native oxide is formed. The silicidation length of the devices, described in the next paragraph of this chapter, must be longer than the width of the undercut (~ 500 nm) to make sure that the Ni-$NiSi_2$ segments are covered with a thermal oxide for optimium device characteristics. The important advantage of the undercut is the facilitated lift-off of the photoresist. The resist is dissolved in acetone lifting the deposited Ni at all areas but the electrode and alignment mark positions. Alignment marks are deposited to enable a correct positioning of the mask in subsequent UVL steps (see Fig. 4.6). Detailed parameters of the recipe for the lift-off procedure are provided in the appendix.[223]

The final step for a proper contacting of the SiNWs is the axial intrusion of Ni silicide leads into the silicon core of the NW *via* diffusion. The Ni-Si system and the conditions for the diffusion-based formation of its various silicide phases are well studied for bulk materials, due to their importance in semiconductor industry as contact materials with low electrical resistance and high temperature stability.[224,225] For the silicidation process within SiNWs, different phase formation behavior is observed.[226,227] With increasing silicidation time, Ni steadily diffuses deeper into the SiNWs and forms metallic single crystalline $NiSi_x$ phases with up to atomically sharp $NiSi_x$-Si interfaces.[227–229]

Within this work, the silicidation is induced by annealing the devices in forming gas atmosphere (H_2:N_2, 1:20, vol./vol., 100 kPa, 100 slm) at 450°C for 90 s in an RTP furnace (AST Electronic GmbH, Germany). The heating and cooling ramps during the process are 10 K/s. Under these conditions, axially intruded single crystalline $NiSi_2$ segments with atomically abrupt $NiSi_2$-Si interfaces are formed inside the oxide shell of the SiNWs at the NW ends, as schematically depicted in Fig. 4.5c.[230] After 90 s silicidation time, a silicidation distance of approx. 3 µm is achieved.[202]

Due to cross-contamination issues between the RTP furnace and the single-NW devices fabricated in chapter 5, another furnace must be used for their forming gas anneals. In the utilized ATV SRO-706 Reflow Oven (ATV Technologies, Germany) relatively low

Fig. 4.6: Layout of the device masks. The blue mask defines the electrode structure and the alignment marks. The red mask is for a passivation layer which opens contact windows to the SiNWs in-between the interdigitated electrodes and on top of the contact pads. The red mask also has alignment marks which enable a correct adjustment of the two layers. In total the chip layout has a size of 15 x 15 mm², enabling an implementation in a multiplexed SD card-based transportable biosensor system.[223] The space between interdigitated electrodes and the design edges as well as the contact pads is sufficient to implement a microfluidic channel system on top of the design (see also Fig. 4.7b). The distance between the electrode fingers, depicted in the black and green insets, is 10 µm.

maximum heating and cooling ramps and low working gas pressures must be applied. In Fig. 4.5f the SiNWs show a silicidation length of approx. 1 µm after a forming gas anneal (N_2:H_2, 10:1, vol./vol., 1 kPa, 450°C) for 3 min 20 s, with a heating ramp of 2.5 K/s and a cooling ramp of 1.8 K/s. This recipe is used for the SiNW devices described in chapter 5.

The tip shapes of the metallic silicide contacts towards the intrinsic Si parts of the NWs lead to local enhancements of the electric fields which results in a better gate coupling and a thinning of the SB width and, thus, effectively in a lowering of the SB yielding lower device resistivity.[199,230] Since the annealing is performed in forming gas atmosphere, one additional effect of the procedure is the hydrogen passivation of dangling bonds at the oxide-Si interface which further improves the electrical behavior.[99,120,221,222] Due to the small lattice mismatch of 0.4% between Si and $NiSi_2$, there are almost no deformations visible along the silicide ends of the NWs.[231]

4.2.4 Device passivation and implementation in microfluidic set-up

For sensing applications in liquid environments, the FET devices have to be protected against electrochemical degradation. Taking into account that the SiNWs are surrounded by a passivating oxide shell, it would be sufficient to insulate the Ni electrodes with a
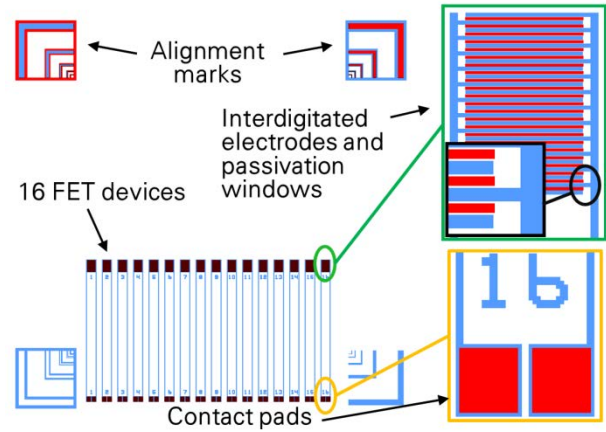
photoresist.[28] However, in earlier investigations within the workgroup, the resists AR-N 4340 S5 (Allresist, Germany) and SU-8 (MicroChem Corp., USA) did not yield the required passivation reliability. Additionally, SiO_2 covered devices have a relatively low pH sensitivity of approx. 35 to 45 mV/pH.[29,106] They are prone to ion diffusion [232] and show hysteretic behavior in pH measurements.[28,232] Two types of thin dielectric films are tested on different devices. (i) 20 nm Al_2O_3 or (ii) a stack of 20 nm Al_2O_3 and 4 nm HfO_2 are deposited on top of the respective chips to achieve a passivation of the electrodes. Both of these gate dielectrics are reported to provide high pH-sensitivities up to the Nernst limit of 59.5 mV/pH (at 300 K) [29,105] with low dependency on the salt concentration of the sample solution,[105,233] and low leakage currents between sample solution and FET electrodes.[234] Additionally, Al_2O_3 is known to exhibit low ion diffusivity [232] and to yield low pH-related hysteresis effects.[235] HfO_2 surfaces are often used for applications over broad pH ranges as they are chemically inert to most acidic and basic solutions.[105]

The dielectrics are deposited *via* atomic layer deposition (ALD). In an ALD process, the substrate is sequentially exposed to commonly two reactive gaseous precursors. The materials adhere in monolayers to and react with the surface building up step-by-step a film of the desired material.[236]

Within this work, 20 nm Al_2O_3 films are deposited in an ALD chamber (Roth & Rau AG, Germany) using Trimethyl Aluminium (TMA) and ozone (O_3) as reactants. At 300°C, 266 cycles of the following procedure are performed: introduction of TMA for 20 ms, N_2 purge for 5 s, introduction of O_3 and reaction time of 5 s, N_2 purge for 3 s.

Stacks of 20 nm Al_2O_3 and 4 nm HfO_2 are deposited in another ALD chamber (FHR-ALD 300, FHR Anlagenbau GmbH, Germany) using TMA and O_3, and ethylmethylaminohafnium (TEMAHf) and water (H_2O) as reactants, respectively. For the Al_2O_3 layer, 222 cycles of the following procedure are performed: introduction of TMA for 0.2 s, N_2 purge for 0.3 s, introduction of O_3 und reaction time of 1.3 s, N_2 purge for 3 s. For the HfO_2 layer it is 50 cycles of: introduction of TEMAHf for 5 s, N_2 purge for 2 s, introduction of H_2O und reaction time of 2 s, N_2 purge for 6 s. The deposition temperature is 250°C.

For contacting the devices, on top of the contact pads the passivation layers are etched back *via* UVL using AZ5214e as positive photoresist and 1% HF solution as etchant for 2 min. The design of the applied photomask is similar to the one shown in red in Fig. 4.6, however, without the opening stripes on top of the NWs. A schematic image of the final device is shown in Fig. 4.7a, a photograph of an entire finished chip in Fig. 4.7c.

Having completed the chip fabrication, the device can be assembled into a microfluidic system using the technique described in chapter 2. A schematic drawing and a photograph of the assembled set-up and a picture taken during the measurement of a liquid sample is shown in Fig. 4.7b,d,e. A PDMS-based microfluidic channel of approx. 12 x 2 x 0.5 mm³ size
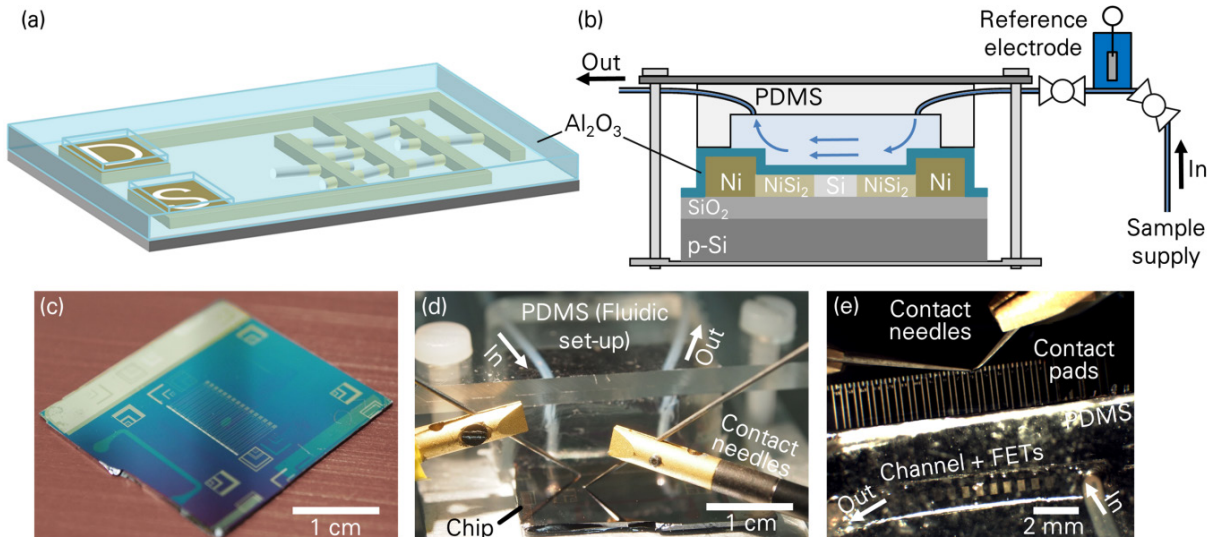
Fig. 4.7: Device passivation and assembly into microfluidic set-up. Schematic drawings of (a) Al_2O_3 passivated SB FET with back etched openings for contacting source (S) and drain (D) contact pads, (b) device implemented in microfluidic set-up as described in chapter 2. (c) Photograph of finished chip. (d) Assembly of chip and microfluidics under tip probe station for electrical measurements. (e) Picture taken *via* stereo microscope of tip probe station during FET measurements in liquid environment.

is positioned manually on top of the FETs and fixed *via* screws of the sample holder. In Fig. 4.7e, it is visible that the long distance between the interdigitated electrodes and the contact pads enables a convenient contacting of the devices using the contact needles of a tip probe station.

An Ag/AgCl reference electrode is used for applying the liquid gate voltage during measurements. The electrode is dipped into a 3 M KCl internal filling solution, saturated with AgCl, of a flow through housing (Microelectrodes, Inc., USA) which is implemented into the inlet tubing system. Within the housing, a ceramic frit or frit membrane, respectively, separates the internal stationary 3 M KCl solution from the transfluent sample solution. To maintain the quality of the frit membrane, it must be in contact with 3 M KCl on both sides at all times, when no experiments are performed. Two shut off valves with screw fittings are integrated into the tubing system to enable a separate storage of the tubing section which the reference electrode housing is connected to (see Fig. 4.7b). During storage that tubing section is filled with 3 M KCl and the valves are shut off.

Liquid gate measurements are performed using a source measure unit (SMU, Keithley Source Meter 2604B, Keithley Instruments, Inc., USA) in combination with a DPP105-V-AI-S micropositioner (Cascade Microtech, Inc., USA) probe station. During measurements the sample solutions are drawn through the microfluidic set-up under reduced pressure using a syringe pump (PHD 2000, Harvard Apparatus, USA). Switching between different solutions is performed using an eight-position selection valve (MLE GmbH, Germany).

Within this thesis, each FET is measured separately. The chip design, as depicted in Fig. 4.6, enables a device implementation into a multiplexed SD card-based transportable biosensor

system.[223] Here, since the applied chips are subjected to various chemical experiments, to facilitate the experimental procedure, they are not integrated into the multiplexer.

4.3 ELECTRICAL CHARACTERISTICS AND SENSOR APPLICATIONS

In this section, the electrical characteristics of the fabricated devices are described. I_{SD}-V_G transfer curves of the devices at different fabrication stages are recorded in dry conditions using a back-gate arrangement. After the deposition of dielectric thin films on top of the FETs, in the second part of this section, the passivated devices are additionally characterized under aqueous solution *via* liquid gate measurements.

It has to be noted that within this work it is primarily intended to use the devices for sensing applications and for surface functionalization investigations. Therefore, at any time, characterization measurements are done cautiously avoiding excessive electric fields, to prevent *e. g.* a breakdown of the dielectrics. This holds particularly true when gating the devices through liquid solutions (see section 4.3.2). In consequence, the applied V_G ranges are commonly not sufficient to perfectly switch the devices into their *on*- or *off*-states. Thus, the data are analyzed with regard to the achieved maximum I_{SD} currents of the devices, I_{max}, instead of the *on*-currents, I_{on}. Furthermore, not the I_{on}/I_{off} ratios but the I_{max}/I_{min} ratios of maximum and minimum currents are determined. The minimum absolute inverse slopes of the logarithmic I_{SD}-V_G curves are designated as subthreshold swings, and the maximum absolute slopes of the linear I_{SD}-V_G curves as transconductances (see also Fig. 1.5e).

If not stated otherwise, when determining the transfer characteristics of the devices the gate voltage sweeps start at the largest negative voltage depicted in the respective graphs, going to the highest positive voltage and back to the initial negative voltage again.

In the third part of this section, the pH and ion concentration sensitivities of the devices are determined. It is explained how the data are collected and how the data are evaluated. Additionally, it is tested, whether a HFDMCS-based surface functionalization enables the fabrication of a true reference sensor.[109,207,208]

The last part describes the applicability of the TESPSA-based receptor immobilization method described in chapter 3 for engineering highly sensitive and highly specific BioFET devices.

4.3.1 Back-gate characteristics

At different stages of the device fabrication process described in section 4.2, the transfer characteristics of the FETs are determined *via* back-gate measurements using a PM8 Prober (Cascade Microtech Inc., USA) in combination with a B1505A Power Device Analyzer/Curve Tracer including two High Power Source/Monitor Unit Modules (Agilent Technologies, Inc., USA). The back-gate voltages, V_{BG}, are regulated *via* a metal chuck on top of which the

measured chips are fixed using vacuum. Measuring one I_{SD}-V_{BG} forward-backward sweep takes a few seconds depending on the I_{SD} current levels. Close to the resolution limit of the analyzer system, at around 10^{-11} A, the holding (integration) time for each measuring point increases.

The device characteristics are measured (i) directly after the deposition of the Ni contacts, (ii) after the silicidation process (see section 4.2.3) and after depositing passivation layers made of (iii) Al_2O_3 or (iv) Al_2O_3+HfO_2 (see section 4.2.4). Representative I_{SD}-V_{BG} characteristics of devices at the different fabrication stages, measured at $V_{SD} = 1$ V, are shown in Fig. 4.8a. Fig. 4.8b and Fig. 4.8c present the average maximum currents and I_{max}/I_{min} ratios as well as the average subthreshold swings and transconductances at the different fabrication stages. For all plotted points a sample size of $N = 15$ devices is used.[1]

The individual I_{max} values and the I_{max}/I_{min} ratios of each device are extracted from its
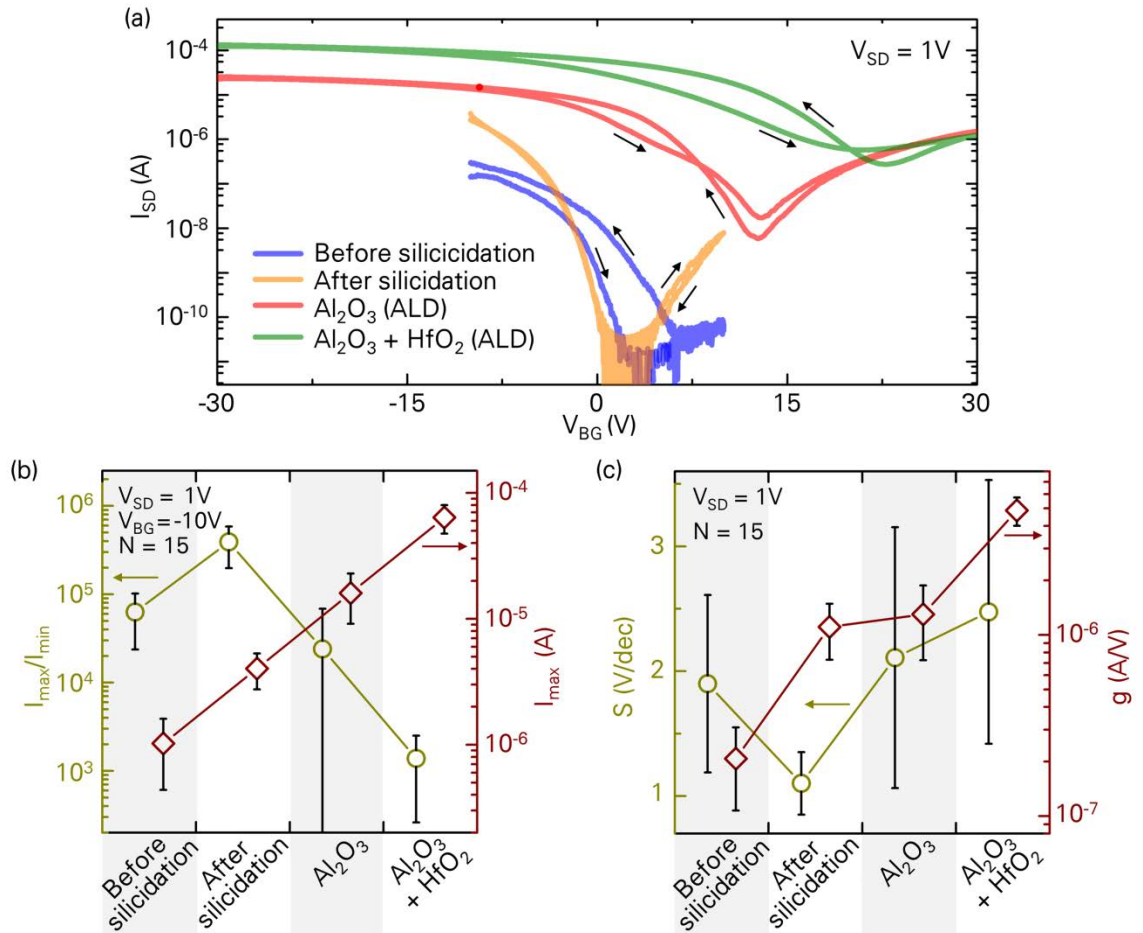
Fig. 4.8: Comparison of device characteristics at different fabrication stages in dry conditions. (a) Representative I_{SD}-V_G hystereses recorded at $V_{SD} = 1$ V. (b) Averaged maximum currents, I_{max}, and I_{max}/I_{min} ratios, and (c) averaged subthreshold swings, S, and transconductances, g, at $V_{BG} = -10$ V, $V_{SD} = 1$ V. The sample size is $N = 15$ devices per plotted point.

---

[1] On each applied chip, 1 out of 16 FETs does not function, either due to a short-circuit or due to an open circuit owing to a locally improper development of the photoresist during the lift-off-based contacting of the SiNWs, as described in section 4.2.3.

respective I_{SD}-V_{BG} hysteresis, measured at $V_{SD} = 1$ V. It must be noted, that in this case all I_{max} values are extracted at $V_{BG} = -10$ V. This is due to the fact that directly after the Ni deposition and after the silicidation, the devices are not characterized beyond $V_{BG} = \pm10$ V. At these stages, the devices show ambipolar behavior with pronounced minima around $V_{BG} \approx 3$ V, as depicted in Fig. 4.8a. Considering that in liquid gate measurements later on high liquid gate voltages, V_{LG}, are avoided to prevent a breakdown of the passivation layers (see section 4.3.2), at the first two fabrication stages using relatively narrow $V_{BG} = \pm10$ V is regarded sufficient for evaluating the devices. Unexpectedly, after depositing the passivation layers, the minima of the ambipolar curves shift to $V_{BG} > 10$ V so that the characterization interval must be extended to $V_{BG} = \pm30$ V. Yet, to enable a better comparison of all fabrication stages, the maximum currents displayed in Fig. 4.8b are determined at $V_{BG} = -10$ V. The transconductances and the subthreshold swings of the devices in Fig. 4.8c are derived from the *p*-branches of the backward gate voltage sweeps.

The representative transfer curves in Fig. 4.8a show that the silicidation process effectively reduces the hysteresis of the devices. In contrast, the deposition of the passivation layers broadens the hystereses again. Next to the above-mentioned shift of the curves towards higher V_{BG}, the passivation layers also induce a shift of the entire characteristics to higher I_{max}. This trend is confirmed by the average maximum currents of all devices depicted in Fig. 4.8b. However, the highest I_{max}/I_{min} ratios are achieved directly after the silicidation (see Fig. 4.8b), even though the freshly silicidized devices are not in saturation at $V_{BG} = -10$V. The relatively good switching behavior of the just silicidized devices is also visible in their subthreshold swings, which are the lowest among the tested chips (see Fig. 4.8c). The transconductances are highest in case of the passivated devices, because of the shift of their entire characteristics to high I_{SD} values. However, it must be noted, that the transconductances of the unpassivated devices do not peak within the applied $V_{BG} = \pm10$ V interval.

With regard to the error bars depicted in Fig. 4.8b,c, it is visible that the freshly silicidized devices possess the lowest device-to-device variability. In contrast, the Al_2O_3 passviation layer causes large variations in the individual transfer characteristics of the devices, which can be seen from the particularly broad error bars of the respective I_{max}/I_{min} ratios.

The data confirm the importance of the silicidation process for improving the switching behavior of the SB FETs, as introduced in section 4.2.3. (i) On one hand, the hystereses are reduced. Before the silicidation, the metal-semiconductor (Ni-Si) interfaces are located at the edges of the as-deposited Ni electrodes, in an area previously etched with HF. The native oxide subsequently formed in these areas is known to provide traps for charges causing the observed hysteresis. During silicidation, the metal-semiconductor ($NiSi_2$-Si) interface is shifted underneath the thermal oxide shell of the NWs. Consequently, the entire semiconducting sections of the NWs and the Schottky barriers are covered with high quality

oxide so that charge trapping and, thus, the hystereses are minimized. Furthermore, the optimized hystereses could be due to a reduction of dangling bonds during the forming gas anneal in the silicidation process. (ii) On the other hand, I_{max} are increased. Due to the intrusion of the silicide, the gate coupling at the contacts is enhanced leading to a strong thinning of the barriers in the *on*-state and, thus, high I_{max} as well as high I_{max}/I_{min} ratios.

The achieved average I_{max}/I_{min} current ratio of $\sim 3.9 \cdot 10^5$ is about two orders of magnitude lower than reported before.[199,229,230] As described in section 1.3.4, this can be attributed to a weak gate coupling, due to the very thick 1.5 µm thermal oxide of the utilized wafer substrates. Additionally, the fact, that the I_{SD} minima of all devices are at $V_{BG} > 0$ V, implies that undesired interface and trapped charges influence the device characteristics and potentially further weaken the gate coupling (see equation (1.9) in section 1.3.4). With regard to the direction of the curve shift, it must be prominently negative charges for which adsorbed water at the NW surface could be responsible.[119]

The transfer characteristics of the passivated devices clearly indicate that they are much more severely affected by interface and trapped charges. It is known that at the interface between SiO_2 and other dielectric layers interface charges can be formed.[237] Due to these charges, the devices are put into pronounced normally-*on* states with high *p*-currents at $V_{BG} = 0$ V. Furthermore, due to their screening effects, the charges strongly reduce the gate coupling resulting in the degraded S. The relatively large device-to-device variations suggest inhomogeneous charge distributions on the respective chips. Since the sole addition of an Al_2O_3 layer results in a smaller shift of the device characteristics than the addition of a stack of $Al_2O_3 + HfO_2$, it is concluded that any new layer of material brings in a new interface with possible interface charges or interface charge traps. Pulsed measurements with varying pulse widths may provide more detailed insights into the nature of the traps by inducing trapping and detrapping. Furthermore, it could be tested if forming gas treatments improve the devices characteristics.

Within this thesis, however, the focus is put on the device behavior in liquid gate measurements, as will be described in the following sections.

4.3.2 Liquid gate characteristics

In dry conditions, FETs can be used as gas sensors.[200,201] For a broad range of sensing applications, however, the respective devices need to be operated in liquid environments. Therefore, the devices are passivated *via* dielectric layers and mounted into a microfluidic the set-up for guiding liquids over the FET surfaces, as explained in section 4.2.4. An implemented Ag/AgCl reference electrode allows gating the system through the sample solution.

In the first part of this section, the liquid gate I_{SD}-V_{LG} characteristics of the fabricated devices are reported. Since the Ni electrodes of the SB FETs are often observed to degrade at liquid gate voltages beyond $V_{LG} = \pm0.5V$, probably due to an oxide degradation, the devices are characterized within the boundaries of $V_{LG} = \pm0.4V$.

In the second part of this section, an additional protective photoresist layer is used to broaden the possible liquid gate voltage range to $V_{LG} = \pm3$ V. The improved device characteristics are described.

4.3.2.1 Influence of the passivating dielectric layer

The behavior of the devices under liquid gate conditions is presented in Fig. 4.9. Representative I_{SD}-V_{LG} curves of two differently passivated bottom-up SB FET devices fabricated within this thesis are compared in Fig. 4.9a. The average values of I_{max}, I_{max}/I_{min} ratio, subthreshold swing and transconductance of the different types of devices are presented in Fig. 4.9b,c. Within the applied V_{LG} range both device are permanently in their *on*-states showing almost no hysteresis. Similarly to the back-gate results (see Fig. 4.8), the devices with $Al_2O_3+HfO_2$ passivation show almost one order of magnitude higher I_{max} levels than the devices with only Al_2O_3 passivation. For both, the Al_2O_3 and the $Al_2O_3+HfO_2$ covered chips, the average I_{max} levels are about one order of magnitude below the respective back-gate values which is attributed to the limited V_{LG} range. The data in Fig. 4.9a illustrate that the limited V_{LG} range does not include the threshold voltages, V_t, yielding for both device types only very low average I_{max}/I_{min} ratios.

However, despite that limited V_{LG} range far from V_t, for both device types, lower subthreshold swings and higher transconductances than in the back-gate measurements are
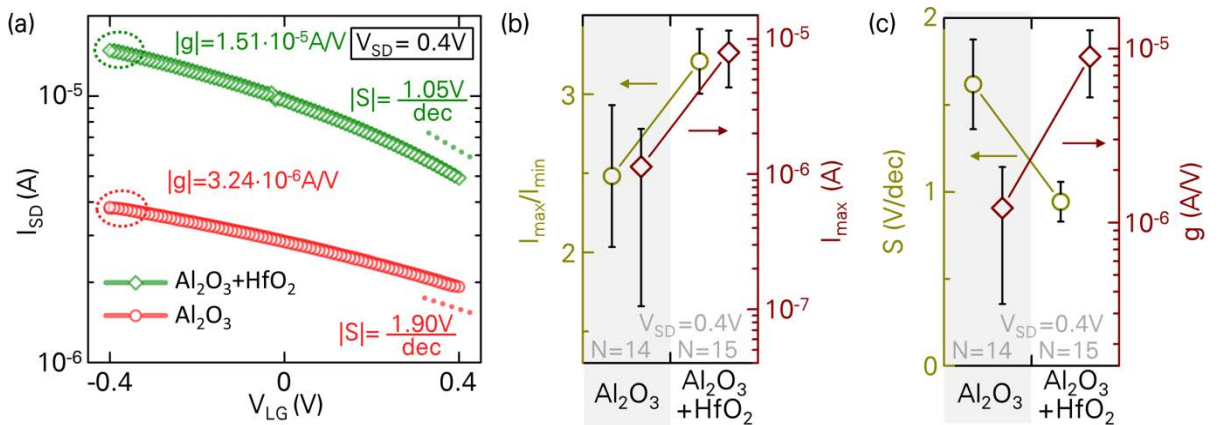
Fig. 4.9: Comparison of liquid gate characteristics of the bottom-up SiNW SB FETs fabricated within this thesis in dependence of the dielectric passivation layer, recorded at $V_{SD} = 0.4$ V. The liquid solution is DI water. (a) Representative I_{SD}-V_{LG} of the different types of devices (b) Averaged maximum currents, I_{max}, and I_{max}/I_{min} ratios, and (c) averaged subthreshold swings, S, and transconductances, g, at $V_{SD} = 0.4$ V. The sample sizes are $N = 14$ and $N = 15$ devices per plotted point, respectively, as indicated in the graphs.

achieved. Therefore, the data presented in Fig. 4.9 demonstrate an improved switching behavior when using the liquid gate, compared to the back-gate characteristics. On one hand, the modified switching behavior is attributed to the altered series of gate dielectrics. There is no more gating through the 1.5 µm thick thermal oxide of the supporting substrate. Instead, there are the maximum 24 nm thin oxides. And in addition to this value, the depletion width in the liquid, $i.\,e.$ the Debye screening, close to the oxide surface adds up as a series capacitor between V_{LG} and C_{Ox}. In DI water, as applied here, it is assumed to be maximum ~ 950 nm wide (see equation 1.10). On the other hand, there is an enhanced gate geometry, since the liquid gate resembles a gate structure close to a surround gate increasing the gate control. Altogether, this enhances the electrical characteristics significantly.

4.3.2.2 Device improvements with additional protective photoresist layer

As described above, the Ni electrodes of the bottom-up SB FETs are observed to degrade in liquid gate measurements beyond $V_{LG} = \pm 0.5$V. It is assumed that there is a degradation of the dielectrics at too high electric fields making the electrodes vulnerable to electrochemical attacks. In an experiment using another device with 20 nm Al_2O_3 passivation plus an additional protective photoresist layer, a much broader range of applicable V_{LG} is achieved.

In Fig. 4.10 the transfer characteristics of three devices are plotted. The red circles and the green diamonds correspond to the representative liquid gate I_{SD}-V_{LG} curves presented in Fig. 4.9 of devices passivated with a 20 nm Al_2O_3 layer or a stack of 20 nm Al_2O_3 and 4 nm HfO_2, respectively. Both curves are recorded at $V_{SD} = 0.4$ V using DI water as liquid solution. The device represented via blue squares is covered by an Al_2O_3 passivation layer and by an additional photoresist layer[2] covering the entire chip, including the interdigitated electrodes. Only on top of the SiNWs, there are opening windows in the photoresist layer. The window positions are schematically depicted in the red mask layout in Fig. 4.6. The openings provide direct contact between the liquid solution and the Al_2O_3 in the vicinity of the sensitive elements – the SiNWs and the Schottky barriers. As depicted in Fig. 4.10 the additional protective layer allows sweeping the liquid gate voltage in the range $V_{LG} = \pm 3$ V without any device degradation. The curve is recorded at $V_{SD} = 0.25$ V using a 10 mM phosphate buffer (PB) liquid solution with pH 7.1.

---

[2] During the experiments for a silane-based surface patterning, described in chapter 3, large difficulties occurred when the resist AZ5214e was applied in combination with APTES. In most cases the resist did not go off the substrate anymore when APTES was evaporated into the lithographically prepared patterns. The manufacturer of the AZ5214e confirmed that the resist crosslinks extraordinarily in the presence of amines, such as APTES. Exposing the resist to APTES vapor inside a desiccator at a vacuum of approx. 5 kPa (see chapter 3) makes it long-term solvent resistant. After 48 h in isopropanol no signs of dissolution are visible. After 48 h in actone the resist is considerably attacked, but not dissolved. Such stabilized photoresist layer is applied on the above-described device during the liquid gate measurements.

Within the increased V_{LG} range, the device is switched from its *on*-state into its off-state at V_{LG} = 3 V. This yields I_{max}/I_{min} = 1.54 · 10⁶, the highest I_{max}/I_{min} ratio determined within all presented experiments, close to I_{on}/I_{off} ratios of similar SiNW SB FETs reported before.[199,229,230] The subthreshold swing of $|S|$ = 0.18 V/dec is the lowest one determined within this work. A peak transconductance of $|g|$ = 1.79 · 10⁻⁵ A/V at V_G = 0.8 V is the highest one determined within this work. The *n*-branch of the actually ambipolar device is not reached within the applied V_G range. However, the data, including

Fig. 4.10: Transfer characteristics of three bottom-up SB FET devices measured *via* liquid gate. Red circles and green diamonds depict devices with plain Al₂O₃ or Al₂O₃+HfO₂ passivation layers, respectively, measured in DI water at V_{SD} = 0.4 V. Blue squares depict device with Al₂O₃ passivation layer and additional photoresist protection with opening windows on top of the SiNWs. Measured in 10 mM phosphate buffer (PB), at pH 7.1, at V_{SD} = 0.25 V. Additional resist passivation enables gate sweeps in-between V_G = ±3 V. At V_G ≈ 2.3 V a subthreshold swing of 0.18 V/dec is determined.

the almost nonexistent hysteresis, emphasize the significant improvement of the gate coupling under liquid gate conditions, compared to the back-gate measurements in section 4.3.1. Additionally, the utilization of a PB solution, instead of DI water, during the measurement, is expected to positively influence the switching behavior,[238] since the Debye screening is reduced to λ_D ≈ 1.5 nm.

The high transconductance is also attributed to the high *on*-current level of the tested device, despite the lower applied V_{SD} when characterizing the device with the additional photoresist layer. The differences in I_{SD} levels between the devices illustrates, that not only device-to-device but also chip-to-chip variations play an important role in the bottom-up assembly strategy applied within this chapter.

In summary, the above-described addition of a protective photoresist layer enables the operation of the SB FET devices in a broader range of V_{LG}. It makes the subthreshold regime of the devices accessible increasing the opportunities to find an optimum operation mode for maximum sensitivity, as described in the following section. However, due to delamination issues of the applied photoresist layer during assembling and disassembling the PDMS set-up, later sensing measurements are performed without additional protective layer in the boundaries of V_{LG} = ±0.4V. In this V_{LG} range the devices are mainly in the Ohmic mode showing an almost linear dependence of I_{SD} over V_{LG}.
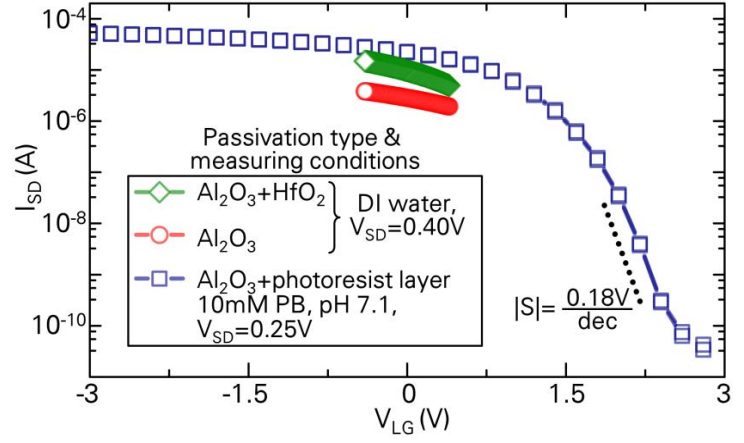
For future tests on improving the device characteristics by means of such protective photoresist layers, the utilization of a thin type of epoxy resist, such as SU-8 2000.5 is recommended, due to its high stability and excellent biocompatibility.[239]

4.3.2.3 Optimum device operation regime

In the literature, there are contradictory opinions about the most suitable measuring regime for obtaining optimum device sensitivities. There are reports describing that the highest signal-to-noise ratios (SNR) of the applied devices are obtained in the subthreshold regime,[206] or at the peak transconductance,[240] or in-between these values.[202] The optimum operation range must be determined for every type of device and measurement set-up separately. Due to the constraints given by the narrow window of applicable liquid gate voltages, no investigations on the optimum working regime for highest SNR are performed within this thesis. From the measurements presented in the previous section (section 4.3.2.2) it is assumed that the SB FETs fabricated within this thesis are operated close to their peak transconductance within the liquid gate voltage boundaries of $V_{LG} = \pm0.4$V.

4.3.3 pH and ion sensitivity

In the experiments described within this section, phosphate buffer (PB) solutions of different pH values and aqueous ammonium acetate (CH_3COONH_4) solutions of different ion concentrations are used as primary samples for investigating the sensing behavior of the fabricated SB FET-based sensors. At first (section 4.3.3.1) the applied measurement approach is explained. Then, distinctive features while preparing the measurements are described (section 4.3.3.2) before the pH and ion sensitivities of the devices are tested (section 4.3.3.3). Finally, the producibility of a true reference sensor[109,207,208] is investigated (section 4.3.3.4).

4.3.3.1 Measurement approach

As introduced in section 1.3.2, the sensing mechanism of FET-based sensors relies on a shift of the threshold voltage upon surface potential changes owing to the adhesion of chemical or biological species. In a first approximation, the shape of the I_{SD}-V_{LG} transfer characteristics of a sensor does not change during the measurement. The shift of the threshold voltage, ΔV_t, is considered equal to a plain shift of the I_{SD}-V_{LG} curve of the device. This is depicted schematically in Fig. 4.11. In the figure, the blue and the red dotted lines represent the I_{SD}-V_{LG} transfer characteristics of a device at the time t_1 and t_n in an analyte solution with the analyte concentration c_1 and c_n, respectively. Based on this schematic, there are various measurement approaches for an ISFET-based detection of analytes.

For monitoring the respective ΔV_t, Bergveld et al.[98] propose the application of operational amplifier-based source/drain follower circuits. In such circuitries, an output voltage is generated the changes of which resemble ΔV_t of the implemented ISFET at constant I_{SD} and
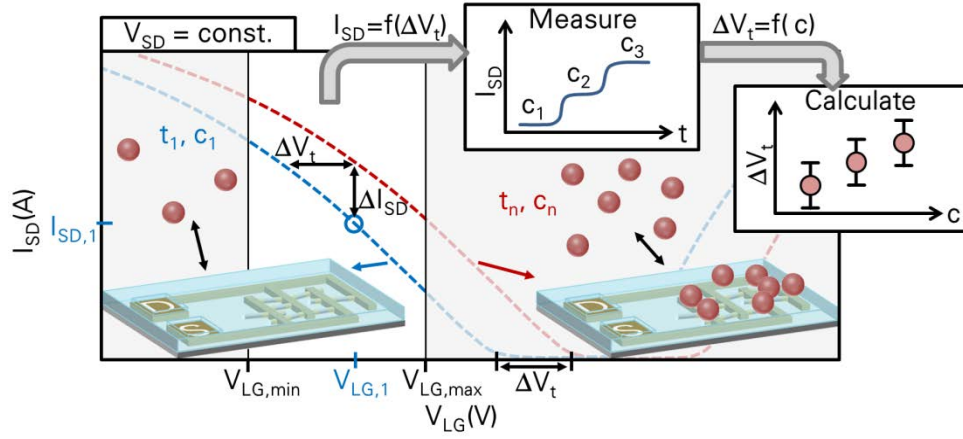
Fig. 4.11: Schematic illustration of the applied measurement approach. The blue and the red dotted lines depict I_{SD}-V_G transfer curves of the schematically shown device in its two states, at the times t_1 and t_n in an analyte solution with the concentrations c_1 and c_n, respectively. During the sensing experiment, the shift of the threshold voltage, ΔV_t, or the shift of the surface potential, respectively, is monitored indirectly by observing I_{SD} at constant $V_{LG} = V_{LG,1}$. At the beginning, at t_1, a section of the entire I_{SD}-V_G curve of the device is recorded within the boundaries $V_{LG,min}$ and $V_{LG,max}$, i. e. the gate voltage constraints explained in section 4.3.2.3. Based on the initial I_{SD}-V_{LG} curve the I_{SD} changes are used to determine ΔV_t over time and to correlate ΔV_t with the applied analyte concentrations c_1, c_2, .., c_n. The starting point of the sensing experiment ($V_{G,1}$,$I_{SD,1}$) is chosen with regard to the device operation constraints summarized in section 4.3.2.3.

V_{LG} levels. However, such set-up is not available within this thesis. Another approach for observing ΔV_t would be the implementation of a software-based feedback loop in the measurement system which keeps I_{SD} constant while adjusting and recording ΔV_{LG} at constant V_{SD}.[223] Furthermore, Zörgiebel et al.[28] developed a measuring approach of permanently sweeping the gate voltage and recording the entire I_{SD}-V_{LG} characteristics at each point of time. This enables a comprehensive post-processing of the experimental data with the possibility to subsequently extract two or three dimensional maps of I_{SD} versus V_{LG} and t, and also the time dependence of specific values such as the transconductance or the subthreshold swing, however, at the expense of a valuable time resolution during the experiments (see also section 4.3.4.2).

In the measurements described within this section, a simpler measurement approach with very high time resolution is used.[29] With regard to the schematic in Fig. 4.11, at the beginning of a measurement, at $t = t_1$, when the FET is in contact with a sample solution of an analyte concentration c_1, the I_{SD}-V_{LG} curve of the device is recorded within the boundaries $V_{LG,min}$ and $V_{LG,max}$, i. e. the above-explained gate voltage constraints of the utilized chips (see section 4.3.2.3). During the sensing experiments the changes of I_{SD} are monitored at constant V_{SD} and constant $V_{LG} = V_{LG,1}$. Based on the initial I_{SD}-V_{LG} curve, via interpolation, the I_{SD} changes are used to determine ΔV_t over time and to correlate ΔV_t with the applied analyte concentrations. The starting point of the sensing experiment ($V_{G,1}$, $I_{SD,1}$) is chosen

with regard to the chip operation constraints summarized in section 4.3.2.3, as further described in the following section.

It has to be noted that any alterations in the transfer characteristics not being related to a surface potential change, such as device degradation or hysteresis effects, are not recognized when only I_{SD} is recorded during the sensing experiment. However, in case of pH and ion concentration sensing, no significant transfer curve deformations are expected.

4.3.3.2 Measurement settings

Sample solutions

As sample solutions 100 mM phosphate buffers with pH 6.1, pH 7.1 and pH 8.1 are prepared for measuring the pH sensitivity. For ion sensitivity measurements 5 µM, 500 µM and 50 mM ammonium acetate (CH_3COONH_4) solutions are used. CH_3COONH_4 dissociates into CH_3COO^- and NH_4^+ ions which are of similar acid or base strength, respectively, as indicated by $pK_b = 9.25$ (CH_3COO^-) and $pK_a = 9.25$ (NH_4^+). Thus, CH_3COONH_4 solutions are expected to be of neutral pH with minimum pH variations so that any visible sensor signals are attributed exclusively to the change of the ion concentration. The pH values of the solutions range between pH 6.4 (5 µM CH_3COONH_4) and pH 6.7 (50 mM CH_3COONH_4).

Fluidic set-up

The devices are assembled in the fluidic set-up as described in section 4.2.4. To minimize interferences on the experiments by air bubbles, prior to the measurements all sample solutions, then ethanol and finally DI water are drawn once through entire the fluidic system. Particularly the eight position selection valve requires cautious handling. Its switching movements in some cases induce the formation of bubbles. The syringe pump is set to draw the solutions through the channel system at 100 µl/min flow ratio. For each tested device, the respective initial I_{SD}-V_{LG} curve (see below) is recorded in streaming DI water. During the sensing measurements, the eight position selection valve is used for switching the sample solutions. Each sensing series comprises three measurement points starting with the lowest pH or ion concentration and finishing with the highest pH or ion concentration, respectively.

FET settings

At the beginning of each experiment, the I_{SD}-V_{LG} curves of the respective devices are measured in DI water at $V_{SD} = 0.4$ V. The applied V_{LG} range is $V_{LG} = \pm 0.4$ V. During the actual sensing experiments, while guiding different sample solutions over the FET surfaces, I_{SD} is recorded at constant $V_{SD} = 0.4$ V, and constant V_{LG}. Finally, ΔV_t is calculated from the measured I_{SD} values, based on the backward branch of the initially recorded I_{SD}-V_{LG} curves,
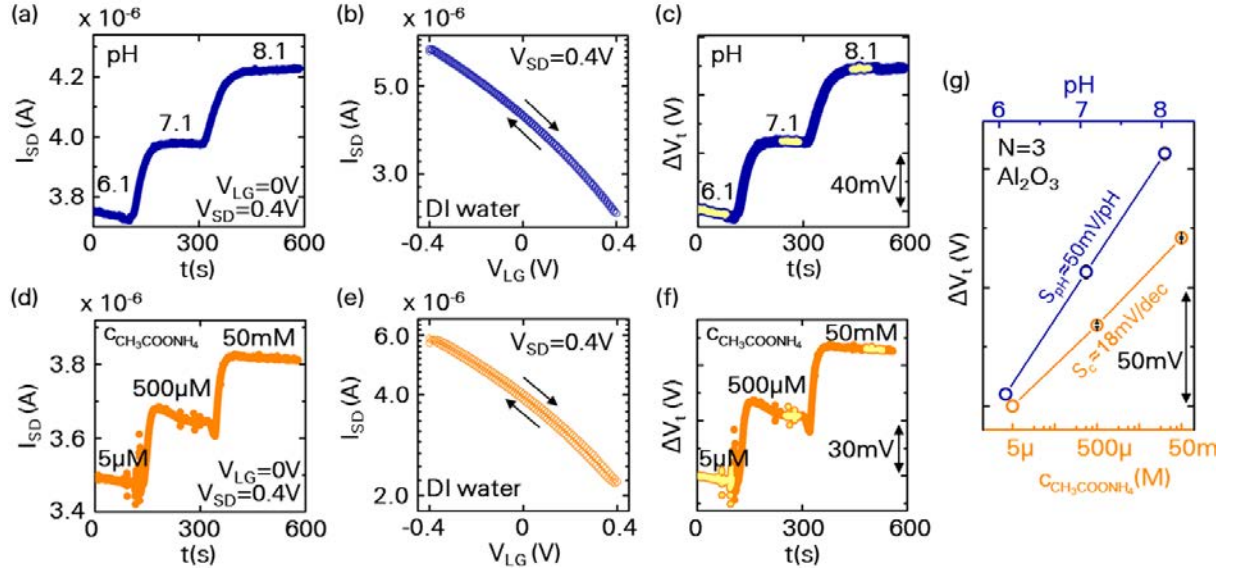
Fig. 4.12: Determination of the pH and ion sensitivities of the devices, demonstrated using the example of one bottom-up SiNW SB FET with Al$_2$O$_3$ surface dielectric layer, with (a) and (d) showing the recorded time-dependent I_{SD} curves while guiding PB buffers or salt solutions with the indicated pH or ion concentrations over the sensor surface at V_{SD} = 0.4 V, V_{LG} = 0 V and (b) and (e) showing the initial I_{SD}-V_{LG} hystereses of the device, recorded at V_{SD} = 0.4 V in DI water, before the pH and ion sensing experiments, respectively. (c) and (f) show the respective determined ΔV_t curves. The yellow highlighted sections in the respective plateaus of the curves are used for determining the pH and ion sensitivities of the device. In (g), the average pH and ion sensitivities of N = 3 Al$_2$O$_3$ passivated devices are plotted.

as described in section 4.3.3.1. Commonly, during the measurements, V_{LG} is set to V_{LG} = 0 V, *i. e.* in the middle of the applicable V_{LG} range (see also section 4.3.2.3).

4.3.3.3 pH and ion sensitivities of bare devices

Fig. 4.12 shows exemplary results and intermediate results of the above-described experimental procedure for determining the pH and ion sensitivities of one bottom-up SiNW SB FET with Al$_2$O$_3$ surface dielectric. Fig. 4.12a & d present the time-dependent I_{SD} curves while guiding analyte solutions with varying pH or varying CH$_3$COONH$_4$ concentrations over the sensor surface. After the measurements, using the I_{SD}-V_{LG} curves in Fig. 4.12b & e, the time-dependent ΔV_t curves in Fig. 4.12c & f are derived. Additionally, the average pH and ion sensitivities of three tested Al$_2$O$_3$ passivated devices are summarized in Fig. 4.12g. The corresponding ΔV_t values are derived from the yellow highlighted sections in the time-dependent ΔV_t plot (Fig. 4.12c,f), where the ΔV_t curves stabilize in plateaus. The Al$_2$O$_3$ surface is determined to provide a pH sensitivity of S_{pH} ≈ 50 mV/pH and a CH$_3$COONH$_4$ ion sensitivity of S_c ≈ 18 mV/dec.

For the HfO$_2$ surface, a pH sensitivity of S_{pH} ≈ 54 mV/pH and an ion sensitivity of S_c ≈ 23 mV/dec is determined. The pH and ion sensitivities of the different surfaces are summarized in Fig. 4.13.

The pH sensitivity of the Al_2O_3 surface is slightly lower than the 57 mV/pH and the 52 mV/pH reported by Chen et al.[29] and Abe et al.,[241] respectively. Also the measured pH sensitivity for the HfO_2 surface is below the literature values of around 59 mV/pH.[105]

These deviations of pH sensitivities are assumed to originate from contaminations at the sensor surfaces. As opposed to Chen et al.[29] who treat their devices with an

Fig. 4.13: Summary of the determined average sensitivities for (a) pH and (b) CH_3COONH_4 ion concentrations with respect to the dielectric material on top of the sensor surface. In each case the sample size is $N = 3$.

UV/ozone cleaning step at the beginning of every sensitivity measurement to remove any organic impurities from the surface, within this thesis there is no UV/ozone cleaner available. An alternative removal of possible contaminations via a plasma cleaning step prior to the measurements is not feasible, as it would lead to an irreversible bonding of the PDMS-based fluidic channel to the chip surface (see also section 1.2 and section 2.1). Furthermore, a plasma cleaning step would make the surface highly reactive and, thus, prone to fast recontamination.[242] In case of a functionalized sensor, an UV/ozone or plasma cleaning would destroy the organic surface modification.

The ion sensitivities of the devices in CH_3COONH_4 solutions depicted in Fig. 4.13b are comparable to other ion sensitivity observations in the literature. In a work of Bergveld, ISFETs with Al_2O_3 dielectrics exhibit increasing sensitivity towards Na^+ and Cl^- ions with increasing NaCl concentrations in the range of $c_{NaCl} = 1$ mM .. 1 M, up to a maximum ion sensitivity of 6 mV/dec.[98] In a work of Tarasov et al. both HfO_2 and Al_2O_3 dielectrics are found to provide Cl^- ion sensitivities of up to 60 mV/dec when using buffered KCl solutions with different Cl^- concentrations above $c_{Cl^-} = 10$ mM.[108] Since the compositions of the applied buffer solutions in both studies differ, it is not possible to directly compare the determined ion sensitivity values.[98,108] However, the reported ion sensitivities are in the same order of magnitude as the ones recorded within this work for aqueous CH_3COONH_4 solutions. Furthermore, there is agreement between the previous studies and the results in Fig. 4.13b that HfO_2 and Al_2O_3 yield similar ion sensitivities.

With regard to the surface complexation model described by Tarasov et al.,[108] CH_3COOH^- anions are expected to partially replace previously adsorbed protons and form chemical complexes with the surface hydroxyl groups of the dielectrics while NH_4^+ cations remain further away from the surface. This induces the shift of the threshold voltage to more positive values.
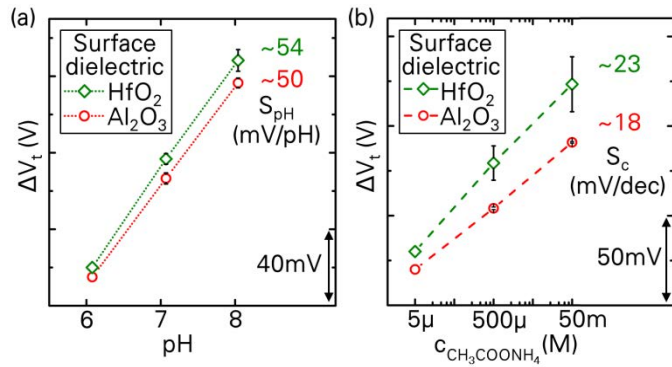
In the above-described studies, at concentrations below c_{NaCl} = 1 mM and c_{Cl^-} = 10 mM, respectively, the devices show no ion sensitivity.[98,108] Such behavior is also predicted by the theoretical models introduced in section 1.3.2.[101–104,108] Strikingly, the measurements within this thesis show distinct ion sensitivities at three to four orders of magnitude lower concentrations. In future measurements, the ion sensitivities at CH_3COONH_4 concentrations below $c_{CH3COONH4}$ = 5 µM should be investigated to find the threshold CH_3COONH_4 concentration below which no more ion sensitivity is observed. This way, a better understanding of the interplay between the ions and the surface may be obtained.
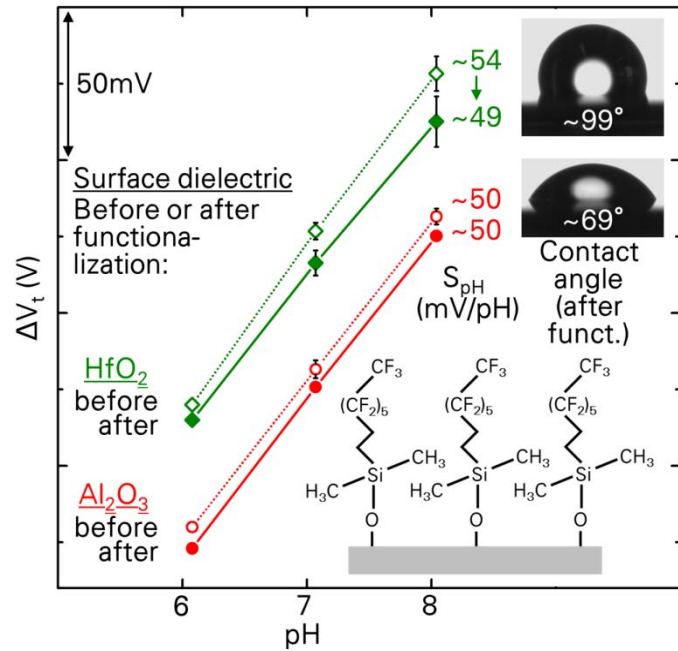
Fig. 4.14: Summary of the determined average pH sensitivities of the devices before (open diamonds or circles) and after the functionalization with HFDMCS (filled diamonds or circles). On HfO_2 covered devices the functionalization results in hydrophobic surfaces with contact angles of ~99°. On Al_2O_3 covered devices the contact angle is ~69°.

4.3.3.4 Surface functionalization and sensitivity changes

As introduced in section 4.1, it is highly desirable to modify the sensor devices in such way that they become insensitive to chemical changes at their surface while maintaining their responsivity to the liquid gate. Such devices could be used as true reference sensors in differential set-ups where they are combined with the actual sensing ISFETs with similar electrical characteristics, to minimize the influences of drift or temperature on the measurements.[106,109,207,208] In a publication by Tarasov *et al.*, SiNW-based ISFETs are converted into true reference sensors by means of a surface functionalization using octadecyldimethylmethoxysilane (ODMMS).[109] They observe a reduction of the pH sensitivity of their devices by two orders of magnitude and explain the effect by a chemical passivation of the -OH groups. In previous surface functionalization attempts with short-chained organo modifiers, the respective FET-based sensors show a residual pH sensitivity of at least S_{pH} > 10 mV/pH.[29,103,106] Instead, long-chained silane molecules, such as ODMMS,[109] docosyldimethyl(dimethylamino)-silane [243] or (heptadecafluoro-1,1,2,2-tetrahydrodecyl)trimethoxysilane [207,208] reduce the pH sensitivity more efficiently to values below $S_{pH} \leq 8$ mV/pH.

Within this thesis the applicability of the silane (heptadecafluoro-1,1,2,2-tetrahydrodecyl)dimethylchlorosilane (HFDMCS) for fabricating true reference sensors is tested. The silane is similar to the previously applied (heptadecafluoro-1,1,2,2-tetrahydrodecyl)trimethoxysilane,[207,208] however, with only one instead of three leaving groups to prevent the formation of multilayers (see inset Fig. 4.14 and section 1.4.2.3). The silane is deposited onto the sensor surfaces for up to seven days (7 d) [109] *via* the desiccator-assisted approach described in section 3.3.1.

Fig. 4.14 summarizes the pH sensitivities of the devices covered with different dielectric layers, before and after the functionalization with HFDMCS. Additionally, the wettability of the surfaces after their functionalization is depicted. In case of Al_2O_3 covered surfaces, the functionalization yields contact angles of ~ 69°. The pH sensitivity remains at $S_{pH} \approx 50$ mV/pH. The HfO_2-covered devices show contact angles of ~ 99° and their pH sensitivity decreases by 9.2 % to $S_{pH} \approx 49$ mV/pH.

With respect to the site-binding model introduced in section 1.3.2, Bousse *et al.* calculated that the pH sensitivity near the point of zero charge, pH_{pzc}, of a device surface is given by [103,104]

$$S_{pH} = \frac{59.5\,\beta}{(\beta+1)}\ \frac{mV}{pH} \qquad (4.1)$$

with the sensitivity parameter *β* being

$$\beta = \frac{2\,q^2\,N_S\left(\frac{Ka_2}{Ka_1}\right)^{1/2}}{C_H\,k\,T} \qquad (4.2)$$

In equation (4.2), q is the elementary charge, N_S is the number of binding sites or -OH groups per surface area, respectively, Ka_1 and Ka_2 are the dissociation constants for protonation and deprotonation of the -OH groups, respectively, C_H is the Helmholtz layer capacitance of the electrochemical double layer on the sensor surface, k the Boltzmann constant and T the absolute temperature.[103,104] The points of zero charge of both surface types, $pH_{pzc,Al2O3} = 8.7$ for Al_2O_3 [244] and $pH_{pzc,HfO2} = 7.6$ for HfO_2,[245] are within or in proximity to the pH-range of the buffer solutions utilized for determining the pH sensitivity. Using the commonly applied values $Ka_1 = Ka_2 = 10^{-7}$ and $C_H = 20$ µF/cm²,[103,104,109] equations (4.1) and (4.2) allow estimating N_S of both surfaces to $N_{S,Al2O3} \approx 9 \cdot 10^{12}$ cm^{-2} and $N_{S,HfO2} \approx 1.75 \cdot 10^{13}$ cm^{-2}, respectively, in case of the non-functionalized devices. After the functionalization with HFDMCS, N_S of the HfO_2 covered device reduces to $N_{S,HfO2} \approx 8 \cdot 10^{12}$ cm^{-2}, *i. e.* more than half of the initial binding sites or -OH groups on the surface are chemically passivated by the silane. To reduce the pH sensitivity to values below $S_{pH} \leq 3$ mV/pH, $N_{S,HfO2}$ must be further decreased by two orders of magnitude.

Other than the contact angle measurements introduced in section 3.2.1, the pH sensitivities of the devices reveal more clearly the deficient quality of the HFDMCS silane layers. Since long functionalization times of up to 7d do not enhance the chemical passivation of the devices, the surface activation procedure before the silane deposition is considered to be the critical step of the overall process. From the relatively low amounts of chemically passivated -OH groups, compared to above-described works,[109,207,208,243] it is evident that the initial surface treatment must be further optimized. The functionalization results may be improved (i) by a longer plasma treatment, (ii) by using a pure oxygen plasma instead of an air plasma, or (iii) by replacing the plasma treatment with a UV/ozone-based activation step.[29,109] Additionally, it is expected that the silane deposition will be improved by reducing the transportation time after the plasma treatment, when carrying the sample from the plasma cleaner to the desiccator set-up. The longer a just plasma treated sample is exposed to ambient air, the more it interacts with present moisture and contaminants, so that its surface gradually reverts back to a non-activated state.[242] Within this work, about 5 min elapse between switching off the plasma cleaner and switching on the vacuum pump of the desiccator set-up for the silane deposition.

In case of the Al_2O_3-covered devices, the surface functionalization does not yield the desired results, neither with respect to the contact angles nor with respect to the pH sensitivity. The reasons for that are not yet known. However, regarding the ALD processes, it is noticeable that the Al_2O_3 films are deposited *via* an ozone-based procedure and the HfO_2 layers are formed *via* a water-based procedure. It remains to be tested, if a water-based ALD deposition of Al_2O_3 dielectrics yields different surface properties for an improved surface functionalization outcome *via* the above-described silane deposition approach.

In the future, for a better general understanding of the device functionalization behavior, X-ray photoelectron spectroscopy (XPS) is considered an appropriate tool for obtaining more detailed information about the surface chemistry. With regard to the HFDMCS functionalization results in this section, all BioFET measurements in the following section (section 4.3.4) are performed on HfO_2-covered FETs to avoid any complications during the required TESPSA silane deposition.

4.3.4 TESPSA-based BioFET application

Within this section, the TESPSA-based receptor immobilization strategy presented in chapter 3 is applied to the fabricated HfO_2-covered bottom-up SiNW FETs for BioFET measurements. In the first part (section 4.3.4.1), important adjustments on the fluidic set-up and the compositions of the analyte solutions are introduced. Section 4.3.4.2 points out the differences of the data acquisition method within this section compared to previous measurements in section 4.3.3. In the last part (section 4.3.4.3), the sensitivity and specificity of the sensors for target analytes before and after the TESPSA-based immobilization of receptor molecules on top of the sensor surface are investigated.

4.3.4.1 Fluidic set-up and analyte solutions

When guiding analyte solutions over the surface of a sensor with immobilized receptor molecules, there are three processes occurring in parallel which influence the sensor signal. (i) Association of analytes to the receptor molecules to form analyte-receptor complexes (see section 1.4.1), (ii) dissociation of the complexes into free receptor structures and free analyte molecules in solution, (iii) disturbance and subsequent equilibration of the electrochemical double layer at the device-solution interface with each analyte binding and unbinding event.

Fluidic set-up

From initial measurements of receptor-analyte interactions on the sensor surfaces using the microfluidic set-up depicted in Fig. 4.7, it is recognized that reducing the flow rate of the liquid to below 2 µl/min or stopping the flow, leads to the formation of air bubbles inside the channel system. In a continuous flow regime with at least 2 µl/min flow rate, the sensor signal is observed to be not sufficiently stable for conclusively detecting the applied analytes (data not shown). Therefore, the fluidic system is changed to a set-up as schematically depicted in Fig. 4.15a. Instead of a syringe pump-based flow of the analyte solutions, they are guided over the sensor surface *via* capillary forces. The solutions are added dropwise at one opening of the PDMS channel system by means of a pipette. At the second opening of the PDMS stamp, excess sample solution is soaked up using a tissue. An Ag/AgCl reference

Fig. 4.15: Modification of experimental procedure, compared to previous arrangements in Fig. 4.7b and Fig. 3.3c, respectively. (a) In the fluidic set-up the sample solution is guided over the sensor surface *via* capillary forces after dropwise addition of excess or new sample solution at one opening of the PDMS channel system using a pipette. At the second opening of the PDMS stamp, excess sample solution is soaked up *via* a tissue. The Ag/AgCl reference electrode is dipped into a 3 M KCl solution saturated with AgCl inside a housing (see also section 4.2.4) which is incorporated into the PDMS set-up and which separates the sample solution from the internal 3 M KCl solution *via* a ceramic frit. (b) Besides the red and the green analytes, *i. e.* IgG$_{Target\_green}$ and IgG$_{Control\_red}$, introduced in section 3.2.3, an additional third analyte is used within the BioFET experiments in this section – an unlabeled peptide, schematically depicted as blue wavy element, which is expected to be repelled by the IgG$_{Receptor}$ immobilized on the sensor surface.

electrode is used for liquid gating the FETs during measurements. The electrode is dipped into a 3 M KCl internal filling solution, saturated with AgCl, of a modified version of the housing described in section 4.2.4 (Microelectrodes, Inc., USA) the tubing connectors of which are entirely removed. The housing is incorporated straight into the PDMS set-up so that the ceramic frit with the internal 3 M KCl solution on one side is in direct contact with the sample solution on the other side.

With the described built-up, a continuous sample flow is not possible. Instead, the flow is stopped after each liquid exchange. For replacing one sample solution with another, three cycles of adding 30 .. 40 µl new solution *via* a pipette and soaking the liquid through the ~ 50 µl large PDMS channel *via* a tissue are performed. Due to the sudden acceleration of the liquid in such events, a fourth sensor signal-influencing effect comes into play. (iv) The ions forming the electrochemical double layer at the device-solution interface are additionally disarranged by the high flow velocity changes.[246] The influence of flow velocity changes on the surface potential increases with decreasing ion concentrations.[246]

Buffer and analyte solutions

As explained above, within this section the receptor immobilization strategy presented in chapter 3 is adapted to the FET-based sensors. TESPSA is applied as linker molecule for the covalent attachment of the same $IgG_{Receptor}$ (see Tab. 3.1), based on the same protocol as before. The same IgG_{Target_green} and $IgG_{Control\_red}$ and one additional unlabelled peptide are utilized as analytes (see Fig. 4.15b). The additional peptide is a nine-amino acid synthetic peptide from human influenza hemagglutinin (HA) which is commonly used in epitope-tagging applications (HA peptide, Roche Diagnostics GmbH, Germany). The HA peptide is expected to show no specific interaction with the $IgG_{Receptor}$.

In consideration of the height of antibodies of about 10 nm,[143] analyte solutions with low ion concentrations are prepared. 300 µM sodium hydrogen phosphate (Na_2HPO_4) solution and 300 µM sodium dihydrogen phosphate (NaH_2PO_4) solution are mixed to form a 300 µM phosphate buffer (PB) solution with pH 7.4. Subsequently, proportions of commercial standard phosphate buffer saline (PBS, pH 7.4, VWR International, USA) are added. Buffers for Debye screening lengths (see section 1.4.2) of ~ 10 nM and ~ 7.5 nM are adjusted by preparing 300 µM PB with 0.002 x PBS and 300 µM PB with 0.005 x PBS, respectively.

The addition of PBS to the buffer system is necessary, because the analytes are delivered in 1 x PBS solutions. IgG stock solutions are diluted 1:500 or 1:200 with PBS-free 300 µM PB, resulting in analyte solutions with maximum analyte concentrations of 7 nM and 18 nM, respectively. Subsequently, solutions of lower analyte concentration are prepared using the respective PBS containing buffers. Maximum concentrations of the HA peptide in the analyte solutions are 9 nM and 22 nM, respectively. Additionally, for reducing unspecific interactions between analytes and surface, 0.05 vol.% Tween20 are added to all solutions.[247]

4.3.4.2   Data acquisition and evaluation

In contrast to the measurement approach presented in section 4.3.3.1, within this section the entire transfer characteristics of the devices are monitored at each point of time of all sensing experiments by continuously sweeping V_{LG} and recording I_{SD}. Commonly, a sweeping cycle starts at $V_{LG} = 0$ V going to $V_{LG} = 0.4$ V, then to $V_{LG} = -0.4$ V and finally back to $V_{LG} = 0$ V. One cycle requires 3 .. 5 s sweeping time.

In the post-processing of the recorded data, the required V_{LG} for a fixed I_{SD} level are determined. The inset in Fig. 4.16 exemplarily depicts the transfer characteristic of a sensor device with immobilized IgG$_{Receptor}$ in the presence of a pure buffer solution (300 µM PB with 0.002 x PBS). Throughout the experiment, analyte solutions with increasing IgG$_{Target\_green}$ concentrations are guided over the surface. The shift of the transfer characteristics of the device at a fixed I_{SD}

Fig. 4.16: Exemplary illustration of recorded transfer curves in case of a sensor device functionalized with IgG$_{Receptor}$ in the presence of 300 µM PB solution with 0.002 x PBS containing varying concentrations of IgG$_{Target\_green}$. The inset shows a full hysteresis at 0 nM analyte concentration, the main graph sections of the upward branches ($V_{LG} = +0.4$ V → -0.4 V) of the hystereses at 0 nM, 5 nM and 7 nM IgG$_{Target\_green}$ concentration. The shift of the transfer characteristics, which is considered equal to ΔV_t, is monitored at an as low as possible selected fixed I_{SD} level of $I_{SD} = 1.9$ µA.

value of 1.9 µA is considered equal to the shift of the threshold voltage, ΔV_t, or the negative of the shift of the surface potential of the sensor (see equation 1.6), respectively. For all measurements presented in the following section (section 4.3.4.3), fixed I_{SD} values close to the corresponding lowest measured I_{SD} are selected for monitoring ΔV_t. The lower the applied I_{SD}, the closer is the device to its subthreshold regime, which is reported to be the regime with highest signal-to-noise ratio for sensing applications in other publications.[206] Of the recorded hystereses, only the upward branches ($V_{LG} = +0.4$ V → -0.4 V) are taken into account for evaluating ΔV_t.

The main graph in Fig. 4.16 depicts sections of the upward branches of the hystereses recorded with the device at analyte concentrations of 0 nM, 5 nM and 7 nM. It is visible that the curves shift to lower values. The following section (section 4.3.4.3) describes the time dependent development of ΔV_t while guiding buffer solutions with different analytes of varying concentrations over the sensor surface. At each stage of the experiments the analyte solutions are allowed to incubate at room temperature for ~ 30 min.[127]
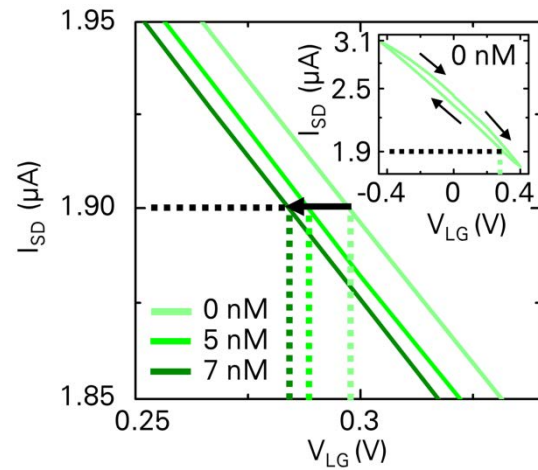
4.3.4.3 Sensor sensitivity and specificity for target analytes

Fig. 4.17a shows the time dependent behavior of ΔV_t of a sensor functionalized with $IgG_{Receptor}$ in the presence of 300 µM PB with 0.002 x PBS containing different analytes at varying concentrations. Every time an analyte solution is replaced by a new one, the ΔV_t values show distinct jumps which are primarily attributed to disturbances of the electrochemical double layer in the course of the sudden acceleration of the liquid on the sensor surface (see also section 4.3.4.1). Subsequently, while incubating the surface with the new analyte solution, the association and dissociation of analytes influence the reconstitution of the electrochemical double layer at the device-solution interface. After ~ 30 min incubation time, the analyte molecules in solution and the receptor-analyte complex and, thus, the electrochemical double layer are considered to be in equilibrium.[127] The sections of the time dependent ΔV_t curves (Fig. 4.17a) highlighted with blue, red or green color, shortly before introducing the next analyte solution, are utilized for determining average ΔV_t values assigned to the respective analyte and analyte concentrations. Fig. 4.17b depicts the dependence of ΔV_t on the concentration of the different analytes.
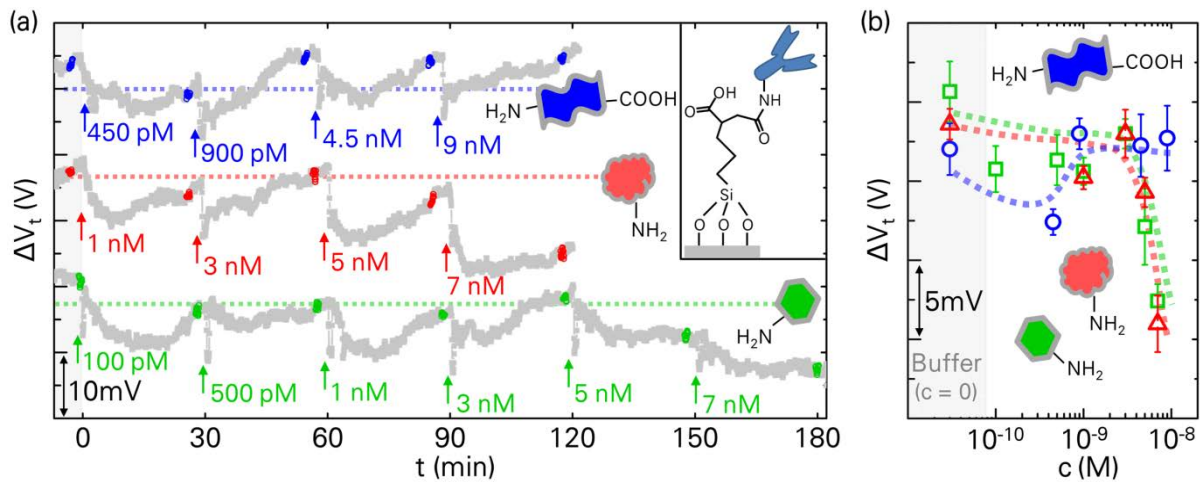

Fig. 4.17: ΔV_t response of one device functionalized with $IgG_{Receptor}$ during incubation of 300 µM PB solutions with **0.002 x PBS** containing HA peptide, $IgG_{Control\_red}$ or IgG_{Target_green} as analytes at varying concentrations. (a) Time dependent sensor signal. Before $t = 0$ min (time segment with light gray background), pure buffer is applied on the sensor. Starting from $t = 0$ min, solutions with gradually increasing analyte concentrations are incubated on the device. Arrows and adjacent references indicate when the analytes are added at the respective concentrations. The upper curve with blue indicators, the middle curve with red indicators and the lower curve with green indicators are related to the addition of HA peptide, $IgG_{Control\_red}$ and IgG_{Target_green}, respectively. The respectively colored dotted lines are guides to the eye to facilitate the recognition of ΔV_t changes. (b) Plot of ΔV_t over analyte concentration. Blue circles, red triangles and green squares correspond to HA peptide, $IgG_{Control\_red}$ and IgG_{Target_green}, respectively. Data points and error bars are determined from the time dependent ΔV_t values highlighted in the curves in (a), shortly before changing the analyte concentrations. Data points in the section having a light gray colored background in (b) correspond to pure buffer solutions without analytes. Dotted lines in (b) are guides to the eye.

From the graphs in Fig. 4.17, it is visible that there is no effective change of the sensor signal upon adding increasing amounts of HA peptide to the sample solutions (data highlighted in blue color). Depicted as blue circles in Fig. 4.17b, after a dip of ~ - 5 mV at $c_{HA\ peptide}$ = 450 pM, the HA peptide-related ΔV_t values recover at higher concentrations. Thus, HA peptide is regarded to exhibit no unspecific interaction with the functionalized surface.

The sensor signal in the presence of the specific antigen IgG$_{Target\_green}$ (data highlighted in green color, green squares in Fig. 4.17b) remains almost constant up to 3 nM analyte concentration. At $c_{IgG\_Target\_green}$ = 5 nM and above a distinct decrease of ΔV_t is observed. At $c_{IgG\_Target\_green}$ = 7 nM, a difference of ~ - 10 mV compared to the initial ΔV_t level is reached. Investigating the device behavior at analyte concentrations beyond 7 nM is not possible within this experimental arrangement. As explained in section 4.3.4.1, this would imply a change of the ionic composition of the sample solution which would affect the Debye screening length so that further ΔV_t changes were not exclusively reducible to analyte concentration differences.

In case of the nonspecific IgG$_{Control\_red}$ (data highlighted in red color, red triangles in Fig. 4.17b), the sensor shows a similar behavior as in case of the IgG$_{Target\_green}$. The fluorescence microscopy investigations in Fig. 3.6 in section 3.3.2 indicate a minor unspecific adsorption of IgG$_{Control\_red}$ to the immobilized receptor when using a 1 x PBS-based analyte solution with an ionic strength of I = 175 mM. In the literature, it is observed that the specificity of antibodies is reduced with decreasing ionic strength of the applied buffer.[127] Thus, in case of the low ionic strength solutions utilized within this section, with I = 1 mM, IgG$_{Control\_red}$ is assumed to exhibit a much stronger unspecific attachment to the surface, so that the signals of IgG$_{Target\_green}$ and IgG$_{Control\_red}$ are not distinguishable within the monitored analyte concentration range.

Since the transfer curve shifts to lower values with adsorption of increasing amounts of IgG, the molecules are concluded to be positively charged. The isoelectric point of the antibodies is not known. Commonly, polyclonal antibodies, as applied within this thesis, have no set isoelectric point.[248] For the HA peptide a theoretical isoelectric point of 5.98 is determined.[249] Thus, in the utilized buffer of pH 7.4, the molecules will possess a negative net charge. Consequently, in the event of an unspecific adsorption of HA peptide, an increase in the ΔV_t curve would be expected.

In subsequent experiments, to explore the impact of the immobilized IgG$_{Receptor}$ on the device specificity, two other states of the sensor surface are investigated. Fig. 4.18 depicts the behavior of the same device as utilized in Fig. 4.17, however, without immobilization of IgG$_{Receptor}$, but instead directly after an air plasma cleaning step (Fig. 4.18a,b) and directly after the deposition of TESPSA (Fig. 4.18c,d), respectively. Again, the analyte solutions are composed of 300 μM PB with 0.002 x PBS and contain HA peptide or IgG$_{Target\_green}$ at varying

concentrations. IgG_{Control_red} is not included in the following investigations, as it is, under the given conditions, expected to behave very similar to IgG_{Target_green}.

The plasma cleaning procedure before recording the curves in Fig. 4.18a comprises 5 min air plasma treatment and 15 min rinsing in an ethanol-water mixture to reduce the reactivity of the surface and inhibit a covalent attachment of the PDMS stamp on top of the device.[66,242]
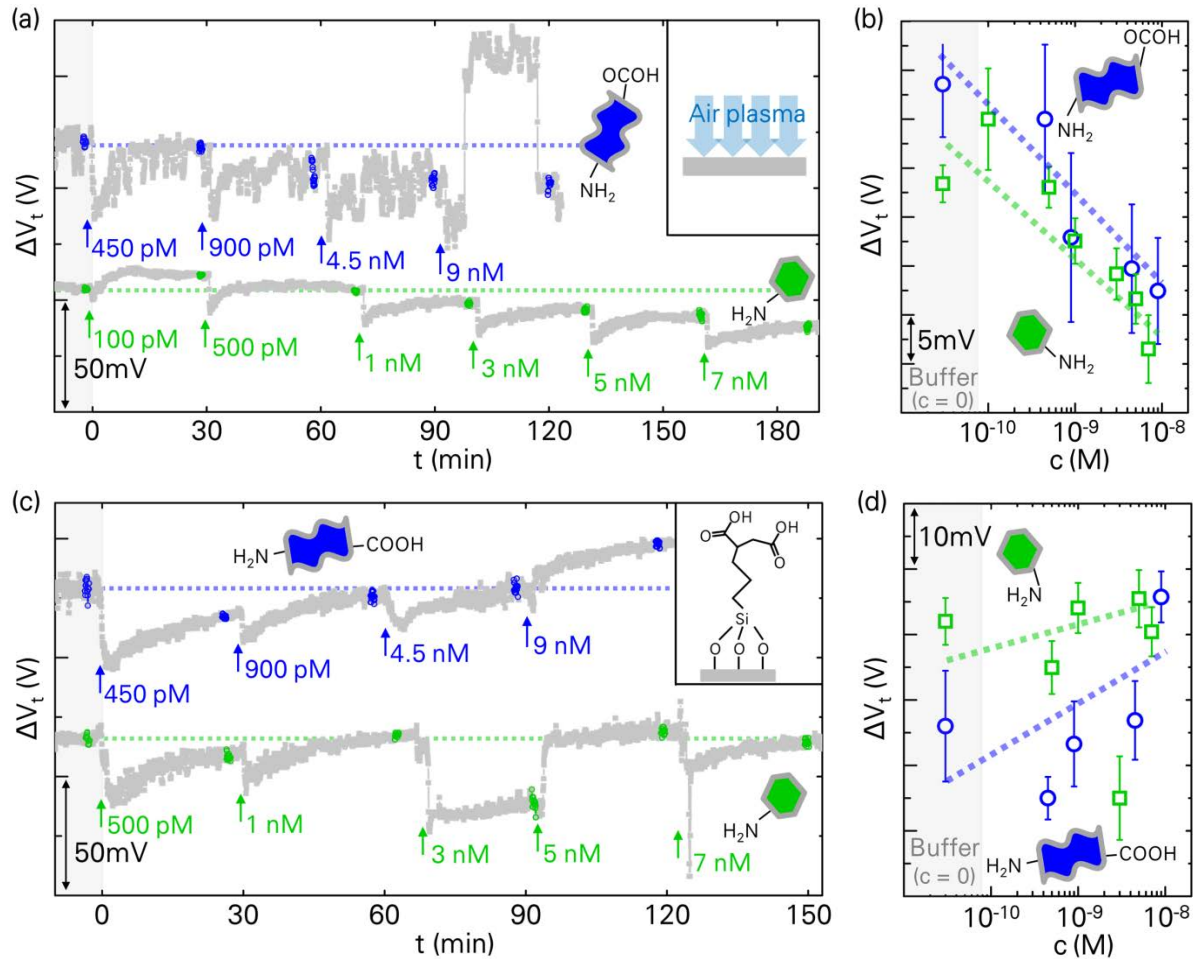

Fig. 4.18: ΔV_t response of the same device utilized in Fig. 4.17, (a & b) directly after an air plasma cleaning procedure and (c & d) directly after depositing TESPSA on the device surface. Sensor signals are recorded during incubation with 300 µM PB solutions with **0.002 x PBS** containing HA peptide, or IgG_{Target_green} as analytes at varying concentrations. (a & c) Time dependent sensor signals. Before $t = 0$ min (time segment with light gray background), pure buffer is applied on the sensor. Starting from $t = 0$ min, solutions with gradually increasing analyte concentrations are incubated on the device. Arrows and adjacent references indicate when the analytes are added at the respective concentrations. Both upper curves with blue indicators and both lower curves with green indicators are related to the addition of HA peptide and IgG_{Target_green}, respectively. The respectively colored dotted lines are guides to the eye to facilitate the recognition of ΔV_t changes. (b & d) Plots of ΔV_t over analyte concentration. Blue circles and green squares correspond to HA peptide and IgG_{Target_green}, respectively. Data points and error bars are determined from the time dependent ΔV_t values highlighted in the curves in (a & c), shortly before changing the analyte concentrations. Data points in the sections having a light gray colored background in (b & d) correspond to pure buffer solutions without analytes. Dotted lines in (b & d) are guides to the eye.

The time dependent ΔV_t curve of the incubation with HA peptide solutions shows a very noisy signal with large amplitudes and one distinct jump to a ~ 50 mV higher temporary ΔV_t plateau level in the middle of the 9 nM incubation time. This behavior is attributed to the early point of time of the ΔV_t measurement directly after the plasma treatment or directly after the above-described rinsing procedure, respectively. The unstable charged species, introduced into the device surface during the plasma cleaning, slowly react with the surrounding matter to enter more stable states.[197,242] This retards the equilibration of the electrochemical double layer at the device-solution interface. Consequently, highly unstable sensor signals are measured, which is also reflected in the huge error bars of the HA peptide concentration-dependent plot of ΔV_t in Fig. 4.18b.

Less noisy behavior is observed, when ΔV_t is measured at a later point of time after the plasma treatment, as can be seen from the IgG_Target_green-related curve in Fig. 4.18a. Consequently, the error bars in IgG_Target_green concentration-dependent plot of ΔV_t in Fig. 4.18b are relatively narrow.

However, the data for both HA peptide and IgG_Target_green in Fig. 4.18a & b indicate merely a drift of the sensor signal. Over the entire concentration range, for both analytes the signal shifts consistently downward.

In case of the just TESPSA functionalized surface in Fig. 4.18c & d, no such distinct downward drift of the signals is observed. Initially, after the TESPSA deposition, the surface is incubated with pure buffer solution so that the succinic anhydride functionalities are hydrolyzed and any formation of covalent amide bonds with primary amines (see chapter 3) is suppressed. During the subsequent addition of the analytes, the ΔV_t values mainly show a slight upward trend, with various ups and downs and one huge outlier after placing 3 nM IgG_Target_green on the sensor surface. It appears as if the TESPSA deposition yields a sensor without any signal stability.

Overall, neither after the plasma cleaning nor after the TESPSA deposition, any correlation between analyte concentration and measured ΔV_t is found. As expected, only the immobilization of IgG_Receptor on the device surface yields dependable signals for distinguishing HA peptide and IgG_Target_green.

The curves in Fig. 4.19 represent a continuation of the experiments shown in Fig. 4.17. Again, the IgG_Receptor is immobilized on the sensor surface. However, the buffer solution is based on 300 µM PB with 0.005 x PBS, instead of 0.002 x PBS, so that higher maximum analyte concentrations can be applied at the expense of a reduced Debye screening length of the liquid (see section 4.3.4.1).

The data in Fig. 4.19 confirm the trend of the initial measurements in Fig. 4.17. Increasing concentrations of HA peptide yield no steady change of ΔV_t. Combining the information

from Fig. 4.17 and Fig. 4.19 leads to the conclusion that the noise of the sensor in case of the HA peptide amounts to ~ 5 mV. Therefore, 5 mV wide light blue and light green strips are included in Fig. 4.19b as guides to the eye for the development of both sensor signals of HA peptide and IgG$_{Target\_green}$, respectively. It is visible that the data of IgG$_{Target\_green}$ suit the assumption of a sensor noise of ~ 5 mV.

With the reduced Debye screening length, compared to the results in Fig. 4.17, slightly higher analyte concentrations, beyond 5 nM, are required to obtain a sufficiently large signal for distinguishing HA peptide and IgG$_{Target\_green}$. Therefore, the limit of detection of the investigated analyte-sensor system is considered to be slightly above ~ 5 nM. Beyond that minimum concentration, the sensitivity of the device for IgG$_{Target\_green}$ is evaluated to be $S_{IgG\_Target\_green}$ ≈ -10 mV/dec.

In Fig. 4.20 two more devices are functionalized with IgG$_{Receptor}$ and tested for their response to increasing amounts of IgG$_{Target\_green}$. The signals are compared to the previous results from
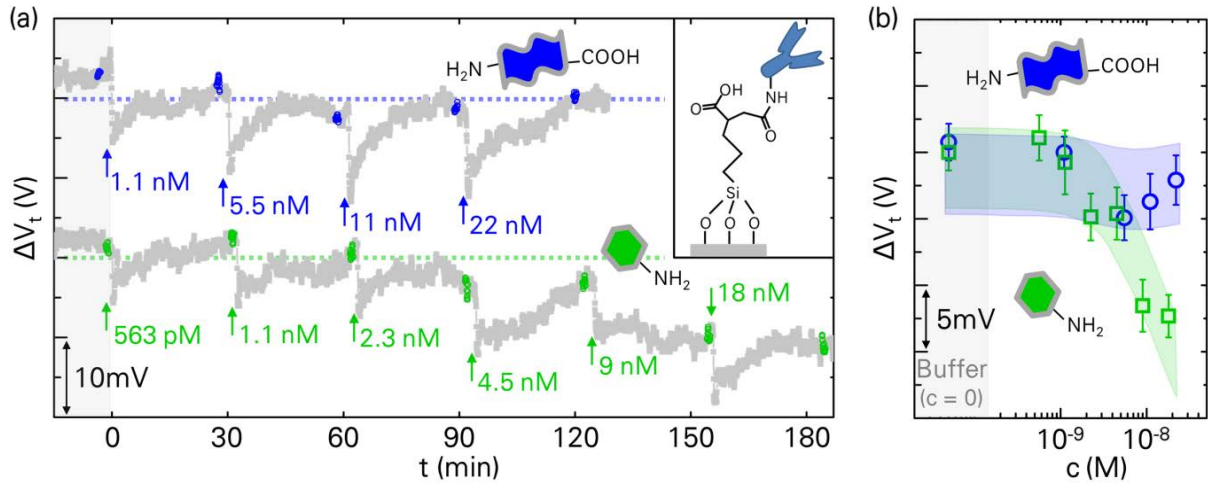

Fig. 4.19: ΔV_t response of the same device utilized in Fig. 4.17 and Fig. 4.18, again functionalized with IgG$_{Receptor}$. This time it is incubated with 300 µM PB solutions with **0.005 x PBS** containing HA peptide, or IgG$_{Target\_green}$ as analytes at varying concentrations. (a) Time dependent sensor signal. Before $t = 0$ min (time segment with light gray background), pure buffer is applied on the sensor. Starting from $t = 0$ min, solutions with gradually increasing analyte concentrations are incubated on the device. Arrows and adjacent references indicate when the analytes are added at the respective concentrations. The upper curve with blue indicators and the lower curve with green indicators are related to the addition of HA peptide and IgG$_{Target\_green}$, respectively. The respectively colored dotted lines are guides to the eye to facilitate the recognition of ΔV_t changes. (b) Plot of ΔV_t over analyte concentration. Blue circles and green squares correspond to HA peptide and IgG$_{Target\_green}$, respectively. Data points and error bars are determined from the time dependent ΔV_t values highlighted in the curves in (a), shortly before changing the analyte concentrations. Data points in the section having a light gray colored background in (b) correspond to pure buffer solutions without analytes. Light blue and light green strips are guides to the eye indicating the ΔV_t development for HA peptide and IgG$_{Target\_green}$, respectively. Both strips are ~ 5 mV wide which is equal to the estimated sensor noise.

Fig. 4.19, reproduced in this graph as green squares. All curves show the same trend. In any case, no significant signal change is observed at analyte concentrations below 1 nM. Beyond $c_{IgG\_Target\_green} = 1$ nM, the strengths of the device signals range between $S_{IgG\_Target\_green} \approx$ -8 .. -14 mV/dec.

On one hand, the apparent device-to-device variations are attributed to possible inhomogeneities in the density of the TESPSA layer as well as the immobilized $IgG_{Receptor}$. Even though silane deposition and receptor attachment are always performed according to the same protocol and the experimental outcome is partially monitored by contact angle measurements, the results from section 4.3.3.4 indicate that the surface chemistry in some cases requires more detailed inspection. For the future, *e. g.* XPS measurements are advisable.

On the other hand, the applied bottom-up assembly of the FETs naturally entails such device-to-device variations, *e. g.* by varying numbers of SiNWs per device. In chapter 5,

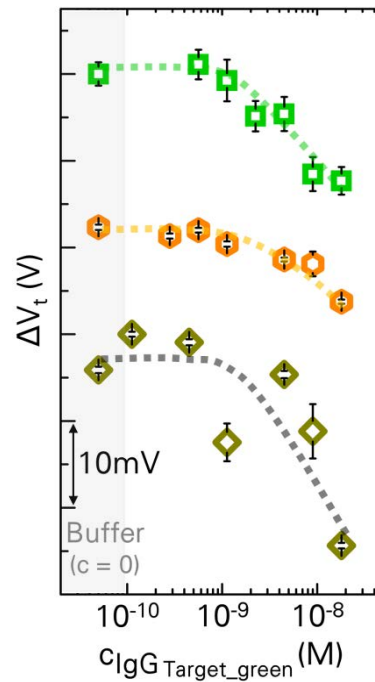Fig. 4.20: ΔV_t response of three different devices functionalized with $IgG_{Receptor}$, incubated with 300 µM PB solutions with **0.005 x PBS** containing IgG_{Target_green} as analyte at varying concentrations. Green squares depict the device already shown in Fig. 4.19, orange hexagons and dark yellow diamonds depict behavior of two further devices. Data points in the section having a light gray colored background correspond to pure buffer solutions without analytes. Dotted lines are guides to the eye.

an approach for a well-defined deposition of bottom-up grown SiNWs is presented which is assumed to increase the device-to-device reproducibility in the future.

Altogether, the data of this section proof the concept that the TESPSA-based receptor immobilization method developed in chapter 3, combined with the bottom-up SiNW-based FETs assembled within this thesis, yields biosensors capable of distinguishing the specific analyte, IgG_{Target_green}, from the nonspecific analyte, HA peptide. For the future, the utilization of different receptor molecules is suggested. Single stranded DNA [25] and aptamers,[26] for example, are capable of capturing analytes much closer to the device surface than antibodies. Consequently, lower Debye screening lengths and, thus, higher ionic strengths of the analyte solutions are applicable. This is expected to positively influence the device specificity, so that also IgG_{Target_green} and $IgG_{Control\_red}$ could be distinguished,[127] similar to the fluorescence-based results in Fig. 3.6 in section 3.3.2.

4.4 CONCLUSION

Within this chapter, the successful assembly of FETs based on cost-efficient bottom-up grown SiNWs is described. After covering the devices with dielectric layers they are implemented in microfluidic set-ups, as described in chapter 2 of this thesis, and applied for sensing pH and ion concentrations. Finally, based on the receptor immobilization method developed in chapter 3 of this thesis, the FET devices are demonstrated to be adaptable for biosensor applications.

5 MICROFLUIDIC ALIGNMENT AND TRAPPING OF NANOWIRES FOR FABRICATING SINGLE-NANOWIRE FETs

As pointed out by the comparative measurements of the sensors in chapter 4, particularly in Fig. 4.20, reproducibly assembling electronic devices from bottom-up grown nanostructures is a challenging task. In this chapter, a simple method for the microfluidic alignment and trapping of one-dimensional (1D) nanostructures from suspension at well-defined positions on a receiver substrate is developed. Instead of implementing a random number of contact printed nano building blocks in each device (see section 4.2.2), the presented approach allows for a subsequent fabrication of single-nanowire field-effect transistors (NW FETs) by contacting the deposited NWs *via* standard UV-lithography (UVL). Silicon as well as copper (II) oxide (CuO) NWs are processed, and up to 13 out of 32 designated trapping sites are occupied with single-NW FETs. Parts of this chapter are published elsewhere.[250]

5.1 MOTIVATION

In section 4.2.1 of this work, it is shown that 1D nanostructures, such as SiNWs, can be readily synthesized in large quantities in bottom-up growth processes. There are various approaches to fabricate 1D nanostructures from metals,[251–254] organic molecules [255,256] and semiconductors.[19,24,32,34,35,38–40,199,203,257–268] Compared to their top-down counterparts, bottom-up 1D nanostructures offer superior electronic properties,[39] better control in the fabrication of heterostructures with axial [251,252,257] and radial [258] variations, and smaller achievable structures down to the molecular scale.[38,203]

The great potential of bottom-up NWs has been demonstrated not only in FETs [39] and (bio-) sensors.[19,24,32,34,35,40,253] but also in other nano-electronics and in nano-photonics applications, such as light-emitting diodes,[257,258] microcavity lasers,[259] waveguides [255,260] and photodetectors.[256,261]

Within this work, NWs are of high importance as building blocks for the assembly of sensors that enable label free real-time monitoring of biologically and medically relevant data with detection limits for proteins[19,24,32] or DNA[34,40] down to the fM-range. There is evidence that the highest sensitivity is achieved employing single-NW devices,[32] which even allow for detecting single viruses,[35] and potentially single molecules.[19] To obtain multiplexed biosensors[24] that enable simultaneous monitoring of several analytes with maximized sensitivity, it is necessary to fabricate multiple single-NW devices on one chip. This, however, requires precise positioning of "bottom-up" 1D nanostructures on substrates, which is an ongoing challenge.

Several techniques – each of them with specific advantages and limitations – have been developed to arrange these nanostructures. Manipulation approaches making use of optical tweezers [269] or the hybridization of NW- and substrate-linked single DNA strands [270] are very laborious and not applicable on a large scale. Arranging NWs via electric [254,266] or magnetic fields [251] yields single-NW devices, but is limited with regard to material choice and requires expensive equipment. Alignment approaches based on spray coating,[262] bubble-blown films,[263] Langmuir-Blodgett technique,[253,264] mechanical printing [199,265,268] or capillary forces [252] enable an efficient deposition of NWs over large areas, however, for reliably contacting single NWs, costly electron-beam lithography (EBL) processing is required.

When aligning 1D nanostructures *via* microfluidics, as demonstrated by Huang and co-workers, EBL is also indispensable for contacting individual NWs.[267] The deposited NWs are well oriented parallel to the liquid flow direction, yet spatial precision is limited.

The issue of full spatial control can be overcome by microfluidic trapping, as it has been demonstrated for spherically shaped, micrometer sized particles [56] and cells.[57] In contrast, 1D nanostructures have orders of magnitude smaller diameters and significantly higher aspect ratios. Hence, the formerly presented trapping layouts are not applicable to NWs.

In this chapter, a microfluidic set-up is developed, which enables the alignment of 1D nanostructures and their trapping at designated positions. The deposition of single NWs and their subsequent contacting *via* conventional UVL is demonstrated indicating the simplicity and the high scalability and cost-efficiency of the approach.

Within this work, three types of NWs are used. (i) Commercially available monodisperse SiNWs in an isopropanol-based suspension (*p-i-p* doped, diam. $\times$ L 150 nm $\pm$ 30 nm $\times$ 20 μm $\pm$ 2 μm, 10^6 wires ml^{-1}, Sigma Aldrich, USA). (ii) "Homemade" polydisperse SiNWs grown based on the recipe described in section 4.2.1. (iii) "Homemade" polydisperse CuO NWs grown *via* oxidation of Cu substrates.

In the following, section 5.2 explains the developed microfluidics-based NW deposition and contacting approach using the commercially available monodisperse SiNW suspension. The electrical characteristics of the fabricated FETs are demonstrated in section 5.3. Subsequently, section 5.4 presents the fabrication of the polydisperse NW suspensions and their utilization in the microfluidic alignment procedure. In section 5.5, possible adjustments of the technique for higher yields of single-NW devices are discussed. Finally, in section 5.6 an outlook on future applications of the developed method is provided.

5.2 NANOWIRE ALIGNMENT, TRAPPING AND CONTACTING

5.2.1 Basic working principle

In this section (section 5.2.1), a basic overview of the strategy for aligning, trapping and contacting single-NW devices is presented. The subsequent sections (sections 5.2.2 - 5.2.7) provide more detailed explanations on specific steps of the procedure.

As introduced in section 1.2, one characteristic feature of microfluidics is the strictly laminar flow of fluids through the respective devices.[16,17] As presented by Huang *et al.,*[267] the laminar flow regime and its inherent forces on rod-like structures allow for aligning NWs in flow direction.[271,272] Within this work, a microfluidic chip is designed which aligns NWs along the liquid flow and guides them into sufficiently narrow channels, so that an abrupt 90° change of the channel direction leads to a trapping of the 1D nanostructures. By dividing the microfluidic structure into multiple sub-channels, several NWs can be trapped in parallel.
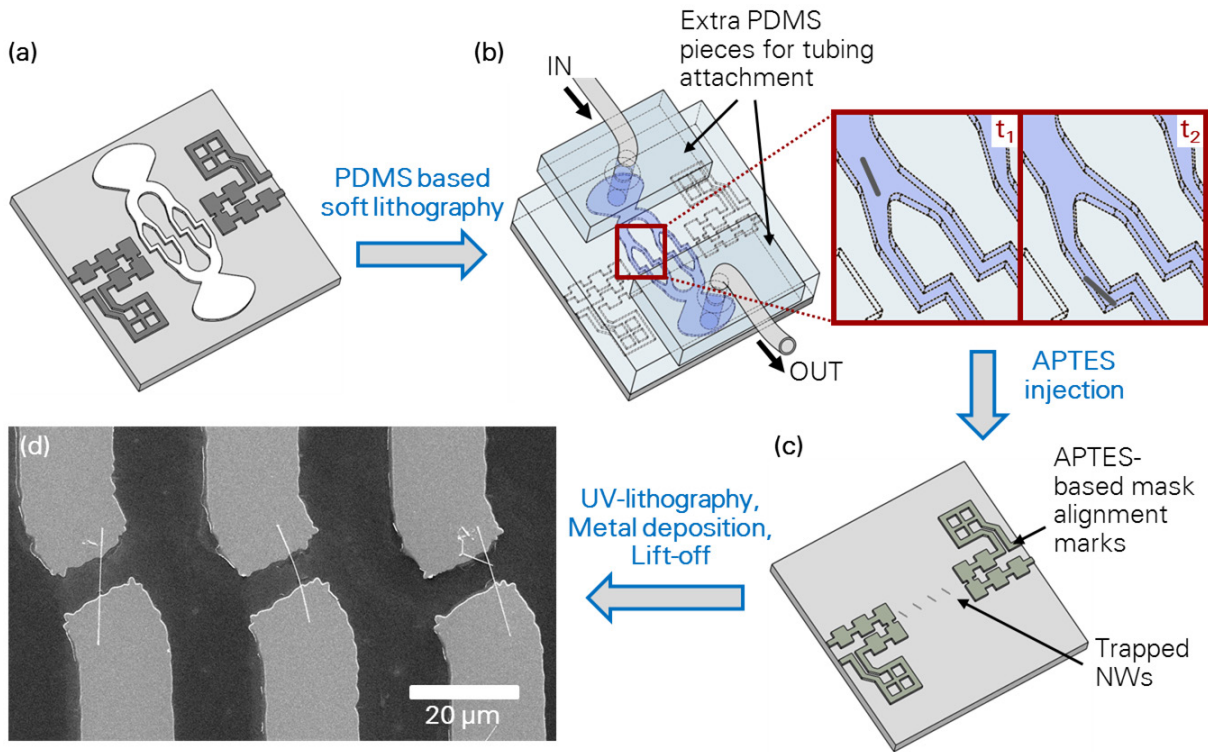

Fig. 5.1: Schematic of the basic working principle for single-NW FET fabrication. (a) Fabrication of SU-8 master for soft lithographic replication with PDMS. The master contains micro-channels for NW alignment and trapping (white) and channels for depositing UVL mask alignment marks (dark gray). (b) Assembly of flow set-up for trapping NWs from suspension. Suspensions are drawn through channels under reduced pressure of 10 kPa applied *via* a syringe pump at the outlet. Tubing is first attached to extra PDMS pieces which are then bound to the PDMS stamp containing the micro-channels. In the enlarged view of the red labeled section, the process of NW trapping is shown ($t_1 < t_2$). NWs are first flow-aligned and guided into the trapping sites (t_1), then trapped and deposited (t_2). (c) After NW trapping and formation of cross-linked APTES mask alignment marks the flow set-up is dismounted for further NW contacting via UVL. (d) Representative SEM image of contacted SiNWs.

Simultaneously deposited mask alignment marks, adjacent to the trapping sites, enable a subsequent contacting of the NWs *via* UVL.

For casting the PDMS-based flow chambers (see also chapter 2), master structures of 10 µm height are fabricated using SU-8 2010 (MicroChem, USA). Fig. 5.1a depicts a schematic of the utilized master structure. The parts of the structure highlighted in dark gray form the channels for the deposition of mask alignment marks. The part of the structure highlighted in white forms the channels for aligning and trapping the NWs.

Within the trapping structure, the broad main channel successively branches over several stages into progressively smaller sub-channels. At the trapping sites – *i. e.* the kinks in the middle of the structure – the channels are 6 µm wide. For drawing the NW suspension through the channels, a reduced pressure of 10 kPa is applied *via* a syringe pump at the outlet. The NWs align along the laminar flow [271,272] and are guided into the trapping sites (at t_1 in Fig. 5.1b). Here, the NWs cannot follow the liquid flow at the abrupt 90° change of the channel direction. Consequently, they are trapped and deposited on the receiver substrate (t_2 in Fig. 5.1b).

For depositing the UVL mask alignment marks, 3-aminopropyltriethoxysilane (APTES, see also section 1.4.2.3 and chapter 3) is injected into the channels to the left and to the right of the trapped NWs *via* capillary forces.[164] In a condensation reaction, the silane molecules bind covalently to the oxide surface of the silicon wafer substrate and cross-link among each other.[147] Consequently, solvent-resistant mask alignment marks remain on the substrate surface after dismounting the PDMS flow chamber (see Fig. 5.1c). The resistance of the alignment marks against organic solvents is important to prevent their dissolution during photoresist spin coating for subsequent UVL.

By means of the APTES-based alignment marks, one pair of Ni contacts (source and drain) for each designated trapping site is deposited *via* UVL in combination with a lift-off and NW contacting procedure as described in section 4.2.3. A representative scanning electron microscopy (SEM) image of the contacted SiNWs is shown in Fig. 5.1d. All depicted devices are single-NW FETs.

5.2.2 Optimized trapping channel layout

Initially, several possible channel layouts and trapping structures were designed a selection of which is shown in Fig. 5.2. Within her Diploma thesis,[273] N. Haustein evaluated the NW trapping efficiencies of these flow structures and optimized the most suitable one, depicted in Fig. 5.2d, by means of theoretical flow calculations and experimental work with regard to a more homogenous flow behavior and a more reliable NW trapping yield. For the theoretical calculations, she used Comsol Multiphysics® including the computational fluid dynamics module.

NW suspension flow direction
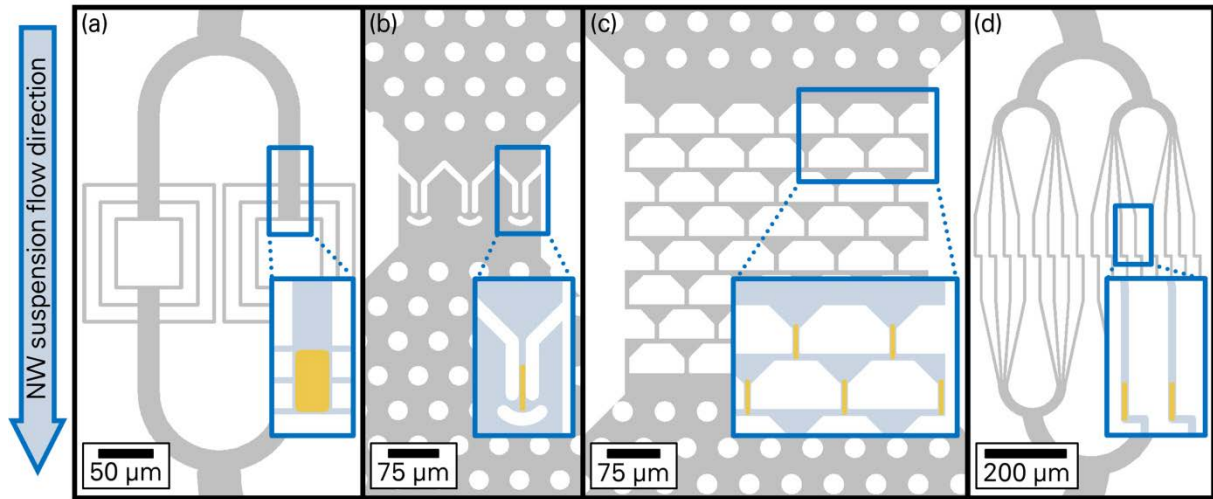
50 µm

75 µm

75 µm

200 µm

Fig. 5.2: Initial trapping channel layouts designed within the framework of this thesis. Blue-framed insets show magnified the intended trapping sites highlighted in orange. In (b) and (c) support posts, as described in section 2.3.2, are included in the in- and outlet regions.

Fig. 5.3 shows the final trapping channel layout, including simulated flow velocities of isopropanol at a pressure difference of 10 kPa between in- and outlet (further utilized *in silico* simulation parameter listed in the appendix). In the final design, the broad main channel of the fluidic structure branches over four stages into 32 sub-channels containing the trapping sites. Based on the intended 6 µm channel width at the trapping sites, a generalized Murray's law is used to obtain the optimum channel widths at the other sections. Murray's law is a biomimetic design rule, based on the principle of minimum work, derived by Murray in 1926.[274] Barber and Emerson formulated a generalized version of this law, which allows for calculating the optimum width ratio between parent and daughter vessels in microfluidic manifolds of constant channel height.[275]

Tab. 5.1 summarizes the optimized channel widths at different branching stages for the utilized 10 µm-high flow structure. Enumerations for the branching stages are the same as depicted in Fig. 5.3.

In addition to the channel widths, the lengths of the branches on the inlet side of the trapping sites are optimized. For each branching stage, the hydrodynamic entrance length of the sub-channels is determined – *i. e.* the axial distance at which the centerline velocity in the sub-channel reaches 99 % of its value for the fully developed flow profile.[276] Twice the simulated entrance length is added to the branches on the inlet side of the trapping sites to allow the flow profile to sufficiently stabilize, so that the NWs have a sufficient amount of time or space, respectively, to align with the flow. On the outlet side of the trapping sites no additional channel elongation is required.

Furthermore, support posts, similar to the ones described in section 2.3.2, are included in the channels at the inlet and outlet regions as well as at the branching stages 1 and 2 (see Fig. 5.3) to prevent the channels from collapsing.

As Fig. 5.3 illustrates, the velocity reaches its maximum at the trapping sites. In the other sections of the structure the velocity is lower and, more importantly, very uniform. Therefore, it is assumed that each inflowing NW can end up in any of the trapping sites with equal probability.
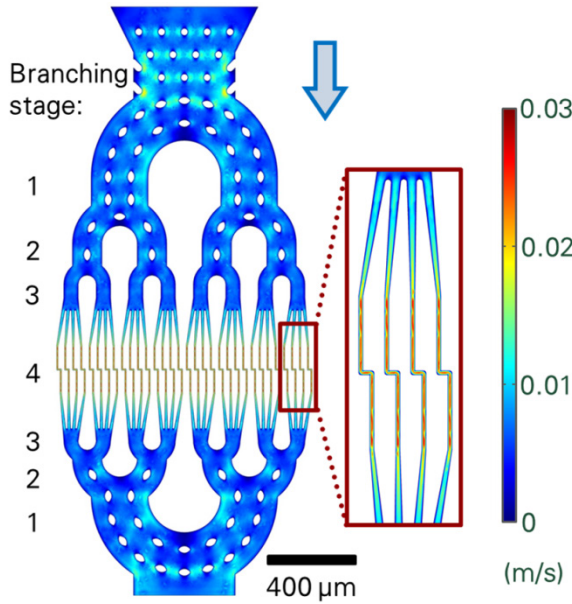

Fig. 5.3: Layout of the final microfluidic channel for alignment and trapping of 1D nanostructures, including the numbering of the branching stages and simulated flow velocities. Flow direction indicated by blue arrow. (Courtesy of N. Haustein)

Tab. 5.1: Optimized channel widths in the 10 μm-high flow structure at different branching stages. Optimization carried out on basis of a generalized Murray's law.[274,275] Branching stages numbered as in Fig. 5.3c. (Courtesy of N. Haustein)
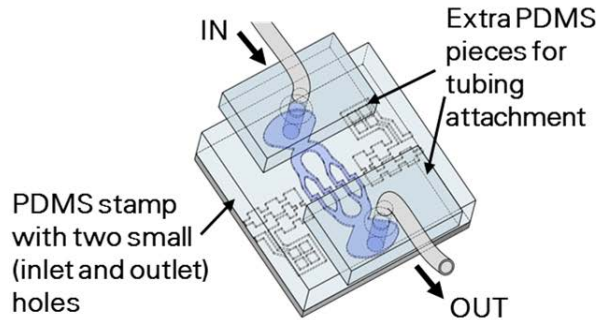
Branching stage	Number of branches	Optimized channel width (μm)
4	32	6[#]
3	8	64
2	4	130
1	2	250
In-/outlet	1	446

[#] At this stage, 6 μm channel width is the default value

5.2.3 Assembly of trapping set-up

When assembling the flow set-up, it is important to prevent any distortion of the PDMS stamp and, thus, misalignment between trapping sites and mask alignment marks.
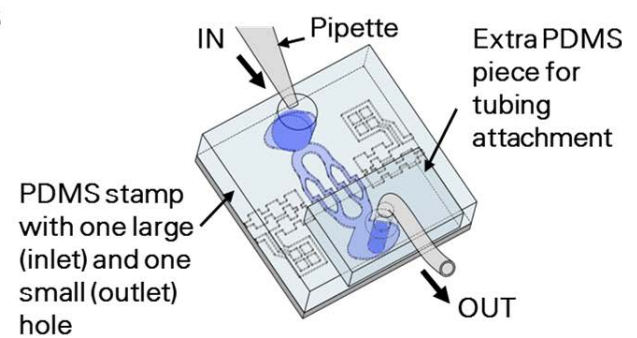

Fig. 5.4: Schematic assembly of microfluidic flow set-ups for trapping NWs from suspension. Suspensions are drawn through channels under reduced pressure of 10 kPa, applied via a syringe pump at the outlet channel. Tubing is first attached to extra PDMS pieces which are then bound to the PDMS stamp containing the microchannels. (a) Tubing attached at both inlet and outlet. (b) Punching a large inlet hole into the PDMS stamp allows for direct pipetting of NW suspensions into the microchannels.

Therefore, the PDMS stamp is placed very gently on the silicon wafer receiver substrate merely utilizing the adhesion forces of the PDMS [73] to seal the structure. Additionally, the required tubing is not plugged into the PDMS stamp containing the microchannels, because this would strain the material. Instead, the tubing is attached to extra PDMS pieces, which are then bound to the main PDMS replica of the microchannels *via* self-adhesion.[73]

Besides the assembly approach presented in Fig. 5.1b with tubing attached at both in- and outlet, there is the possibility to punch a large inlet hole of 3 mm diameter into the PDMS stamp which allows for direct pipetting of NW suspensions into the microchannels. Both set-ups are juxtaposed in Fig. 5.4.

5.2.4 Flow-through processing of NW suspension

As will be further explained in section 5.4.1, isopropanol is used as basis for all NW suspensions within this work. Since isopropanol is known to swell PDMS,[72] the stock NW suspensions are mixed 1:1 (vol./vol.) with deionized water directly before the flow experiments. This dilution of the organic solvent minimizes the swelling of PDMS, so that no distortions occur between trapping sites and alignment marks.

In case of the commercial SiNW suspension, sample volumes below 5 µl are consumed per experiment. These experiments require a delicate, but slow, sample uptake *via* inlet tubing. The flow set-up assembly depicted in Fig. 5.4a is used. When working with the SiNW and CuO NW suspensions fabricated within this work (see section 5.4), since their NW concentration is relatively low, sample volumes of up to 20 µl are applied. Taking up such large sample volumes *via* inlet tubing would be very time consuming. In these cases, the flow set-up assembly depicted in Fig. 5.4b is preferably used.

By means of a syringe pump and a manometer, the NW suspensions are drawn through the channel set-up at a reduced pressure of 10 kPa.

5.2.5 Alignment mark deposition

Mask alignment marks made of APTES are utilized for the subsequent contacting of the trapped and deposited NWs. Parts of the channels for alignment mark deposition are shown in Fig. 5.5. Fig. 5.5a & c depict SEM images of the receiver substrate at the end of the alignment and trapping procedure after dismounting the PDMS stamp. The previous position of the NW trapping channels is discernible as bright traces in-between the white dotted lines in Fig. 5.5a. To the left (not shown here) and to the right of the trapping sites, the APTES-based alignment marks are deposited.

The channels for the alignment mark deposition possess an opening at the side of the PDMS stamp. Drops of APTES are brought in contact with the channels, and the silane
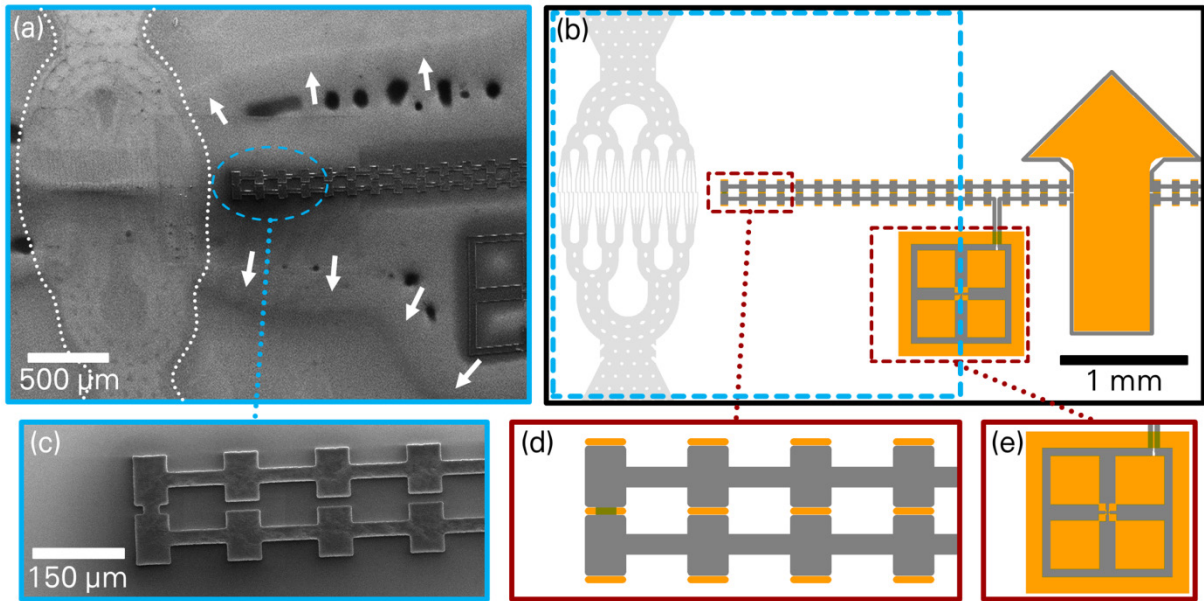
Fig. 5.5: Deposition of APTES-based mask alignment marks. (a) SEM image of receiver substrate after dismounting PDMS stamp. In-between the white dotted lines, bright traces of the NW alignment channels are visible. To its right, the APTES-based alignment marks are deposited. White arrows indicate the outline of what is assumed to be the imprint of the swollen part of the PDMS stamp due to a release of ethanol during APTES crosslinking.[72] (b) Drawing of the channel layouts. In light gray, the channels for NW trapping and in dark gray, the channels for the deposition of the APTES-based alignment marks. In orange, drawing of the corresponding alignment marks on the mask for contacting the NWs. The arrow included in the alignment mark layout indicates the NW suspension flow direction of the device. The blue-framed part represents the area depicted in (a). (c) Magnified SEM image of the blue circled alignment mark section in (a). (d & e) Magnified view on the red-framed parts of the alignment marks in (b).

enters the channels *via* capillary forces.[164] Inside the channels the APTES molecules bind covalently to the oxide surface and/or cross-link among each other *via* their three hydrolysable groups (see section 1.4.2.3).[147] After inserting the silane into the channels, it is allowed to crosslink for at least 12 h before dismounting the PDMS stamp from the receiver substrate.

The APTES-based alignment marks have the advantage that they are insoluble in organic solvents. Thus, they do not vanish while spin coating photoresist onto the substrate as required for UVL when contacting the wires. However, during the condensation reaction of APTES, ethanol is released, which is also known to swell PDMS.[72] Consequently, minor deformations of the microchannels occur during the deposition of the mask alignment marks. In the SEM image in Fig. 5.5a, the APTES-based alignment marks are surrounded by imprints the outlines of which are indicated by white arrows. These imprints are assumed to originate from an ethanol-based swelling of the PDMS parts in the vicinity of the channels for alignment mark deposition. At the crosses of the alignment pattern (see Fig. 5.5e), about 2 mm away from the center of the trapping structure, there are deviations of a few micrometer between specified and obtained alignment mark positions. These deformations

decrease the accuracy of the mask alignment during UVL. However, already the alignment accuracy achieved when focusing on the alignment structure closest to the trapping sites, depicted in see Fig. 5.5c & d, is sufficient to reliably contact the deposited NWs. Fig. 5.5c demonstrates the high quality of the APTES structures achieved with the described procedure.

One possible approach for reducing the swelling of the PDMS might be the application of silanes with methoxy instead of ethoxy hydrolysable groups. Then, during the crosslinking of the alignment mark structures, methanol instead ethanol will be released. Methanol swells PDMS only half as much as ethanol.[72]

5.2.6 Disassembly of trapping set-up and single-NW yield

In case of the commercial, monodisperse SiNW suspension, when using the optimized trapping structure described in section 5.2.2, rarely more than two SiNWs per trapping site are deposited – even if optical microscopy observations during the flow experiments indicate the trapping of an increased amount of SiNWs. As emphasized by the images in Fig. 5.6 from preliminary experiments using the trapping structure depicted in Fig. 5.2b, large amounts of trapped SiNWs are lifted off the receiver substrates upon dismounting the PDMS flow chamber. It is assumed that mainly SiNWs having contact to the receiver substrate over their entire length stay on the substrate surface. SiNWs having only partly or no contact to the substrate – *e. g.* due to lying on top of other SiNWs – are removed with the PDMS stamp, due to adhesion forces between stamp and NWs.[73]
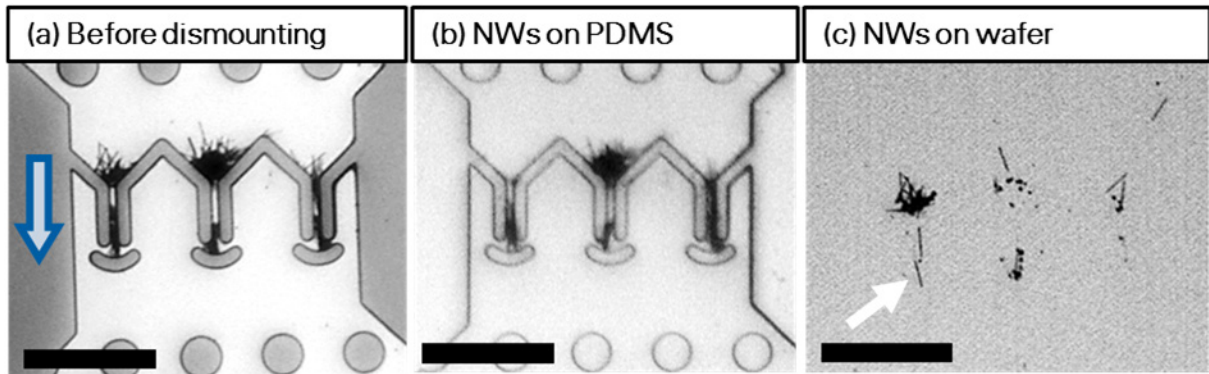

Fig. 5.6: Optical microscopy images of trapping experiment with NW trapping structure utilized in preliminary experiments (see also Fig. 5.2b). The blue arrow indicates the flow direction. Scale bars denote 100 µm. Although this trapping structure does not provide sufficient control over the NW positioning, it can be used for trapping large amounts of NWs, for studying the interactions between NWs and PDMS stamp, and NWs and receiver substrate, respectively. (a) Before dismounting the flow assembly, large amounts of NWs are trapped in the intended trapping sites, but also in other sections of the channel. (b) After dismounting the alignment chamber, a large proportion of the trapped NWs adheres to the PDMS stamp, assumingly due to the high adhesion forces of the PDMS. (c) On the wafer, only two non-overlapping NWs are left at the trapping site, indicated by the white arrow. (Courtesy of N. Haustein)

Based on this mechanism, after contacting the NWs (see section 5.2.7), up to 13 out of 32 designated trapping sites are occupied with single-SiNW FETs. On average, 25-40% of the produced FET devices do not contain any SiNWs, 35-40% contain one SiNW, 15-25% contain two SiNWs, and below 10% contain more than two SiNWs. These yields are comparable to earlier works in this field, such as electric field-based NW alignment.[254,277] More recent electric field-based approaches [266] and EBL-supported deposition and contacting techniques [268] achieve significantly higher yields of single-NW devices. However, the approach developed within this work uniquely unites simplicity, cost-efficiency and versatility.

5.2.7 Contacting the NWs

Within her diploma thesis, N. Haustein found that the commercial, monodisperse SiNWs are deposited in tilted positions, on average with an angle of $21° \pm 5°$ between NW and channel wall (see Fig. 5.7a). Using the APTES-based alignment marks, one pair of metal contacts (source and drain) is deposited for each designated trapping site. In the design of the metal contacts the observed NW tilt is taken into account, as schematically shown in Fig. 5.7b.

Fig. 5.7: (a) Schematic drawing of the average tilted deposition of the NWs with respect to the trapping channel sidewalls. (b) Schematic drawing showing how NW tilt is considered in the source (S) and drain (D) metal contact layout.

When contacting the SiNWs, Ni is used as electrode material. In accordance with the recipe described in section 4.2.3, AZ5214e image reversal photoresist is used as negative resist in the UVL procedure. Immediately before depositing 175 nm Ni on the devices (High Resolution Ion Beam Coater, Gatan, USA), the samples are dipped in 1% HF for 40 s to remove the native SiO_2 shell from the SiNWs. After metal deposition and lift-off in acetone, the samples are rinsed in isopropanol and dried under a stream of N_2. Subsequently, the samples are annealed in forming gas (N_2:H_2 10:1, 10 mbar, 450 °C, 3 min, ATV SRO-706 Reflow Oven, ATV Technologies, Germany) to lower the contact resistance.

Fig. 5.1d and Fig. 5.8a show representative scanning electron microscopy (SEM) image of contacted SiNWs. All depicted devices are single-NW FETs.
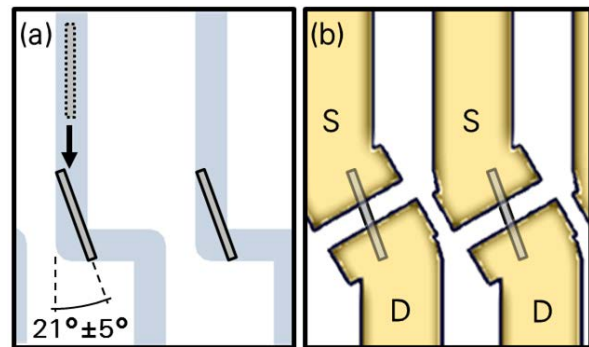
5.3 CHARACTERISTICS OF FETs FROM COMMERCIAL MONODISPERSE SINW SUSPENSION

Fig. 5.8 summarizes the electronic properties of the SiNW FETs fabricated within this work. In all cases, the receiver substrates are Si wafer with 200 nm thermal oxide (Active Business Company GmbH, Germany). For characterizing the back-gated devices, the same PM8 Prober set-up as described in section 4.3.1 is used.

Fig. 5.8a shows five neighboring single-NW FETs. In Fig. 5.8b & c the representative I_{SD}-V_{BG} and I_{SD}-V_{SD} characteristics of the highlighted single-SiNW FET (see Fig. 2a) are plotted. The characteristics demonstrate a p-type behavior of the devices, as expected for the purchased p-doped SiNWs. At V_{SD} = 5 V, average on-currents of approximately 0.25 nA per single-SiNW FET are observed.

As pointed out in section 5.2.6, there are also trapping sites where no SiNW or more than one SiNW is contacted. The averaged drain-currents of three different kinds of devices (0, 1 or 2 SiNWs per FET) are compared in Fig. 5.8d. As expected, the graph shows that the output current scales with the number of SiNWs per FET.
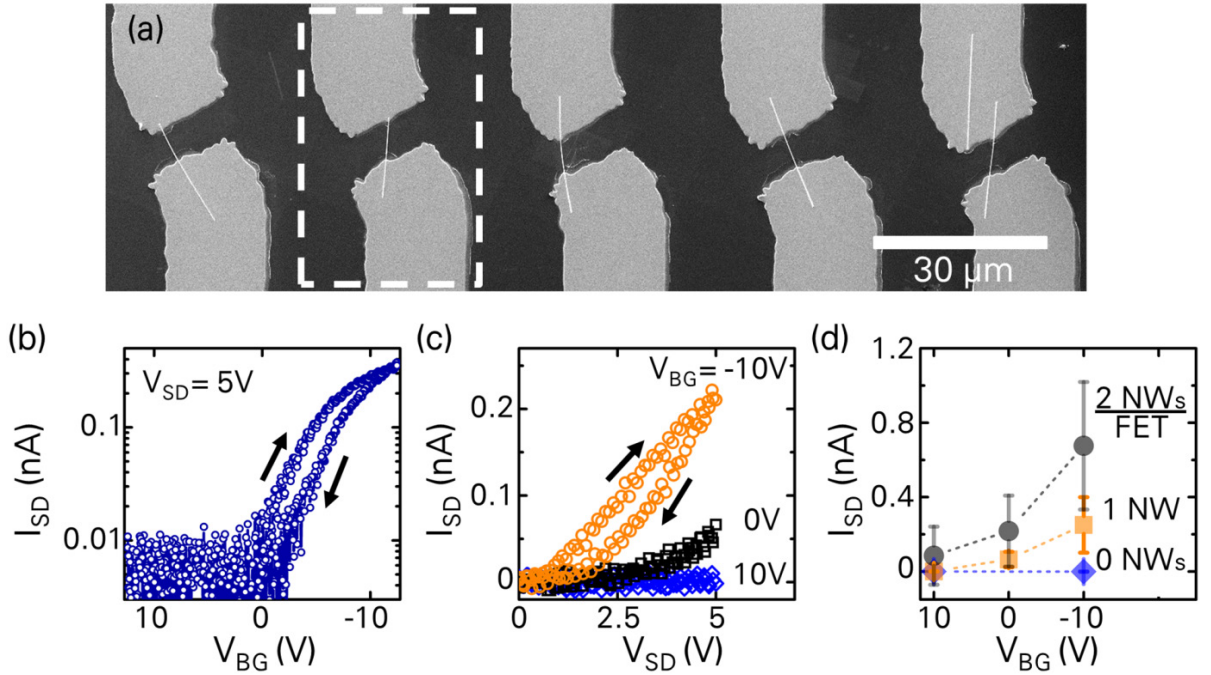

Fig. 5.8: SiNW FET characteristics. (a) SEM image of five neighboring back-gated single-SiNW FETs. (b) Representative single-SiNW FET I_{SD}-V_{BG} output curves recorded with the device highlighted in (a) at V_{SD} = 5 V. (c) Representative single-SiNW FET I_{SD}-V_{SD} output curves recorded with the device highlighted in (a) at different gate voltages: orange circles, black squares, blue diamonds correspond to V_{BG} = 10 V, 0 V, 10 V respectively. (d) Comparison of averaged drain currents in FET devices with different numbers of SiNWs at V_{SD} = 5 V: black circles, orange squares and blue diamonds correspond to 0, 1 and 2 SiNWs per FET, respectively. Note the reverse direction of V_{BG} -axis in (b & d).

The measured currents are relatively low compared to other SiNW devices in literature.[39] The deviations are attributed to two effects. First, the thick gate oxide and back-gate geometry lead to a low gate coupling. Second, the commercial SiNWs utilized within this work are not passivated so that charge trapping within the native oxide shell occurs. This effectively screens the gate coupling (see section 1.3.4).

For the future, at the NaMLab gGmbH, there is the vision to fabricate NWs that are readily passivated, *e. g.* with thermal SiO_2 and high-k dielectrics, and that possess surrounding gate electrodes. Applying such bottom-up 1D nanostructures in the presented alignment and trapping set-up is expected to yield single-NW FETs with improved electrical characteristics. Initial experiments for applying NW suspensions made from "homemade" 1D nanostructures are presented in section 5.4.

Additionally, compared to the contact printing approach described in section 4.2.2, the microfluidics-based deposition of bottom-up grown NWs presented in this chapter enables the utilization of receiver substrates with very thin oxide layers without the risk of scratching the surface and producing devices with high leakage currents. Consequently, in future experiments the gate oxide thickness can readily be reduced for enhancing the device performance.

5.4 "HOMEMADE" NANOWIRE SUSPENSIONS

The successful fabrication of single-NW FETs using the commercially available SiNW suspension in combination with the relatively poor electrical characteristics of the respective devices generates a demand for "homemade" NW suspensions with better control over the electrical properties of the NWs. In this section, the fabrication of polydisperse NW suspensions made from bottom-up grown SiNWs and CuO NWs is described. Furthermore, their applicability for the fabrication of single-NW FETs with the presented microfluidics-based alignment and trapping approach is tested.

It is expected that the optimized flow structure (see Fig. 5.3) works specifically well with NWs having similar mechanical properties as the applied commercial SiNWs. The NW length and the NW stiffness are regarded as the two most essential aspects determining the success of the alignment and trapping procedure. Considering that the NWs depicted in Fig. 5.1, Fig. 5.6 and Fig. 5.8 show hardly any bending, rather stiff NWs of at least 20 μm length are assumed to be optimum ingredients for the "homemade" NWs suspensions.

5.4.1 Suspension medium

The commercial SiNWs are delivered in an isopropanol-based suspension. Due to their native oxide shell, SiNWs possess a polar surface, just as CuO NWs.[278] As a polar solvent or suspension medium, respectively, isopropanol inhibits the agglomeration of such polar nano-sized objects, which explains its frequent application for similar purposes in other

references.[120,254,262,266] Consequently, also the NWs grown within this work are dispersed in isopropanol by harvesting them *via* ultrasound.

5.4.2 Polydisperse SiNW suspensions

As described in section 4.2.1, the bottom-up growth of SiNWs enables a cost-efficient production of innumerable amounts of semiconducting nano-sized building blocks. Experience shows that harvesting SiNWs in liquid *via* ultrasound often yields suspensions of NW pieces significantly shorter than the actual NW growth length.[120] Therefore, within this work, for preparing SiNW suspensions, at first a 20 nm thick Al_2O_3 sacrificial layer is atomic layer deposited [(3)] on the growth substrate surface, before immobilizing seed gold nanoparticles (AuNPs) on top. The idea is, as depicted in Fig. 5.9, to first grow the NWs, then etch away the sacrificial Al_2O_3 layer using H_3PO_4 [279] and finally disperse the NWs over their entire length in isopropanol.

For depositing the linker silane TESPSA and seed AuNPs on top of the Al_2O_3 layer and for growing the SiNWs, the same recipes as described in section 3.2.4 and in section 4.2.1, respectively, are applied. For etching the sacrificial layer, growth substrates are dipped over
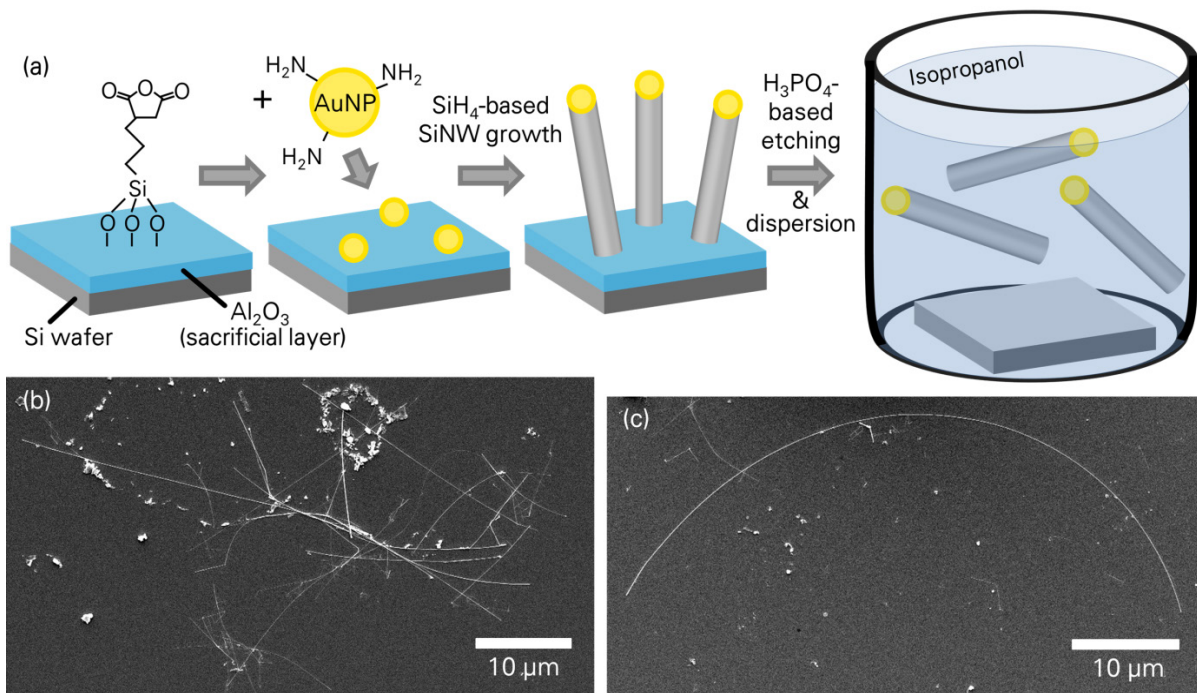

Fig. 5.9: Preparation of SiNW suspension. (a) Schematic drawing of growth and harvesting procedure. Al_2O_3 is used as sacrificial layer. After deposition of seed AuNPs on the TESPSA functionalized surface and catalytic growth of SiNWs in a SiH_4-enriched CVD atmosphere (see section 4.2.1), Al_2O_3 is etched using a 5 vol.% aqueous H_3PO_4 solution. Subsequently, the SiNWs are dispersed in isopropanol. (b & c) SEM images of SiNWs deposited on Si wafer surface from a 5 µl drop of isopropanol-based SiNW suspension.

[(3)] ALD chamber: Roth & Rau AG (Germany). 300°C, 266 cycles: introduction of TMA for 20 ms, N_2 purge for 5 s, introduction of O_3 und reaction time of 5 s, N_2 purge for 3 s (see also section 4.2.4).

night in 5 vol.% aqueous H_3PO_4 solution. After rinsing the substrate twice in water, it is dipped into isopropanol and sonicated for 1 s so that the SiNWs are released. The sonication is kept as short as possible, because sonicating for much longer than 1 s could break already harvested SiNWs in the suspension into smaller pieces.

The SEM images in Fig. 5.9b,c show SiNWs that remained on a fresh Si wafer after putting a 5 μl drop of the produced NW suspension on its surface and evaporating the isopropanol. In both cases, the longest NWs exceed 40 μm in length indicating a successful dispersion of the respective NWs over their entire lengths. It appears that most of the NWs do not detach from the growth substrate during the H_3PO_4-based etching step. Instead, the etching step only weakens the connection to the substrate making the NW segments closest to the substrate surface preferential breaking points during sonication. This facilitates harvesting long SiNWs in isopropanol. However, as exposed in Fig. 5.9b, there are also undesirably short NW fragments in the suspension. Furthermore, the bending of the NW in Fig. 5.9c demonstrates that its stiffness is undesirably low compared to the commercial SiNWs.

When applying the produced SiNW suspension in the microfluidic alignment and trapping set-up depicted in Fig. 5.4b (see section 5.2.3), the high flexibility of the produced SiNWs yields huge complications in the experimental procedure. Fig. 5.10 shows a single-SiNW deposited at a trapping site (Fig. 5.10a) and large SiNW agglomerates deposited at the inlet area of the flow structure (Fig. 5.10b). It appears that in the microfluidic channel, most of the SiNWs entangle together, making them useless for the actual alignment and trapping procedure. Furthermore, the SiNW depicted in Fig. 5.10a, with its curvature and its short NW length, is assumed to be not trapped but accidently deposited near the intended trapping site.
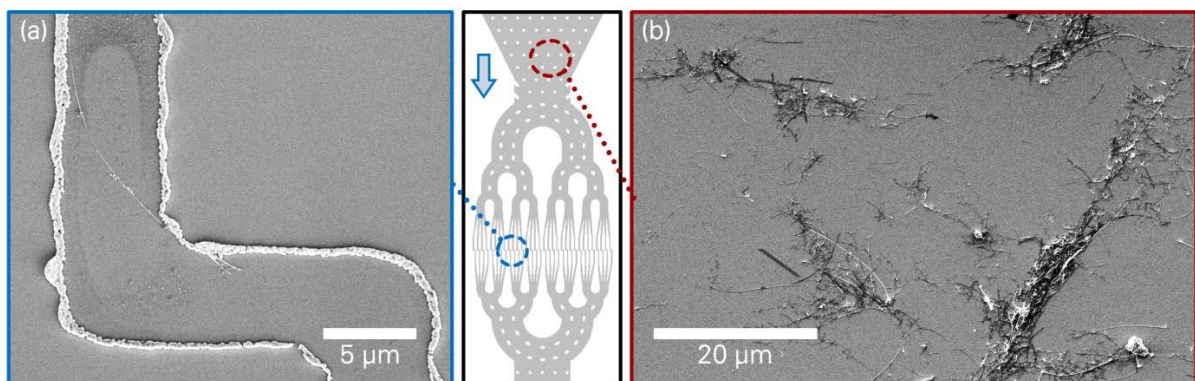
Fig. 5.10: Outcome of alignment and trapping experiments using SiNW suspensions fabricated according to the production scheme schematically depicted in Fig. 5.9. (a) SiNW of ~ 14 μm length deposited at NW trapping site. The former positions of the microfluidic channel walls are readily identifiable due to the debris left behind by the isopropanol-based suspension. (b) NW agglomerations observed at the inlet of the flow structure. The locations of the two spots depicted in (a) and (b) on the receiver substrate are circled in blue and red, respectively, in the image of the flow structure in the middle of the figure. Blue arrow indicates NW suspension flow direction.

Fig. 5.10a also illustrates that large amounts of debris are left on the receiver substrate near the channel walls. Due to the sonication of the substrates during harvesting the SiNWs, it is not possible to determine the origin of the debris. Any previous contaminants of the growth substrate surface could be included in it, such as flakes of amorphous Si formed as undesired side product during SiNW growth.[202]

Due to the low yield of SiNWs deposited at the trapping sites and due to the risk of cross contaminating the clean room devices of the NaMLab gGmbH, because of the debris on the surface, the samples produced from the "homemade" SiNW suspension are not further processed.

For future experiments, the stiffness of the NWs must be increased to obtain better alignment and trapping results. Since the SiNWs fabricated within this work are much thinner (~ 20 nm) than the utilized commercial SiNWs (~ 150 nm), increasing the NW thickness may be one possibility to reduce their flexibility. Furthermore, the application of shorter NWs in combination with a narrower channel width and a reduced channel height at the trapping sites, could enhance the trapping yield. Shorter NWs are expected to show less entanglement at the inlet area (see Fig. 5.10b). The trapping site geometry has to be adjusted accordingly. However, as further discussed in section 5.5, adjustments to the channel dimensions have to be done with great care.

5.4.3 Polydisperse CuO NW suspensions

To verify the applicability of the developed NW positioning method with NWs of another type of material, polydisperse suspensions from CuO NWs are prepared. In the literature, CuO NWs are proven to yield p-type field-effect transistors and CO gas sensors.[280]

Within this work, CuO NWs are grown via oxidation of Cu foil (99,9% Cu content, RCT®-ANT-99.9, Reichelt Chemietechnik GmbH + Co., Germany) at 500 °C in air for 12 h,[281] and dispersed in isopropanol via sonication. Fig. 5.11 shows the NWs on the growth substrate and after their deposition on a Si wafer from a drop of NW suspension. Both images show that CuO NWs of at least 20 µm length are grown. However, also large portions of shorter NW pieces go into suspension.

The CuO NW suspensions are diluted 1:1 (vol./vol.) with deionized water directly before applying up to 20 µl of sample volume in the alignment and trapping set-up depicted in Fig. 5.4b. For contacting
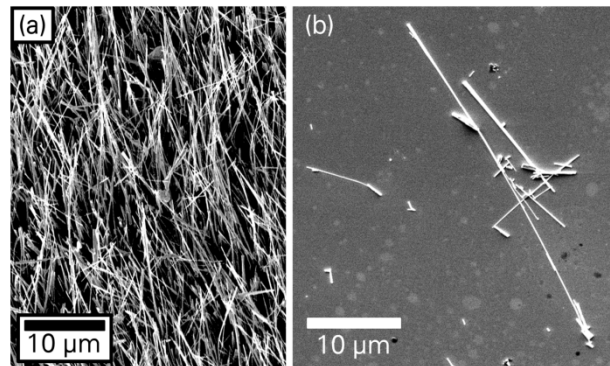

Fig. 5.11: Growth and harvesting of CuO NWs. SEM images of (a) CuO NW forest on growth substrate, (b) CuO NWs deposited on Si wafer surface from isopropanol-based suspension.

the deposited CuO NWs, Cr/Au electrodes (5 nm/110 nm, UNIVEX 300, Oerlikon Leybold Vaccum) are used. After UVL using AZ5214e image reversal photoresist as negative resist, metal deposition and lift-off in acetone, the samples are rinsed with isopropanol and dried under a stream of N_2.

Fig. 5.12a shows a representative image of a CuO NW trapped and contacted with the presented approach. The plot in Fig. 5.12b demonstrates the *p*-type behavior of the CuO single-NW FET. The

Fig. 5.12: (a) SEM image of a back-gated single CuO NW FET fabricated with the developed approach. (b) I_{SD}-V_{SD} characteristics of the device shown in Fig. 5.12a at different gate voltages: orange circles, black squares, blue diamonds correspond to V_{BG} = -40 V, 0 V, 40 V respectively.

on-current of 0.39 nA is in good agreement with the characteristics of other CuO NW devices in literature.[280]

Compared to the commercial SiNWs, less single-NW FETs per chip are obtained when using the CuO NWs. This is attributed to the polydispersity of the CuO NWs in the obtained suspension as well as to the fact that a large proportion of the CuO NWs is significantly shorter than the 20 µm-long commercial SiNWs.

Compared to the "homemade" SiNWs, the CuO NWs show no such entanglement as depicted in Fig. 5.10b. The CuO NWs appear to be much stiffer which is attributed to their thickness of ~ 150 .. 200 nm. This indicates that increasing the thickness and, thus, the stiffness of the 1D nanostructures results in better trapping behavior.

5.5 POSSIBLE FUTURE TUNING OF SINGLE-NW FET YIELD

The results show that a monodisperse NW solution with stiff NWs more likely yields single-NW devices. It is assumed, that the NW concentration in the suspensions, the flow velocity at the trapping sites as well as the channel width and height at the trapping sites are also important parameters that influence the yield of single-NW devices.

In case of the trapping site geometry, reducing the channel height will guide the NWs closer to the receiver substrate surface on the bottom of the channel. This way they are more likely to assemble on the receiver substrate surface over their entire length, reducing the probability of receiving devices with no attached NWs. However, the probability of receiving devices with more than one NW is increased.

Reducing the channel width will decrease the amount of trapping sites where two or more neighboring NWs are deposited. However, reducing the channel dimensions, *i. e.* width and height, respectively, will make the system prone to clogging. This highlights that there is a
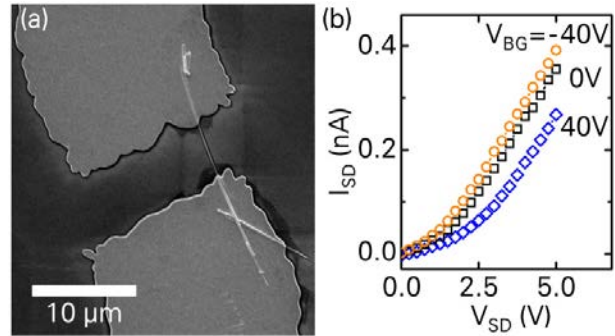
delicate interplay of channel width and height towards the effective deposition of single-NW devices.

5.6 CONCLUSION

The results of this chapter demonstrate the successful development of a continuous-flow microfluidics-based approach for the alignment, trapping and deposition of single NWs at designated positions, without limitations regarding NW materials. Crucial parameters for the alignment and trapping outcome are the stiffness and the length of the 1D nanostructures as well as the layout and the dimensions of the trapping sites. The option to use standard UVL for contacting the NWs renders the process cost-efficient and attractive for large scale applications. The fact that microfluidic channels with hundreds and thousands of trapping sites have been built for single-particle [56] and single-cell studies,[57] respectively, illustrates the upscaling opportunities of the presented method.

Within the scope of this thesis, in the field of chemo- and biosensing, large-scale arrays of single-NW devices are considered a seminal step towards a highly sensitive multiplexed detection of large amounts of analytes, with enhanced properties compared to *e. g.* DNA microarrays.[196] Generally, as the positioning of 1D nanostructures can be fully controlled, the developed approach represents a simple, yet precise and versatile tool for integrating 1D bottom-up building blocks with their unique properties into top-down technology.

The single-NW devices assembled within this work are not passivated with a dielectric film (see section 4.2.4), so that they are not used for sensing applications in aqueous environments *via* liquid gate (see sections 4.3.3 and 4.3.4). Instead, they are used for memristive sensing [282] in a back-gate arrangement by B. Ibarlucea.

FINAL CONCLUSION AND OUTLOOK

Within this thesis, various innovative concepts for the fabrication of LoC analysis devices are developed and successfully applied. Step by step, the respective achievements of the different chapters finally result in a facile fabrication of SiNW-based biosensors.

The sensing devices are comprised of a microfluidic system the channel layouts of which are readily adaptable to all kinds of flow requirements, as demonstrated in chapter 2. SiNW-based FETs are the signal transducing backbone of the biosensors. Implemented into the microfluidic channels, they show high pH sensitivities near the Nernst limit (see chapter 4). In order to exploit their sensitivities for biosensing purposes, the NWs are functionalized using a TESPSA-based surface modification approach, developed in chapter 3, which allows for a simple attachment of analyte-specific receptor molecules. In the final set-up, immobilized antibodies enable distinguishing between the unspecific analyte, HA peptide, which induces no signal changes and the specific analyte, IgG_{Target_green}, which is detected with varying sensitivities of $S_{IgG\_Target\_green} \approx$ -8 .. -14 mV/dec at concentrations beyond $c_{IgG\_Target\_green}$ = 1 nM. As a means to diminish device-to-device variations and to increase device sensitivities, in chapter 5, a continuous-flow microfluidics-based NW alignment and trapping procedure for reliably fabricating single-SiNW FETs is developed.

Beyond focusing on the assembly of SiNW devices, the developed techniques are utilized for exploring several additional applications. The reversible sealability , ranging from (i) the fabrication of flexible electronic interconnects and uniquely shaped 3D polymer microstructures with possible applications in cell culturing (chapter 2) over (ii) the patterned immobilization of AuNPs and patterned surface wettabilities for passively controlling the behavior of liquids (chapter 3) to (iii) the implementation of different kinds of NW materials into single-NW FETs.

Currently, the presented techniques are further applied and adjusted for (i) assembling the microfluidics of localized SPR devices, (ii) functionalizing SiNW-based sensors similar to the ones presented in chapter 4 and (iii) memristive single-SiNW-based sensing. In summary, the achievements of this thesis are considered a very versatile, useful toolbox for future scientific investigations and further engineering of facile LoC built-ups, not only in the field of SiNW-based biosensing but also in the greater field of bionanotechnology.

REFERENCES

1.   R. S. Yalow, S. A. Berson. Immunoassay of endogenous plasma insulin in man. *J Clin Invest* **39** (1960) 1157–1175.

2.   S. D. Gan, K. R. Patel. Enzyme Immunoassay and Enzyme-Linked Immunosorbent Assay. *J Invest Dermatol* **133** (2013) 1–3.

3.   R. K. Saiki, S. Scharf, F. Faloona, K. B. Mullis, G. T. Horn, H. A. Erlich, N. Arnheim. Enzymatic amplification of beta-globin genomic sequences and restriction site analysis for diagnosis of sickle cell anemia. *Science* **230** (1985) 1350–1354.

4.   M. Botes, M. de Kwaadsteniet, T. E. Cloete. Application of quantitative PCR for the detection of microorganisms in water. *Anal Bioanal Chem* **405** (2012) 91–108.

5.   J. P. Santos, T. Arroyo, M. Aleixandre, J. Lozano, I. Sayago, M. García, M. J. Fernández, L. Arés, J. Gutiérrez, J. M. Cabellos, M. Gil, M. C. Horrillo. A comparative study of sensor array and GC–MS: application to Madrid wines characterization. *Sens Actuators B Chem* **102** (2004) 299–307.

6.   H. Cheng, Z. H. Qin, X. F. Guo, X. S. Hu, J. H. Wu. Geographical origin identification of propolis using GC–MS and electronic nose combined with principal component analysis. *Food Res Int* **51** (2013) 813–822.

7.   O. Geschke [Ed.]. *Microsystem engineering of lab on a chip devices*. Wiley-VCH, 2008.

8.   S. C. Terry, J. H. Jerman, J. B. Angell. A gas chromatographic air analyzer fabricated on a silicon wafer. *IEEE Trans Electron Devices* **26** (1979) 1880–1886.

9.   A. Manz, N. Graber, H. M. Widmer. Miniaturized total chemical analysis systems: A novel concept for chemical sensing. *Sens Actuators B Chem* **1** (1990) 244–248.

10. A. K. Au, H. Lai, B. R. Utela, A. Folch. Microvalves and Micropumps for BioMEMS. *Micromachines* **2** (2011) 179–220.

11. A. R. Abate, M. B. Romanowsky, J. J. Agresti, D. A. Weitz. Valve-based flow focusing for drop formation. *Appl Phys Lett* **94** (2009) 023503.

12. L. Wang, L. A. Flanagan, N. L. Jeon, E. Monuki, A. P. Lee. Dielectrophoresis switching with vertical sidewall electrodes for microfluidic flow cytometry. *Lab Chip* **7** (2007) 1114.

13. N.-T. Nguyen, Z. Wu. Micromixers - a review. *J Micromech Microeng* **15** (2005) R1–R16.

14. D. C. Duffy, O. J. Schueller, S. T. Brittain, G. M. Whitesides. Rapid prototyping of microfluidic switches in poly (dimethyl siloxane) and their actuation by electro-osmotic flow. *J Micromech Microeng* **9** (1999) 211.

15. D. J. Sadler, R. Changrani, P. Roberts, Chia-Fu Chou, F. Zenhausern. Thermal management of BioMEMS: Temperature control for ceramic-based PCR and DNA detection devices. *IEEE Trans Compon Packag Technol* **26** (2003) 309–316.

16. G. M. Whitesides. The origins and the future of microfluidics. *Nature* **442** (2006) 368–373.

17. H. A. Stone, A. D. Stroock, A. Ajdari. Engineering Flows in Small Devices. *Annu Rev Fluid Mech* **36** (2004) 381–411.

18. D. R. Shankaran, K. V. Gobi, N. Miura. Recent advancements in surface plasmon resonance immunosensors for detection of small molecules of biomedical, food and environmental interest. *Sens Actuators B Chem* **121** (2007) 158–177.

19. Y. Cui, Q. Wei, H. Park, C. M. Lieber. Nanowire Nanosensors for Highly Sensitive and Selective Detection of Biological and Chemical Species. *Science* **293** (2001) 1289–1292.

20. P. Bergveld. Development of an Ion-Sensitive Solid-State Device for Neurophysiological Measurements. *IEEE Trans Biomed Eng* **BME-17** (1970) 70–71.

21. P. J. Conroy, S. Hearty, P. Leonard, R. J. O'Kennedy. Antibody production, design and use for biosensor-based applications. *Semin Cell Dev Biol* **20** (2009) 10–26.

22. E. Stern, J. F. Klemic, D. A. Routenberg, P. N. Wyrembak, D. B. Turner-Evans, A. D. Hamilton, D. A. LaVan, T. M. Fahmy, M. A. Reed. Label-free immunodetection with CMOS-compatible semiconducting nanowires. *Nature* **445** (2007) 519–522.

23. G. Zheng, C. M. Lieber. Nanowire Biosensors for Label-Free, Real-Time, Ultrasensitive Protein Detection. *Methods Mol Biol* **790** (2011) 223–237.

24. G. Zheng, F. Patolsky, Y. Cui, W. U. Wang, C. M. Lieber. Multiplexed electrical detection of cancer markers with nanowire sensor arrays. *Nat Biotech* **23** (2005) 1294–1301.

25. Z. Li, Y. Chen, X. Li, T. I. Kamins, K. Nauka, R. S. Williams. Sequence-Specific Label-Free DNA Sensors Based on Silicon Nanowires. *Nano Lett* **4** (2004) 245–247.

26. E. Baldrich. *Recognition Receptors in Biosensors*. Springer, 2010. 675–722.

27. L. Römhildt, C. Pahlke, F. Zörgiebel, H.-G. Braun, J. Opitz, L. Baraban, G. Cuniberti. Patterned Biochemical Functionalization Improves Aptamer-Based Detection of Unlabeled Thrombin in a Sandwich Assay. *ACS Appl Mater Interfaces* **5** (2013) 12029–12035.

28. F. M. Zörgiebel, S. Pregl, L. Römhildt, J. Opitz, W. Weber, T. Mikolajick, L. Baraban, G. Cuniberti. Schottky barrier-based silicon nanowire pH sensor with live sensitivity control. *Nano Res* **7** (2014) 263–271.

29. S. Chen, J. G. Bomer, E. T. Carlen, A. van den Berg. Al_2O_3/Silicon NanoISFET with Near Ideal Nernstian Response. *Nano Lett* **11** (2011) 2334–2341.

30. L. Luo, J. Jie, W. Zhang, Z. He, J. Wang, G. Yuan, W. Zhang, C. Wu, S. Lee. Silicon nanowire sensors for Hg^{2+} and Cd^{2+} ions. *Appl Phys Lett* **94** (2009) 193101.

31. X. Bi, A. Agarwal, K.-L. Yang. Oligopeptide-modified silicon nanowire arrays as multichannel metal ion sensors. *Biosens Bioelectron* **24** (2009) 3248–3251.

32. J. Li, Y. Zhang, S. To, L. You, Y. Sun. Effect of Nanowire Number, Diameter, and Doping Density on Nano-FET Biosensor Sensitivity. *ACS Nano* **5** (2011) 6661–6668.

33. F. Patolsky, G. Zheng, C. M. Lieber. Nanowire-Based Biosensors. *Anal. Chem.* **78** (2006) 4260–4269.

34. J. Hahm, C. M. Lieber. Direct Ultrasensitive Electrical Detection of DNA and DNA Sequence Variations Using Nanowire Nanosensors. *Nano Lett.* **4** (2004) 51–54.

35. F. Patolsky, G. Zheng, O. Hayden, M. Lakadamyali, X. Zhuang, C. M. Lieber. Electrical detection of single viruses. *PNAS* **101** (2004) 14017–14022.

36. D. D. D. Ma, C. S. Lee, F. C. K. Au, S. Y. Tong, S. T. Lee. Small-Diameter Silicon Nanowire Surfaces. *Science* **299** (2003) 1874–1877.

37. C. X. Wang, M. Hirano, H. Hosono. Origin of Diameter-Dependent Growth Direction of Silicon Nanowires. *Nano Lett* **6** (2006) 1552–1555.

38. Y. Wu, Y. Cui, L. Huynh, C. J. Barrelet, D. C. Bell, C. M. Lieber. Controlled Growth and Structures of Molecular-Scale Silicon Nanowires. *Nano Lett* **4** (2004) 433–436.

39. Y. Cui, Z. Zhong, D. Wang, W. U. Wang, C. M. Lieber. High Performance Silicon Nanowire Field Effect Transistors. *Nano Lett* **3** (2003) 149–152.

40. D. Karnaushenko, B. Ibarlucea, S. Lee, G. Lin, L. Baraban, S. Pregl, M. Melzer, D. Makarov, W. M. Weber, T. Mikolajick, O. G. Schmidt, G. Cuniberti. Light Weight and Flexible High-Performance Diagnostic Platform. *Adv Healthcare Mater* **4** (2015) 1517–1525.

41. M. J. Madou. *Fundamentals of Microfabrication: The Science of Miniaturization, Second Edition*. CRC Press, 2002.

42. *Fotolithografie - Theorie und Anwendung von Fotolacken, Entwicklern, Ätzchemikalien und Lösemitteln*. MicroChemicals GmbH, 2012.

43. I. E. Araci, P. Brisk. Recent developments in microfluidic large scale integration. *Curr Opin Biotechnol* **25** (2014) 60–68.

44. J. Melin, S. R. Quake. Microfluidic Large-Scale Integration: The Evolution of Design Rules for Biological Automation. *Annu Rev Biophys Biomol Struct* **36** (2007) 213–231.

45. D. Mark, S. Haeberle, G. Roth, F. von Stetten, R. Zengerle. Microfluidic lab-on-a-chip platforms: requirements, characteristics and applications. *Chem Soc Rev* **39** (2010) 1153.

46. P. J. Hung, P. J. Lee, P. Sabounchi, R. Lin, L. P. Lee. Continuous perfusion microfluidic cell culture array for high-throughput cell-based assays. *Biotechnol Bioeng* **89** (2005) 1–8.

47. A. R. Wheeler, W. R. Throndset, R. J. Whelan, A. M. Leach, R. N. Zare, Y. H. Liao, K. Farrell, I. D. Manger, A. Daridon. Microfluidic Device for Single-Cell Analysis. *Anal Chem* **75** (2003) 3581–3586.

48. E. A. Lipman, B. Schuler, O. Bakajin, W. A. Eaton. Single-Molecule Measurement of Protein Folding Kinetics. *Science* **301** (2003) 1233–1235.

49. T. Thorsen, R. W. Roberts, F. H. Arnold, S. R. Quake. Dynamic Pattern Formation in a Vesicle-Generating Microfluidic Device. *Phys Rev Lett* **86** (2001) 4163–4166.

50. S. L. Anna, N. Bontoux, H. A. Stone. Formation of dispersions using 'flow focusing' in microchannels. *Appl Phys Lett* **82** (2003) 364–366.

51. E. Tumarkin, E. Kumacheva. Microfluidic generation of microgels from synthetic and natural polymers. *Chem Soc Rev* **38** (2009) 2161.

52. S. Seiffert, D. A. Weitz. Microfluidic fabrication of smart microgels from macromolecular precursors. *Polymer* **51** (2010) 5883–5889.

53. S. S. Datta, A. Abbaspourrad, E. Amstad, J. Fan, S.-H. Kim, M. Romanowsky, H. C. Shum, B. Sun, A. S. Utada, M. Windbergs, S. Zhou, D. A. Weitz. 25th Anniversary Article: Double Emulsion Templated Solid Microcapsules: Mechanics And Controlled Release. *Adv Mater* **26** (2014) 2205–2218.

54. Y. Yu, H. Wen, J. Ma, S. Lykkemark, H. Xu, J. Qin. Flexible Fabrication of Biomimetic Bamboo-Like Hybrid Microfibers. *Adv Mater* **26** (2014) 2494–2499.

55. J. Thiele, M. Windbergs, A. R. Abate, M. Trebbin, H. C. Shum, S. Förster, D. A. Weitz. Early development drug formulation on a chip: Fabrication of nanoparticles using a microfluidic spray dryer. *Lab Chip* **11** (2011) 2362–2368.

56. W.-H. Tan, S. Takeuchi. A trap-and-release integrated microfluidic system for dynamic microarray applications. *PNAS* **104** (2007) 1146–1151.

57. A. M. Skelley, O. Kirak, H. Suh, R. Jaenisch, J. Voldman. Microfluidic control of cell pairing and fusion. *Nat Meth* **6** (2009) 147–152.

58. K. Churski, T. S. Kaminski, S. Jakiela, W. Kamysz, W. Baranska-Rybak, D. B. Weibel, P. Garstecki. Rapid screening of antibiotic toxicity in an automated microdroplet system. *Lab Chip* **12** (2012) 1629.

59. P. S. Dittrich, A. Manz. Lab-on-a-chip: microfluidics in drug discovery. *Nat Rev Drug Discov* **5** (2006) 210–218.

60. S. K. Sia, G. M. Whitesides. Microfluidic devices fabricated in Poly(dimethylsiloxane) for biological studies. *Electrophoresis* **24** (2003) 3563–3576.

61. E. K. Sackmann, A. L. Fulton, D. J. Beebe. The present and future role of microfluidics in biomedical research. *Nature* **507** (2014) 181–189.

62. D. J. Laser, J. G. Santiago. A review of micropumps. *J Micromech Microeng* **14** (2004) R35.

63. A. Günther, M. Jhunjhunwala, M. Thalmann, M. A. Schmidt, K. F. Jensen. Micromixing of Miscible Liquids in Segmented Gas–Liquid Flow. *Langmuir* **21** (2005) 1547–1555.

64. N.-T. Nguyen. *Micromixers: Fundamentals, Design and Fabrication*. William Andrew, 2011.

65. X.-M. Zhao, Y. Xia, G. M. Whitesides. Soft lithographic methods for nano-fabrication. *J Mater Chem* **7** (1997) 1069–1074.

66. D. C. Duffy, J. C. McDonald, O. J. A. Schueller, G. M. Whitesides. Rapid Prototyping of Microfluidic Systems in Poly(dimethylsiloxane). *Anal Chem* **70** (1998) 4974–4984.

67. N. Li, C.-H. Hsu, A. Folch. Parallel mixing of photolithographically defined nanoliter volumes using elastomeric microvalve arrays. *Electrophoresis* **26** (2005) 3758–3764.

68. Y. Lee, Y. Lim, H. Shin. Mixed-Scale Channel Networks Including Kingfisher-Beak-Shaped 3D Microfunnels for Efficient Single Particle Entrapment. *Nanoscale* (2016) 11810–11817.

69. Y. Xia, G. M. Whitesides. Soft lithography. *Annu Rev Mater Sci* **28** (1998) 153–184.

70. M. Rafat, D. R. Raad, A. C. Rowat, D. T. Auguste. Fabrication of reversibly adhesive fluidic devices using magnetism. *Lab Chip* **9** (2009) 3016.

71. E. J. Wong. *Modeling and Control of Rapid Cure in Polydimethylsiloxan (PDMS) for Microfluidic Device Applications*. Massachusetts Institute of Technology, 2010.

72. J. N. Lee, C. Park, G. M. Whitesides. Solvent Compatibility of Poly(dimethylsiloxane)-Based Microfluidic Devices. *Anal Chem* **75** (2003) 6544–6554.

73. J. C. McDonald, G. M. Whitesides. Poly(dimethylsiloxane) as a Material for Fabricating Microfluidic Devices. *Acc Chem Res* **35** (2002) 491–499.

74. V. Saarela, S. Franssila, S. Tuomikoski, S. Marttila, P. Östman, T. Sikanen, T. Kotiaho, R. Kostiainen. Re-usable multi-inlet PDMS fluidic connector. *Sens Actuators B Chem* **114** (2006) 552–557.

75. A. Konda, J. M. Taylor, M. A. Stoller, S. A. Morin. Reconfigurable microfluidic systems with reversible seals compatible with 2D and 3D surfaces of arbitrary chemical composition. *Lab Chip* **15** (2015) 2009–2017.

76. Z. Yang, R. Maeda. Socket with built-in valves for the interconnection of microfluidic chips to macro constituents. *J Chromatogr A* **1013** (2003) 29–33.

77. Q. Chen, G. Li, Y. Nie, S. Yao, J. Zhao. Investigation and improvement of reversible microfluidic devices based on glass-PDMS-glass sandwich configuration. *Microfluid Nanofluid* **16** (2013) 83–90.

78. M. Le Berre, C. Crozatier, G. Velve Casquillas, Y. Chen. Reversible assembling of microfluidic devices by aspiration. *Microelectron Eng* **83** (2006) 1284–1287.

79. H. Song, D. L. Chen, R. F. Ismagilov. Reactions in Droplets in Microfluidic Channels. *Angew Chem Int Ed Engl* **45** (2006) 7336–7356.

80. J. Leng, J.-B. Salmon. Microfluidic crystallization. *Lab Chip* **9** (2009) 24–34.

81. L. Li, R. F. Ismagilov. Protein Crystallization Using Microfluidic Technologies Based on Valves, Droplets, and SlipChip. *Annu Rev Biophys* **39** (2010) 139–158.

82. L. Mazutis, J. Gilbert, W. L. Ung, D. A. Weitz, A. D. Griffiths, J. A. Heyman. Single-cell analysis and sorting using droplet-based microfluidics. *Nat Protocols* **8** (2013) 870–891.

83. A. M. Klein, L. Mazutis, I. Akartuna, N. Tallapragada, A. Veres, V. Li, L. Peshkin, D. A. Weitz, M. W. Kirschner. Droplet Barcoding for Single-Cell Transcriptomics Applied to Embryonic Stem Cells. *Cell* **161** (2015) 1187–1201.

84. Y. Zhang, P. Ozdemir. Microfluidic DNA amplification - A review. *Anal Chim Acta* **638** (2009) 115–125.

85. M. Margulies *et al.* Genome sequencing in microfabricated high-density picolitre reactors. *Nature* **437** (2005) 376–380.

86. B. L. Wang, A. Ghaderi, H. Zhou, J. Agresti, D. A. Weitz, G. R. Fink, G. Stephanopoulos. Microfluidic high-throughput culturing of single cells for selection based on extracellular metabolite production or consumption. *Nat Biotech* **32** (2014) 473–478.

87. S.-Y. Teh, R. Lin, L.-H. Hung, A. P. Lee. Droplet microfluidics. *Lab Chip* **8** (2008) 198.

88. D. Bardin, T. D. Martz, P. S. Sheeran, R. Shih, P. A. Dayton, A. P. Lee. High-speed, clinical-scale microfluidic generation of stable phase-change droplets for gas embolotherapy. *Lab Chip* **11** (2011) 3990–3998.

89. D. R. Link, E. Grasland-Mongrain, A. Duri, F. Sarrazin, Z. Cheng, G. Cristobal, M. Marquez, D. A. Weitz. Electric Control of Droplets in Microfluidic Devices. *Angew Chem Int Ed Engl* **45** (2006) 2556–2560.

90. R. B. Fair. Digital microfluidics: is a true lab-on-a-chip possible? *Microfluid Nanofluid* **3** (2007) 245–281.

91. P. Garstecki, M. J. Fuerstman, H. A. Stone, G. M. Whitesides. Formation of droplets and bubbles in a microfluidic T-junction - scaling and mechanism of break-up. *Lab Chip* **6** (2006) 437–446.

92. L. Bell, A. Seshia, D. Lando, E. Laue, M. Palayret, S. F. Lee, D. Klenerman. A microfluidic device for the hydrodynamic immobilisation of living fission yeast cells for super-resolution imaging. *Sens Actuators B Chem* **192** (2014) 36–41.

93. J. Bardeen, W. H. Brattain. The transistor, a semi-conductor triode. *Phys Rev* **74** (1948) 230.

94. D. Hutcheson. Transistors, by the Numbers: A look at Moore's Law in action. *IEEE Spectrum* **52** (2015) 31.

95. G. Q. Zhang, A. van Roosmalen. *More than Moore: Creating High Value Micro/Nanoelectronics Systems.* Springer Science & Business Media, 2010.

96. J.-P. Colinge, C. A. Colinge. *Physics of semiconductor devices.* Springer Science & Business Media, 2005.

97. S. G. Burns, P. R. Bond. *Principles of electronic circuits.* PWS Publishing Company, 1997.

98. P. Bergveld. Thirty years of ISFETOLOGY: What happened in the past 30 years and what may happen in the next 30 years. *Sens Actuators B Chem* **88** (2003) 1–20.

99. S. M. Sze, K. K. Ng. *Physics of Semiconductor Devices.* John Wiley & Sons, Inc., 2006.

100. T. W. Healy, L. R. White. Ionizable surface group models of aqueous interfaces. *Adv Colloid Interface Sci* **9** (1978) 303–345.

101. D. E. Yates, S. Levine, T. W. Healy. Site-binding model of the electrical double layer at the oxide/water interface. *J Chem Soc, Faraday Trans 1* **70** (1974) 1807–1818.

102. R. E. G. van Hal, J. C. T. Eijkel, P. Bergveld. A general model to describe the electrostatic potential at electrolyte oxide interfaces. *Adv Colloid Interface Sci* **69** (1996) 31–62.

103. A. van den Berg, P. Bergveld, D. N. Reinhoudt, E. J. Sudhölter. Sensitivity control of ISFETs by chemical surface modification. *Sens Actuators* **8** (1985) 129–148.

104. L. Bousse, N. F. De Rooij, P. Bergveld. Operation of chemically sensitive field-effect sensors as a function of the insulator-electrolyte interface. *IEEE Trans Electron Devices* **30** (1983) 1263–1270.

105. S. Zafar, C. D'Emic, A. Afzali, B. Fletcher, Y. Zhu, T. Ning. Optimization of pH sensing using silicon nanowire field effect transistors with HfO_2 as the sensing surface. *Nanotechnology* **22** (2011) 405501.

106. H. Perrot, N. Jaffrezic-Renault, N. F. De Rooij, H. H. Van Den Vlekkert. Ionic detection using differential measurement between an ion-sensitive FET and a reference FET. *Sens Actuators* **20** (1989) 293–299.

107. T. Rim, M. Meyyappan, C.-K. Baek. Optimized operation of silicon nanowire field effect transistor sensors. *Nanotechnology* **25** (2014) 505501.

108. A. Tarasov, M. Wipf, R. L. Stoop, K. Bedner, W. Fu, V. A. Guzenko, O. Knopfmacher, M. Calame, C. Schönenberger. Understanding the Electrolyte Background for Biochemical Sensing with Ion-Sensitive Field-Effect Transistors. *ACS Nano* **6** (2012) 9291–9298.

109. A. Tarasov, M. Wipf, K. Bedner, J. Kurz, W. Fu, V. A. Guzenko, O. Knopfmacher, R. L. Stoop, M. Calame, C. Schönenberger. True Reference Nanosensor Realized with Silicon Nanowires. *Langmuir* **28** (2012) 9899–9905.

110. A. Heinzig, T. Mikolajick, J. Trommer, D. Grimm, W. M. Weber. Dually Active Silicon Nanowire Transistors and Circuits with Equal Electron and Hole Transport. *Nano Lett* **13** (2013) 4176–4181.

111. R. T. Tung. Schottky-Barrier Formation at Single-Crystal Metal-Semiconductor Interfaces. *Phys Rev Lett* **52** (1984) 461–464.

112. A. Heinzig, S. Slesazeck, F. Kreupl, T. Mikolajick, W. M. Weber. Reconfigurable Silicon Nanowire Transistors. *Nano Lett* **12** (2012) 119–124.

113. W. Füssel, M. Schmidt, H. Angermann, G. Mende, H. Flietner. Defects at the Si/SiO_2 interface: Their nature and behaviour in technological processes and stress. *Nucl Instrum Methods Phys Res Sect A* **377** (1996) 177–183.

114. I. Lundström, S. Christensson, C. Svensson. Carrier trapping hysteresis in MOS transistors. *Phys Stat Sol A* **1** (1970) 395–407.

115. F. P. Heiman, G. Warfield. The effects of oxide traps on the MOS capacitance. *IEEE Trans Electron Devices* **12** (1965) 167–178.

116. D. M. Fleetwood. Fast and slow border traps in MOS devices. *Third European IEEE Conference on RADECS 95.* 1995. 1–8.

117. T. L. Tewksbury, H. S. Lee, G. A. Miller. The effects of oxide traps on the large-signal transient response of analog MOS circuits. *IEEE J Solid-State Circuits* **24** (1989) 542–544.

118. W. Olthuis, P. Bergveld. On the charge storage and decay mechanism in silicon dioxide electrets. *IEEE Trans Electr Insul* **27** (1992) 691–697.

119. E. H. Nicollian, C. N. Berglund, P. F. Schmidt, J. M. Andrews. Electrochemical Charging of Thermal SiO_2 Films by Injected Electron Currents. *J Appl Phys* **42** (1971) 5654–5664.

120. W. M. Weber. *Silicon to Nickel Silicide Longitudinal Nanowire Heterostructures: Synthesis, Electrical Characterization and Novel Devices*. Technische Universität München, 2008.

121. B. Nagel, H. Dellweg, L. M. Gierasch. *Glossary for Chemists of Terms Used in Biotechnology (IUPAC Recommendations 1992)*. International Union of Pure and Applied Chemistry, Applied Chemistry Division, Commission on Biotechnology, 1992.

122. J. Cooper, T. Cass. *Biosensors*. Oxford University Press, 2004.

123. B. R. Eggins. *Biosensors: an Introduction*. Springer, 2013.

124. M. Zourob [Ed.]. *Recognition Receptors in Biosensors*. Springer, 2010.

125. J. Wang. Electrochemical biosensors: Towards point-of-care cancer diagnostics. *Biosens Bioelectron* **21** (2006) 1887–1892.

126. F. Rusmini, Z. Zhong, J. Feijen. Protein Immobilization Strategies for Protein Biochips. *Biomacromolecules* **8** (2007) 1775–1789.

127. R. Reverberi, L. Reverberi. Factors affecting the antigen-antibody reaction. *Blood Transfus* **5** (2007) 227–240.

128. E. Harlow, D. Lane. *Using Antibodies: A Laboratory Manual*. CSHL Press, 1999.

129. G. Gilardi. *Protein engineering for biosensors, in "Biosensors 2nd Edition" J. Cooper and A. E. G. Cass [Eds.]*. Oxford University Press, 2004.

130. L. Gorton, E. Csöregi, E. Domínguez, J. Emnéus, G. Jönsson-Pettersson, G. Marko-Varga, B. Persson. Selective detection in flow analysis based on the combination of immobilized enzymes and chemically modified electrodes. *Anal Chim Acta* **250** (1991) 203–248.

131. C. W. Park, C. S. Ah, C.-G. Ahn, J.-H. Yang, A. Kim, T.-Y. Kim, G. Y. Sung. Analysis of configuration of surface-immobilized proteins by Si nanochannel field effect transistor biosensor. *Sens Actuators B Chem* **154** (2011) 164–168.

132. N. Jing, R. F. Rando, Y. Pommier, M. E. Hogan. Ion Selective Folding of Loop Domains in a Potent Anti-HIV Oligonucleotide. *Biochemistry* **36** (1997) 12498–12505.

133. J. Figueroa, S. Magaña, D. V. Lim, R. Schlaf. Antibody immobilization using pneumatic spray: Comparison with the avidin–biotin bridge immobilization method. *J Immunol Methods* **386** (2012) 1–9.

134. A. K. Trilling, J. Beekwilder, H. Zuilhof. Antibody orientation on biosensor surfaces: a minireview. *Analyst* **138** (2013) 1619.

135. J.-W. Park, I.-H. Cho, D. W. Moon, S.-H. Paek, T. G. Lee. ToF-SIMS and PCA of surface-immobilized antibodies with different orientations. *Surf Interface Anal* **43** (2011) 285–289.

136. D. P. Nitsche-Schmitz, H. M. Johansson, I. Sastalla, S. Reissmann, I.-M. Frick, G. S. Chhatwal. Group G Streptococcal IgG Binding Molecules FOG and Protein G Have Different Impacts on Opsonization by C1q. *J Biol Chem* **282** (2007) 17530–17536.

137. F. D. Lowy. Staphylococcus aureus Infections. *N Engl J Med* **339** (1998) 520–532.

138. D. M. Gersten, J. J. Marchalonis. A rapid, novel method for the solid-phase derivatization of IgG antibodies for immune-affinity chromatography. *J Immunol Methods* **24** (1978) 305–309.

139. J. Turková. Oriented immobilization of biologically active proteins as a tool for revealing protein interactions and function. *J Chromatogr B Biomed Sci Appl* **722** (1999) 11–31.

140. E. L. Schmid, T. A. Keller, Z. Dienes, H. Vogel. Reversible oriented surface immobilization of functional proteins on oxide surfaces. *Anal Chem* **69** (1997) 1979–1985.

141. C. Boozer, J. Ladd, S. Chen, S. Jiang. DNA-Directed Protein Immobilization for Simultaneous Detection of Multiple Analytes by Surface Plasmon Resonance Biosensor. *Anal Chem* **78** (2006) 1515–1519.

142. B. G. Kopek. *Structure, Organization, and Formation of the Flock House Virus RNA Replication Complex.* ProQuest, 2008.

143. M. Reth. Matching cellular dimensions with molecular sizes. *Nat Immunol* **14** (2013) 765–767.

144. S. Fiorilli, P. Rivolo, E. Descrovi, C. Ricciardi, L. Pasquardini, L. Lunelli, L. Vanzetti, C. Pederzolli, B. Onida, E. Garrone. Vapor-phase self-assembled monolayers of aminosilane on plasma-activated silicon substrates. *J Colloid Interface Sci* **321** (2008) 235–241.

145. B. Arkles. *Silane Coupling Agents: Connecting Across Boundaries.* Gelest Inc., 2014.

146. K. L. Mittal [Ed.]. *Silanes and Other Coupling Agents, Volume 5.* CRC Press, 2009.

147. P. V. Der Voort, E. F. Vansant. Silylation of the Silica Surface A Review. *J Liq Chromatogr Relat Technol* **19** (1996) 2723–2752.

148. A. Ulman. Formation and Structure of Self-Assembled Monolayers. *Chem Rev* **96** (1996) 1533–1554.

149. O. Seitz, P. G. Fernandes, R. Tian, N. Karnik, H.-C. Wen, H. Stiegler, R. A. Chapman, E. M. Vogel, Y. J. Chabal. Control and stability of self-assembled monolayers under biosensing conditions. *J Mater Chem* **21** (2011) 4384–4392.

150. R. Ulbrich, R. Golbik, A. Schellenberger. Protein adsorption and leakage in carrier–enzyme systems. *Biotechnol Bioeng* **37** (1991) 280–287.

151. G. T. Hermanson. *Bioconjugate Techniques*. Academic Press, 1996.

152. J. Escorihuela, M. J. Bañuls, J. G. Castelló, V. Toccafondo, J. García-Rupérez, R. Puchades, Á. Maquieira. Chemical silicon surface modification and bioreceptor attachment to develop competitive integrated photonic biosensors. *Anal Bioanal Chem* **404** (2012) 2831–2840.

153. J. H. Chua, R.-E. Chee, A. Agarwal, S. M. Wong, G.-J. Zhang. Label-Free Electrical Detection of Cardiac Biomarker with Complementary Metal-Oxide Semiconductor-Compatible Silicon Nanowire Sensor Arrays. *Anal Chem* **81** (2009) 6266–6271.

154. M. Matsunaga, T. Ueno, T. Nakanishi, T. Osaka. Enantioselective potential response of a human serum albumin-modified ITO electrode for tryptophan. *Electrochem Commun* **10** (2008) 1844–1846.

155. F. Patolsky, G. Zheng, C. M. Lieber. Fabrication of silicon nanowire devices for ultrasensitive, label-free, real-time detection of biological and chemical species. *Nat Protocols* **1** (2006) 1711–1724.

156. G. Festag, A. Steinbrück, A. Wolff, A. Csaki, R. Möller, W. Fritzsche. Optimization of Gold Nanoparticle-Based DNA Detection for Microarrays. *J Fluoresc* **15** (2005) 161–170.

157. R. GhoshMoulick, X. T. Vu, S. Gilles, D. Mayer, A. Offenhäusser, S. Ingebrandt. Impedimetric detection of covalently attached biomolecules on field-effect transistors. *Phys Stat Sol A* **206** (2009) 417–425.

158. N. J. Alves, T. Kiziltepe, B. Bilgicer. Oriented Surface Immobilization of Antibodies at the Conserved Nucleotide Binding Site for Enhanced Antigen Detection. *Langmuir* **28** (2012) 9640–9648.

159. A. Gang, N. Haustein, L. Baraban, G. Cuniberti. Multifunctional reversibly sealable microfluidic devices for patterned material deposition approaches. *RSC Adv* **5** (2015) 11806–11811.

160. A. W. Flounders, D. L. Brandon, A. H. Bates. Patterning of immobilized antibody layers via photolithography and oxygen plasma exposure. *Biosens Bioelectron* **12** (1997) 447–456.

161. D. M. Mattox. *Handbook of Physical Vapor Deposition (PVD) Processing*. William Andrew, 2010.

162. E. Delamarche, A. Bernard, H. Schmid, A. Bietsch, B. Michel, H. Biebuyck. Microfluidic Networks for Chemical Patterning of Substrates: Design and Application to Bioassays. *J Am Chem Soc* **120** (1998) 500–508.

163. A. Khademhosseini, J. Yeh, G. Eng, J. Karp, H. Kaji, J. Borenstein, O. C. Farokhzad, R. Langer. Cell docking inside microwells within reversibly sealed microfluidic channels for fabricating multiphenotype cell arrays. *Lab Chip* **5** (2005) 1380–1386.

164. E. Kim, Y. Xia, G. M. Whitesides. Polymer microstructures formed by moulding in capillaries --- (MIMIC). *Nature* **376** (1995) 581–584.

165. C. Dagdeviren *et al*. Conformal piezoelectric systems for clinical and experimental characterization of soft tissue biomechanics. *Nat Mater* **14** (2015) 728–736.

166. D.-H. Kim *et al*. Epidermal Electronics. *Science* **333** (2011) 838–843.

167. Y. Zhang, R. Chad Webb, H. Luo, Y. Xue, J. Kurniawan, N. H. Cho, S. Krishnan, Y. Li, Y. Huang, J. A. Rogers. Theoretical and Experimental Studies of Epidermal Heat Flux Sensors for Measurements of Core Body Temperature. *Adv Healthcare Mater* **5** (2016) 119–127.

168. H. Lee, T. K. Choi, Y. B. Lee, H. R. Cho, R. Ghaffari, L. Wang, H. J. Choi, T. D. Chung, N. Lu, T. Hyeon, S. H. Choi, D.-H. Kim. A graphene-based electrochemical device with thermoresponsive microneedles for diabetes monitoring and therapy. *Nat Nanotechnol* **11** (2016) 566–572.

169. S. Xu *et al*. Stretchable batteries with self-similar serpentine interconnects and integrated wireless recharging systems. *Nat Commun* **4** (2013) 1543.

170. M. Meyer, N. Van Binh, V. Calero, L. Baraban, G. Cuniberti, J. A. Rogers. Imperceptible sensorics for medical monitoring. *IEEE 15th International Conference on Nanotechnology (IEEE-NANO)* 2015. 1309–1312.

171. B. Weng, R. L. Shepherd, K. Crowley, A. J. Killard, G. G. Wallace. Printing conducting polymers. *Analyst* **135** (2010) 2779–2789.

172. J. C. McDonald, D. C. Duffy, J. R. Anderson, D. T. Chiu, H. Wu, O. J. A. Schueller, G. M. Whitesides. Fabrication of microfluidic systems in poly(dimethylsiloxane). *Electrophoresis* **21** (2000) 27–40.

173. D. Alemu, H.-Y. Wei, K.-C. Ho, C.-W. Chu. Highly conductive PEDOT:PSS electrode by simple film treatment with methanol for ITO-free polymer solar cells. *Energy Environ Sci* **5** (2012) 9662–9671.

174. Y. Xia, J. Ouyang. PEDOT:PSS films with significantly enhanced conductivities induced by preferential solvation with cosolvents and their application in polymer photovoltaic cells. *J Mater Chem* **21** (2011) 4927–4936.

175. K. T. Nguyen, J. L. West. Photopolymerizable hydrogels for tissue engineering applications. *Biomaterials* **23** (2002) 4307–4314.

176. K. Franke, I. Kurth, M. Bornhäuser, C. Werner, T. Pompe. Biomimetic microcavities based on poly(dimethylsiloxane) elastomers. *Soft Matter* **5** (2009) 3505–3510.

177. J. P. Rolland, R. M. Van Dam, D. A. Schorzman, S. R. Quake, J. M. DeSimone. Solvent-Resistant Photocurable 'Liquid Teflon' for Microfluidic Device Fabrication. *J Am Chem Soc* **126** (2004) 2322–2323.

178. A. Gang, G. Gabernet, L. D. Renner, L. Baraban, G. Cuniberti. A simple two-step silane-based (bio-) receptor molecule immobilization without additional binding site passivation. *RSC Adv* **5** (2015) 35631–35634.

179. T. Pompe, S. Zschoche, N. Herold, K. Salchert, M.-F. Gouzy, C. Sperling, C. Werner. Maleic Anhydride Copolymers - A Versatile Platform for Molecular Biosurface Engineering. *Biomacromolecules* **4** (2003) 1072–1079.

180. R. G. Chapman, E. Ostuni, L. Yan, G. M. Whitesides. Preparation of Mixed Self-Assembled Monolayers (SAMs) That Resist Adsorption of Proteins Using the Reaction of Amines with a SAM That Presents Interchain Carboxylic Anhydride Groups. *Langmuir* **16** (2000) 6927–6936.

181. J. Blümmel, N. Perschmann, D. Aydin, J. Drinjakovic, T. Surrey, M. Lopez-Garcia, H. Kessler, J. P. Spatz. Protein repellent properties of covalently attached PEG coatings on nanostructured SiO2-based interfaces. *Biomaterials* **28** (2007) 4739–4747.

182. K. Yallup, K. Iniewski. *Technologies for Smart Sensors and Sensor Fusion.* CRC Press, 2014.

183. S. Wang, T. Wang, P. Ge, P. Xue, S. Ye, H. Chen, Z. Li, J. Zhang, B. Yang. Controlling Flow Behavior of Water in Microfluidics with a Chemically Patterned Anisotropic Wetting Surface. *Langmuir* **31** (2015) 4032–4039.

184. A. I. Hochbaum, R. Fan, R. He, P. Yang. Controlled Growth of Si Nanowire Arrays for Device Integration. *Nano Lett* **5** (2005) 457–460.

185. H. T. Ng, J. Han, T. Yamada, P. Nguyen, Y. P. Chen, M. Meyyappan. Single Crystal Nanowire Vertical Surround-Gate Field-Effect Transistor. *Nano Lett* **4** (2004) 1247–1252.

186. R. Janissen, L. Oberbarnscheidt, F. Oesterhelt. Optimized straight forward procedure for covalent surface immobilization of different biomolecules for single molecule applications. *Colloids Surf B Biointerfaces* **71** (2009) 200–207.

187. http://www.abcr.de/shop/de/3-Aminopropyldimethylethoxysilane-97-19463.html/ (Accessed: 9th April 2016)

188. http://www.abcr.de/shop/de/3-Triethoxysilyl-propylsuccinic-anhydride-94-63298.html/ (Accessed: 9th April 2016)

189. http://www.abcr.de/shop/de/1H-1H-2H-2H-Perfluorooctyldimethylchlorosilane-97-7129.html/   (Accessed: 11th April 2016)

190. http://www.nanocs.net/PEG/Surface-reactive-PEG/methoxy-PEG-silane/Silane-PEG-350.htm   (Accessed: 11th April 2016)

191. S. S. Shah, M. C. Howland, L.-J. Chen, J. Silangcruz, S. V. Verkhoturov, E. A. Schweikert, A. N. Parikh, A. Revzin. Micropatterning of Proteins and Mammalian Cells on Indium Tin Oxide. *ACS Appl Mater Interfaces* **1** (2009) 2592–2601.

192. T. Pompe, L. Renner, M. Grimmer, N. Herold, C. Werner. Functional Films of Maleic Anhydride Copolymers under Physiological Conditions. *Macromol Biosci* **5** (2005) 890–895.

193. B. Dorvel, B. Reddy, I. Block, P. Mathias, S. E. Clare, B. Cunningham, D. E. Bergstrom, R. Bashir. Vapor-Phase Deposition of Monofunctional Alkoxysilanes for Sub-Nanometer-Level Biointerfacing on Silicon Oxide Surfaces. *Adv Funct Mater* **20** (2010) 87–95.

194. D. Janssen, R. De Palma, S. Verlaak, P. Heremans, W. Dehaen. Static solvent contact angle measurements, surface free energy and wettability determination of various self-assembled monolayers on silicon dioxide. *Thin Solid Films* **515** (2006) 1433–1438.

195. M. H. Lee, D. Boettiger, P. Ducheyne, R. J. Composto. Self-assembled monolayers of omega-functional silanes: A platform for understanding cellular adhesion at the molecular level. *Silanes and Other Coupling Agents* **4** (2007) 163–178.

196. M. Schena, D. Shalon, R. W. Davis, P. O. Brown. Quantitative Monitoring of Gene Expression Patterns with a Complementary DNA Microarray. *Science* **270** (1995) 467–470.

197. L. Jiang, S. Li, J. Wang, L. Yang, Q. Sun, Z. Li. Surface Wettability of Oxygen Plasma Treated Porous Silicon. *J Nanomater* **2014** (2014) e526149.

198. R. S. Wagner, W. C. Ellis. Vapor-liquid-solid mechanism of single crystal growth. *Appl Phys Lett* **4** (1964) 89–90.

199. S. Pregl, W. M. Weber, D. Nozaki, J. Kunstmann, L. Baraban, J. Opitz, T. Mikolajick, G. Cuniberti. Parallel arrays of Schottky barrier nanowire field effect transistors: Nanoscopic effects for macroscopic current output. *Nano Res* **6** (2013) 381–388.

200. C. Schmädicke. *Silicon nanowire based sensor for highly sensitive and selective detection of ammonia*. TU Dresden, 2015.

201. C. Schmädicke, S. Pregl, A. Gang, L. Baraban, G. Cuniberti. Silicon Nanowire based Sensor for Ammonia Detection. *in preparation.*

202. S. Pregl. *Fabrication and characterization of a silicon nanowire based Schottky-barrier field effect transistor platform for functional electronics and biosensor applications.* TU Dresden, 2014.

203. T. Y. Tan, N. Li, U. Gösele. Is there a thermodynamic size limit of nanowires grown by the vapor-liquid-solid process? *Appl Phys Lett* **83** (2003) 1199.

204. Z. Fan, J. C. Ho, Z. A. Jacobson, R. Yerushalmi, R. L. Alley, H. Razavi, A. Javey. Wafer-Scale Assembly of Highly Ordered Semiconductor Nanowire Arrays by Contact Printing. *Nano Lett* **8** (2008) 20–25.

205. A. Javey, Nam, R. S. Friedman, H. Yan, C. M. Lieber. Layer-by-Layer Assembly of Nanowires for Three-Dimensional, Multifunctional Electronics. *Nano Lett* **7** (2007) 773–777.

206. X. P. A. Gao, G. Zheng, C. M. Lieber. Subthreshold Regime has the Optimal Sensitivity for Nanowire FET Biosensors. *Nano Lett* **10** (2010) 547–552.

207. D. Niwa, T. Homma, T. Osaka. Fabrication of organic monolayer modified ion-sensitive field effect transistors with high chemical durability. *Jpn J Appl Phys* **43** (2003) L105.

208. D. Niwa, Y. Yamada, T. Homma, T. Osaka. Formation of Molecular Templates for Fabricating On-Chip Biosensing Devices. *J Phys Chem B* **108** (2004) 3240–3245.

209. V. Schmidt, J. V. Wittemann, S. Senz, U. Gösele. Silicon Nanowires: A Review on Aspects of their Growth and their Electrical Properties. *Adv Mater* **21** (2009) 2681–2702.

210. Y. Cui, L. J. Lauhon, M. S. Gudiksen, J. Wang, C. M. Lieber. Diameter-controlled synthesis of single-crystal silicon nanowires. *Appl Phys Lett* **78** (2001) 2214.

211. B. Wang, T. Stelzner, R. Dirawi, O. Assad, N. Shehada, S. Christiansen, H. Haick. Field-Effect Transistors Based on Silicon Nanowire Arrays: Effect of the Good and the Bad Silicon Nanowires. *ACS Appl Mater Interfaces* **4** (2012) 4251–4258.

212. E. Koren, G. Elias, A. Boag, E. R. Hemesath, L. J. Lauhon, Y. Rosenwaks. Direct Measurement of Individual Deep Traps in Single Silicon Nanowires. *Nano Lett* **11** (2011) 2499–2502.

213. D. V. Lang, H. G. Grimmeiss, E. Meijer, M. Jaros. Complex nature of gold-related deep levels in silicon. *Phys Rev B* **22** (1980) 3917–3934.

214. D. Ghosh, N. Chattopadhyay. Gold Nanoparticles: Acceptors for Efficient Energy Transfer from the Photoexcited Fluorophores. *Opt Photonics J* **03** (2013) 18–26.

215. B. Jean-Luc, D. Bruno. *Contamination monitoring and analysis in semiconductor manufacturing*. INTECH Open Access Publisher, 2010.

216. W. O. Filtvedt, A. Holt, P. A. Ramachandran, M. C. Melaaen. Chemical vapor deposition of silicon from silane: Review of growth mechanisms and modeling/scaleup of fluidized bed reactors. *Energ Mat Sol Cells* **107** (2012) 188–200.

217. M. Shimbo, K. Furukawa, K. Fukuda, K. Tanzawa. Silicon-to-silicon direct bonding method. *J Appl Phys* **60** (1986) 2987.

218. K. Seo, S. Sharma, A. A. Yasseri, D. R. Stewart, T. I. Kamins. Surface Charge Density of Unpassivated and Passivated Metal-Catalyzed Silicon Nanowires. *Electrochem Solid-State Lett* **9** (2006) G69.

219. Y. Wang, K.-K. Lew, J. Mattzela, J. Redwing, T. Mayer. Top-gated field effect devices using oxidized silicon nanowires. *IEEE: 63rd Device Research Conference Digest.* 2005. 159–160.

220. T. Kawashima, T. Saitoh, K. Komori, M. Fujii. Synthesis of Si nanowires with a thermally oxidized shell and effects of the shell on transistor characteristics. *Thin Solid Films* **517** (2009) 4520–4526.

221. L. D. Thanh, P. Balk. Elimination and Generation of Si - SiO$_2$ Interface Traps by Low Temperature Hydrogen Annealing. *J Electrochem Soc* **135** (1988) 1797–1801.

222. M. L. Reed, J. D. Plummer. Chemistry of Si-SiO$_2$ interface trap annealing. *J Appl Phys* **63** (1988) 5776–5793.

223. T. Voitsekhivska, E. Suthau, K.-J. Wolter. CMOS multiplexer for portable biosensing system with integrated microfluidic interface. *IEEE 64th Electronic Components and Technology Conference (ECTC).* 2014. 173–178.

224. S. P. Murarka. *Silicides for VLSI Applications*. Academic Press, 2012.

225. K. N. Tu. Interdiffusion in Thin Films. *Annu Rev Mater Sci* **15** (1985) 147–176.

226. N. S. Dellas, C. J. Schuh, S. E. Mohney. Silicide formation in contacts to Si nanowires. *Journal of Materials Science* **47** (2012) 6189–6205.

227. Y. E. Yaish, A. Katsman, G. M. Cohen, M. Beregovsky. Kinetics of nickel silicide growth in silicon nanowires: From linear to square root growth. *J Appl Phys* **109** (2011) 094303.

228. Y. Wu, J. Xiang, C. Yang, W. Lu, C. M. Lieber. Single-crystal metallic nanowires and metal/semiconductor nanowire heterostructures. *Nature* **430** (2004) 61–65.

229. W. M. Weber, L. Geelhaar, A. P. Graham, E. Unger, G. S. Duesberg, M. Liebau, W. Pamler, C. Chèze, H. Riechert, P. Lugli, F. Kreupl. Silicon-Nanowire Transistors with Intruded Nickel-Silicide Contacts. *Nano Lett* **6** (2006) 2660–2666.

230. W. M. Weber, L. Geelhaar, E. Unger, C. Chèze, F. Kreupl, H. Riechert, P. Lugli. Silicon to nickel-silicide axial nanowire heterostructures for high performance electronics. *Phys Stat Sol B* **244** (2007) 4170–4175.

231. A. Nagashima, T. Kimura, A. Nishimura, J. Yoshino. Comparative studies on the surface structures of $NiSi_2$ and epitaxially formed on Si(111). *Surface Science* **441** (1999) 158–166.

232. L. Bousse, P. Bergveld. The role of buried OH sites in the response mechanism of inorganic-gate pH-sensitive ISFETs. *Sens Actuators* **6** (1984) 65–78.

233. O. Knopfmacher, A. Tarasov, M. Wipf, W. Fu, M. Calame, C. Schönenberger. Silicon-Based Ion-Sensitive Field-Effect Transistor Shows Negligible Dependence on Salt Concentration at Constant pH. *ChemPhysChem* **13** (2012) 1157–1160.

234. O. Knopfmacher, A. Tarasov, W. Fu, M. Wipf, B. Niesen, M. Calame, C. Schönenberger. Nernst Limit in Dual-Gated Si-Nanowire FET Sensors. *Nano Lett* **10** (2010) 2268–2274.

235. J.-C. Chou, C.-Y. Weng. Sensitivity and hysteresis effect in Al_2O_3 gate pH-ISFET. *Mater Chem Phys* **71** (2001) 120–124.

236. N. Pinna, M. Knez. *Atomic Layer Deposition of Nanostructured Materials*. John Wiley & Sons, 2012.

237. D. K. Simon, P. M. Jordan, T. Mikolajick, I. Dirnstorfer. On the Control of the Fixed Charge Densities in Al_2O_3-Based Silicon Surface Passivation Schemes. *ACS Appl Mater Interfaces* **7** (2015) 28215–28222.

238. S. Park, S. Lee, C.-H. Kim, I. Lee, W.-J. Lee, S. Kim, B.-G. Lee, J.-H. Jang, M.-H. Yoon. Sub-0.5 V Highly Stable Aqueous Salt Gated Metal Oxide Electronics. *Sci Rep* **5** (2015)

239. K. V. Nemani, K. L. Moodie, J. B. Brennick, A. Su, B. Gimi. In vitro and in vivo evaluation of SU-8 biocompatibility. *Mater Sci Eng* **33** (2013) 4453–4459.

240. N. K. Rajan, D. A. Routenberg, M. A. Reed. Optimal signal-to-noise ratio for silicon nanowire biochemical sensors. *Appl Phys Lett* **98** (2011) 264107.

241. H. Abe, M. Esashi, T. Mats. ISFET's using inorganic gate thin films. *IEEE Trans Electron Devices* **26** (1979) 1939–1944.

242. S. B. Habib, E. G. Ii, R. F. Hicks. Atmospheric oxygen plasma activation of silicon (100) surfaces. *Vac Sci Technol* **28** (2010) 476–485.

243. P. Bataillard, P. Clechet, N. Jaffrezic-Renault, X. G. Kong, C. Martelet. The preparation of CHEMFET selective gates by thin silica layer grafting and their behaviour. *Sens Actuators* **12** (1987) 245–254.

244. J. Cesarano, I. A. Aksay, A. Bleier. Stability of Aqueous α-Al$_2$O$_3$ Suspensions with Poly (methacrylic acid) Polyelectrolyte. *J Am Ceram Soc* **71** (1988) 250–255.

245. M. Kosmulski. Attempt To Determine Pristine Points of Zero Charge of Nb$_2$O$_5$, Ta$_2$O$_5$, and HfO$_2$. *Langmuir* **13** (1997) 6315–6320.

246. D. R. Kim, C. H. Lee, X. Zheng. Probing Flow Velocity with Silicon Nanowire Sensors. *Nano Lett* **9** (2009) 1984–1988.

247. S. H. Jenkins, W. R. Heineman, H. B. Halsall. Extending the detection limit of solid-phase electrochemical enzyme immunoassay to the attomole level. *Anal Biochem* **168** (1988) 292–299.

248. Molecular weight and isoelectric point of various immunoglobulins. http://www.agrisera.com/en/info/molecular-weight-and-isoelectric-point-of-various-immunoglobulins.html (Accessed: 27th September 2016)

249. L. P. Kozlowski. *IPC - Isoelectric Point Calculator*. Biol Direct, 2016.

250. A. Gang, N. Haustein, L. Baraban, W. Weber, T. Mikolajick, J. Thiele, G. Cuniberti. Microfluidic alignment and trapping of 1D nanostructures – a simple fabrication route for single-nanowire field effect transistors. *RSC Adv* **5** (2015) 94702–94706.

251. A. K. Bentley, J. S. Trethewey, A. B. Ellis, W. C. Crone. Magnetic Manipulation of Copper–Tin Nanowires Capped with Nickel Ends. *Nano Lett* **4** (2004) 487–490.

252. X. Zhou, Y. Zhou, J. C. Ku, C. Zhang, C. A. Mirkin. Capillary Force-Driven, Large-Area Alignment of Multi-segmented Nanowires. *ACS Nano* **8** (2014) 1511–1516.

253. A. Tao, F. Kim, C. Hess, J. Goldberger, R. He, Y. Sun, Y. Xia, P. Yang. Langmuir–Blodgett Silver Nanowire Monolayers for Molecular Sensing Using Surface-Enhanced Raman Spectroscopy. *Nano Lett* **3** (2003) 1229–1233.

254. P. A. Smith, C. D. Nordquist, T. N. Jackson, T. S. Mayer, B. R. Martin, J. Mbindyo, T. E. Mallouk. Electric-field assisted assembly and alignment of metallic nanowires. *Appl Phys Lett* **77** (2000) 1399–1401.

255. Y. S. Zhao, A. Peng, H. Fu, Y. Ma, J. Yao. Nanowire Waveguides and Ultraviolet Lasers Based on Small Organic Molecules. *Adv Mater* **20** (2008) 1661–1665.

256. G. A. O'Brien, A. J. Quinn, D. A. Tanner, G. Redmond. A Single Polymer Nanowire Photodetector. *Adv Mater* **18** (2006) 2379–2383.

257. M. S. Gudiksen, L. J. Lauhon, J. Wang, D. C. Smith, C. M. Lieber. Growth of nanowire superlattice structures for nanoscale photonics and electronics. *Nature* **415** (2002) 617–620.

258. F. Qian, Y. Li, S. Gradečak, D. Wang, C. J. Barrelet, C. M. Lieber. Gallium Nitride-Based Nanowire Radial Heterostructures for Nanophotonics. *Nano Lett* **4** (2004) 1975–1979.

259. X. Duan, Y. Huang, R. Agarwal, C. M. Lieber. Single-nanowire electrically driven lasers. *Nature* **421** (2003) 241–245.

260. D. J. Sirbuly, M. Law, P. Pauzauskie, H. Yan, A. V. Maslov, K. Knutsen, C.-Z. Ning, R. J. Saykally, P. Yang. Optical routing and sensing with nanowire assemblies. *PNAS* **102** (2005) 7800–7805.

261. H. Kind, H. Yan, B. Messer, M. Law, P. Yang. Nanowire ultraviolet photodetectors and optical switches. *Adv Mater* **14** (2002) 158.

262. O. Assad, A. M. Leshansky, B. Wang, T. Stelzner, S. Christiansen, H. Haick. Spray-Coating Route for Highly Aligned and Large-Scale Arrays of Nanowires. *ACS Nano* **6** (2012) 4702–4712.

263. G. Yu, A. Cao, C. M. Lieber. Large-area blown bubble films of aligned nanowires and carbon nanotubes. *Nat Nanotechnol* **2** (2007) 372–377.

264. D. Whang, S. Jin, Y. Wu, C. M. Lieber. Large-Scale Hierarchical Organization of Nanowire Arrays for Integrated Nanosystems. *Nano Lett* **3** (2003) 1255–1259.

265. J.-H. Ahn, H.-S. Kim, K. J. Lee, S. Jeon, S. J. Kang, Y. Sun, R. G. Nuzzo, J. A. Rogers. Heterogeneous Three-Dimensional Electronics by Use of Printed Semiconductor Nanomaterials. *Science* **314** (2006) 1754–1757.

266. E. M. Freer, O. Grachev, D. P. Stumbo. High-yield self-limiting single-nanowire assembly with dielectrophoresis. *Nat Nanotechnol* **5** (2010) 525–530.

267. Y. Huang, X. Duan, Q. Wei, C. M. Lieber. Directed Assembly of One-Dimensional Nanostructures into Functional Networks. *Science* **291** (2001) 630–633.

268. J. Yao, H. Yan, C. M. Lieber. A nanoscale combing technique for the large-scale assembly of highly aligned nanowires. *Nat Nanotechnol* **8** (2013) 329–335.

269. P. J. Pauzauskie, A. Radenovic, E. Trepagnier, H. Shroff, P. Yang, J. Liphardt. Optical trapping and integration of semiconductor nanowire assemblies in water. *Nat Mater* **5** (2006) 97–101.

270. J. Lee, A. A. Wang, Y. Rheem, B. Yoo, A. Mulchandani, W. Chen, N. V. Myung. DNA Assisted Assembly of Multisegmented Nanowires. *Electroanalysis* **19** (2007) 2287–2293.

271. R. C. Givler, M. J. Crochet, R. B. Pipes. Numerical Prediction of Fiber Orientation in Dilute Suspensions. *J Compos Mater* **17** (1983) 330–343.

272. B. Lanfer, U. Freudenberg, R. Zimmermann, D. Stamov, V. Körber, C. Werner. Aligned fibrillar collagen matrices obtained by shear flow deposition. *Biomaterials* **29** (2008) 3888–3895.

273. N. Haustein. *Microfluidic alignment and trapping of silicon nanowires for the fabrication of single-nanowire field effect transistors*. TU Dresden, 2015.

274. C. D. Murray. The physiological principle of minimum work: I. The vascular system and the cost of blood volume. *PNAS* **12** (1926) 207.

275. R. W. Barber, D. R. Emerson. Optimal design of microfluidic networks using biologically inspired principles. *Microfluid Nanofluid* **4** (2008) 179–191.

276. R. K. Shah, A. L. London. *Laminar Flow Forced Convection in Ducts: A Source Book for Compact Heat Exchanger Analytical Data*. Academic Press, 2014.

277. S. Raychaudhuri, S. A. Dayeh, D. Wang, E. T. Yu. Precise Semiconductor Nanowire Placement Through Dielectrophoresis. *Nano Lett* **9** (2009) 2260–2266.

278. D. Widmann, H. Mader, H. Friedrich. *Technologie hochintegrierter Schaltungen*. Springer, 1996.

279. S. E. Jee, P. S. Lee, B.-J. Yoon, S.-H. Jeong, K.-H. Lee. Fabrication of Microstructures by Wet Etching of Anodic Aluminum Oxide Substrates. *Chem Mater* **17** (2005) 4049–4052.

280. L. Liao, Z. Zhang, B. Yan, Z. Zheng, Q. L. Bao, T. Wu, C. M. Li, Z. X. Shen, J. X. Zhang, H. Gong, J. C. Li, T. Yu. Multifunctional CuO nanowire devices: p-type field effect transistors and CO gas sensors. *Nanotechnology* **20** (2009) 085203.

281. X. Jiang, T. Herricks, Y. Xia. CuO Nanowires Can Be Synthesized by Heating Copper Substrates in Air. *Nano Lett* **2** (2002) 1333–1338.

282. I. Tzouvadaki, P. Jolly, X. Lu, S. Ingebrandt, G. de Micheli, P. Estrela, S. Carrara. Label-Free Ultrasensitive Memristive Aptasensor. *Nano Lett* **16** (2016) 4472–4476.

APPENDICES

A.1 PROTOCOLS

A.1.1 UV-Lithography

Preparation of master structures for microfluidic channels using SU-8 2010 *(SU-8 2050)* negative photoresist (MicroChem)

Substrate preparation	4'' SSP silicon wafer with native oxide (Siegert Wafer) treated with air plasma (Plasma Prep II, SPI supplies) for 2 min and heated to 95 °C for 10 min
Spin coating of photoresist	Two-step coating protocol: 500 rpm at 100 rpm s^{-1} for 10 s and 3000 rpm at 300 rpm s^{-1} for 45 s
Soft-bake	At 95 °C for 3 min *(7 min)*
UV-exposure	In MJB4 manual mask aligner (SÜSS MicroTec), 114 mJ cm^{-2} *(4 x 190 mJ cm^{-2})* at 365 nm
Post-exposure bake	At 95 °C for 3.5 min *(4 min)*
Development	In mr-Dev 600 for 3 min *(4 min)*
Rinsing	In isopropanol
Drying	Under a stream of N$_2$
Storage	In dust-free conditions in a container

Application of AZ5214e image reversal photoresist as positive resist and application of AZ6632 positive photoresist (both MicroChemicals GmbH)

Spin coating of photoresist	At 2000 rpm, 4000 rpm s^{-1} for 50 s
Bake	At 110 °C for 1.5 min

UV-exposure	In MJB4 manual mask aligner (SÜSS MicroTec), 57 mJ cm^{-2} at 365 nm
Development	In AZ 726 MIF developer for 1 min
Rinsing	In water
Drying	Under a stream of N$_2$

Application of AZ5214e image reversal photoresist as negative resist

Spin coating of photoresist	At 2000 rpm, 4000 rpm s^{-1} for 50 s
Prebake	At 120 °C for 1.5 min
UV-exposure	In MJB4 manual mask aligner (SÜSS MicroTec), 19 mJ cm^{-2} at 365 nm
Reversal bake	At 120 °C for 1.5 min
Flood exposure	In MJB4 manual mask aligner (SÜSS MicroTec), 570 mJ cm^{-2} at 365 nm
Development	In AZ 726 MIF developer for 1 min
Rinsing	In water
Drying	Under a stream of N$_2$

Patterned Au thin film deposition

Substrate preparation	AZ5214e lithography-based patterning of the surface
Au deposition	UNIVEX 300, Oerlikon Leybold Vacuum, 5nm Cr / desired thickness of Au

Lift-off	In acetone
Rinsing	In isopropanol
Drying	Under a stream of N_2

Patterned Ni thin film deposition on SiNWs

Substrate preparation	AZ5214e lithography-based patterning of the substrate
HF-dip	Dip in 1 % HF for 40 s (native SiO_2 shell around SiNWs) to 80 s (6nm thermal SiO_2 shell around SiNWs)
Rinsing	Extensively under a stream of water for 1.5 min
Drying	Under a stream of N_2
! Critical step !	Max. 5 min between last HF-contact of sample and introduction of sample into the vacuum chamber of sputtering device, due to fast reoxidation of Si
Ni deposition	At 10 keV beam energy in High Resolution Ion Beam Coater (Gatan, Inc.) until desired Ni thickness is reached
Lift-off	In acetone
Rinsing	In isopropanol
Drying	Under a stream of N_2

A.1.2 Soft lithography

Preparation of microfluidic channels *via* polydimethylsiloxane (PDMS)-based soft lithography

Pre-polymer mixing	Mixing of PDMS (Sylgard 184, Dow Corning) base and curing agent 10:1 by weight

Degassing	Under vacuum until no more air bubbles are visible
Casting	Pour liquid pre-polymer mixture onto master structure
Curing	At 45°C for at least 5 h
Mold disassembly	Peel cured PDMS cast from master structure
Storage	In dry and dust-free conditions with the indented structure facing away from the storage container

A.1.3 SiNW growth and thermal oxidation

SiNW growth

Substrate preparation	SSP silicon wafer with native oxide (Siegert Wafer) treated with air plasma (Plasma Prep II, SPI supplies) for 2 min
AuNP deposition	Dilute aqueous AuNP solution (20 nm Gold Nanospheres - BioPure, 1 mg/mL, BPEI-stabilized, nanoComposix Europe) 1:100 in water and cover wafer with solution for 30 min
Rinsing	Under flowing water
Substrate cleaning	Successive ultra-sonication in acetone, isopropanol and water, in each case for 10 min
Drying	Under a stream of N_2
Removing organic shell of Au-NP	250 W remote O_2 plasma (20sccm O_2, 50 Pa) in ATV SRO-706 Reflow Oven (ATV Technologies)
CVD growth of SiNWs	In customized Precision 5000 (Applied Materials) - pre-treatment: (1) 450 °C, 500 sccm H_2, 6.65 kPa, 230s, (2) H_2/Ar-plasma, 200 W, 450 °C, 950 sccm Ar, 50 sccm H_2, 0.4 kPa, 300 s - growth: 450 °C, 50 sccm SiH_4, 50 sccm H_2, 6.67 kPa (growth rate up to ~ 1 μm/min)

Thermal oxidation of SiNWs

Substrate preparation	Substrate with printed SiNWs is cleaned in acetone, isopropanol and water
Catalyst particle dissolution	In aqua regia (HNO_3:HCl, 1:3, vol./vol.) for 4 h
Rinsing	In water
Drying	Under a stream of N_2
Thermal oxidation	875°C, 100 kPa O_2, 6 min in rapid thermal processing furnace (RTP, AST Electronic GmbH)
Passivation of dangling bonds	450°, 100 kPa forming gas (H_2:N_2, 1:20, vol./vol.), 10 min (RTP, AST Electronic GmbH)

A.2 *IN SILICO* FLOW SIMULATION

Input parameter applied for *in silico* flow simulation studies of microfluidic NW alignment and trapping structures in COMSOL Multiphysics (courtesy of N. Haustein)

Property name	Value
Density of PDMS ρ_{PDMS}	970 kg m^{-3}
Young's modulus E_{PDMS}	750 kPa
Poisson's ratio v_{PDMS}	0.5
Density of isopropanol $\rho_{isopropanol}$	781 kg m^{-3}
Dynamic viscosity $\mu_{isopropanol}$	0.0025 Pa s
Pressure at inlet p_{in}	100 kPa
Pressure at outlet p_{out}	90 kPa

LIST OF PUBLICATIONS

PEER-REVIEWED PUBLICATIONS

A. Gang, N. Haustein, L. Baraban, G. Cuniberti. Multifunctional reversibly sealable microfluidic devices for patterned material deposition approaches. *RSC Adv.* **5** (2015) 11806–11811

A. Gang, G. Gabernet, L. D. Renner, L. Baraban, G. Cuniberti. A simple two-step silane-based (bio-) receptor molecule immobilization without additional binding site passivation. *RSC Adv.* **5** (2015) 35631–35634

A. Gang, N. Haustein, L. Baraban, W. Weber, T. Mikolajick, J. Thiele, G. Cuniberti. Microfluidic alignment and trapping of 1D nanostructures – a simple fabrication route for single-nanowire field effect transistors. *RSC Adv.* **5** (2015) 94702–94706

PUBLICATIONS IN PREPARATION

C. Schmädicke, S. Pregl, **A. Gang**, L. Baraban, G. Cuniberti. Silicon Nanowire based Sensor for Ammonia Detection.

SELECTED INTERNATIONAL CONFERENCES

A. Gang, G. Gabernet, N. Haustein, J. Thiele, L. Baraban, L. D. Renner, W. Weber, T. Mikolajick, G. Cuniberti. *Improved surface modification and microfluidic set-up for silicon nanowire-based biosensing*. Talk at ANNIC 2015, Paris

A. Gang, S. Pregl, F. Zörgiebel, L. Römhildt, C. Pahlke, W. Weber, L. Baraban, L. D. Renner, T. Mikolajick, G. Cuniberti. *Silicon nanowire based (bio) sensing*. Talk at TNT Conference 2014, Barcelona.

A. Gang, S. Pregl, F. Zörgiebel, L. Römhildt, C. Pahlke, W. Weber, L. Baraban, L. D. Renner, T. Mikolajick, G. Cuniberti. *Silicon nanowire based detection of blood proteins*. Talk at DPG Spring Meeting 2014, Dresden.

L. Römhildt, **A. Gang**, L. Baraban, J. Opitz, G. Cuniberti. *Supported lipid bilayer shells around silicon nanowires in aqueous solution*. Poster presentation at NanoBioEurope 2013, Toulouse.

ACKNOWLEDGEMENTS

VERSICHERUNG

Diese Arbeit wurde am Institut für Werkstoffwissenschaft der Technischen Universität Dresden unter der wissenschaftlichen Betreuung Prof. Dr. Gianaurelio Cunibertis durchgeführt.

Hiermit versichere ich, dass ich die vorliegende Arbeit ohne unzulässige Hilfe Dritter und ohne Benutzung anderer als der angegebenen Hilfsmittel angefertigt habe; die aus fremden Quellen direkt oder indirekt übernommenen Gedanken sind als solche kenntlich gemacht. Bei der Auswahl und Auswertung des Materials sowie bei der Herstellung des Manuskripts habe ich Unterstützung von folgenden Personen erhalten:

• Larysa Baraban (Korrekturlesen der gesamten Arbeit)

• Julian Thiele (Korrekturlesen der Einleitung und des Kapitel 1)

• Walter Weber (Korrekturlesen Unterkapitel 1.3 und Kapitel 4)

• Felix Zörgiebel (Matlab-Programmierung)

• Sebastian Pregl (Bereitstellung von Siliziumnanodrähten)

• Matthias Grube, Andreas Krause, Imad Ibrahim (Unterstützung bei Siliziumnanodraht Wachstum)

• Claudia Richter, Violetta Sessi, Thomas Henke (ALD Beschichtung von Proben)

• Natalie Haustein (Unterkapitel 5.2.2, 5.2.5 - 5.2.7)

Weitere Personen waren an der geistigen Herstellung der vorliegenden Arbeit nicht beteiligt. Insbesondere habe ich nicht die Hilfe eines kommerziellen Promotionsberaters in Anspruch genommen. Dritte haben von mir keine geldwerten Leistungen für Arbeiten erhalten, die in Zusammenhang mit dem Inhalt der vorgelegten Dissertation stehen. Die Arbeit wurde bisher weder im Inland noch im Ausland in gleicher oder ähnlicher Form einer anderen Prüfungsbehörde vorgelegt.

Darüber hinaus erkenne ich die Promotionsordnung der Fakultät Maschinenwesen der Technischen Universität Dresden vom 01.07.2001 an.

Andreas Gang

Dresden, 04.04.2017